BERNHARD EDEGGER

Charge ordering in α'-NaV_2O_5

DIPLOMARBEIT

zur Erlangung des akademischen Grades Diplomingenieur der
Studienrichtung Technische Physik

Technische Universität Graz

Betreuer:

Ao.Univ.-Prof. Hans Gerd Evertz
Institut für Theoretische Physik
Technische Universität Graz

Abstract

In this diploma thesis we consider the charge ordering process in α'-NaV_2O_5. This compound belongs to the low-dimensional transition metal oxides and forms a strongly correlated electron system, which can be described by an extended Hubbard model. We investigate the charge ordering in the presence of electron-lattice interactions for quarter-filled ladder systems by using Exact Diagonalization and DMRG(Density-Matrix-Renormalization-Group). We used model parameters obtained by first-principles band-structure calculations and saw that the system orders in a zig-zag pattern when the nearest neighbor Coulomb repulsion becomes large enough. The relevant Holstein coupling to the lattice considerably reduces the critical value of the nearest-neighbor Coulomb repulsion and the formation of a zig-zag charge-ordered state is then accompanied by a static lattice distortion. The coupling to the lattice changes the universality class of the corresponding quantum phase transition. We also investigated coupled ladder systems, which show a similar behavior as the single ladders systems when coupled to the static lattice distortions, but appear to order only at larger Coulomb repulsion without lattice distortions.

Zusammenfassung

Im Rahmen dieser Diplomarbeit wurde die Ladungsordnung in der Verbindung α'-Natriumvanadat untersucht. Dieses Material gehört zu den niedrigdimensionalen Übergangsmetalloxiden und bildet ein stark korreliertes Elektronensystem, welches über ein Hubbardmodel beschrieben werden kann. Die Ladungsordnung wurde unter Berücksichtigung der Elektron-Gitter Wechselwirkung in einem viertelgefüllten Leitersystem durch Verwendung von exakter Diagonalisierung und DMRG (Dichtematrix-Renormierungsgruppe) berechnet. Dazu wurden für das Natriumvanadat relevante Modelparameter verwendet, die aus "First-Principles" Bandstrukturrechnungen stammen. Die Ladung auf der Leiter ordnet in einem Zick-Zack-Muster, wenn die "Nächste-Nachbar" Coulomabstoßung groß genug ist. Die relevante Holstein-Kopplung mit dem Gitter verringert den kritischen Wert der "Nächste-Nachbar" Coulombabstoßung, an dem Zick-Zack-artig ladungsgeordnete Zustände entstehen, erheblich. Diese ladungsgeordneten Zustände sind zusätzlich von einer statischen Verzerrung des Gitters begleitet. Die Universalitätsklasse des zugehörigen quantenkritischen Punktes ändert sich durch die Ankopplung von statischen Gitterverzerrungen. Die Untersuchungen wurden sowohl für einfache als auch für gekoppelte Leitersystem durchgeführt. Ohne Gitterverzerrungen ordnet das gekoppelte Leitersysteme erst bei deutlich größerer Coulomb-Abstoßung als das einfache Leitersystem. Mit Gitterverzerrungen zeigen jedoch beide Systeme sehr ähnliche Ergebnisse.

Contents

Chapter 1

Introduction

This work treats the theoretical description and analysis of the charge order found in experiments on the compound α'-NaV_2O_5. Such studies are challenging because one has to solve a many body Schrödinger equation. An exact solution is only possible in few cases and hence one has to apply approximations, but the realistic description of electron correlations is still very difficult.

afsd

The introduction of an effective potential [1, 2] constitutes a very common approach in solid state physics. The potential describes the influence of all other electrons on a single one and has to be calculated self-consistently. So we have an one electron Schrödinger equation, where the correlations of the electrons are included in the effective potential. In this context the local density approximation (LDA) [3, 4] is often applied to solve the potential self-consistently. This method is in very common use and also very successful in many cases. Nevertheless LDA has problems to describe strongly correlated electrons like they exist in NaV_2O_5. In such systems the Coulomb energy and the kinetic energy of the electrons at the Fermi edge are of the same order of magnitude and strong nonlocal correlations occur which cannot be treated by a local density approximation.

Strongly correlated electrons can be found for example in systems with incompletely filled d- and f-electrons. Cuprates, Mangantes and also Vanadates are examples for such transition metal oxides. Due to their remarkable properties, these materials have become very important in solid state physics in recent years. Interesting examples are the high temperature superconductivity [5], Colossal Magneto-Resistance [6, 7] but also charge, spin and lattice order phenomena [8].

Many-particle-models have been developed to deal with strongly correlated electrons. In this diploma thesis, an extended Hubbard model is used to describe the salient properties of charge order in NaV_2O_5. Model parameters were taken from first-principles calculations by J.Spitaler and C. Ambrosch-Draxl (Reference [9]). The main object of my present work is the investigation of charge ordering in the low temperature phase in the presence of electron-phonon coupling. For that purpose we have to find the ground state of our Hamiltonian by using Exact Diagonalization of finite systems (for instance Lanzcos)[10], Quantum Monte Carlo (QMC)[11] or Density Matrix Renormalization Group (DMRG)[12].

This thesis contains the following chapters. In the second chapter the current knowledge about the compound NaV_2O_5 is presented and an effective Hubbard model is introduced. Model parameters, system sizes and boundary conditions used in this work are discussed. In the third chapter algorithms to determine ground state properties of the Hubbard model and its extensions are explained. While in these chapters are used only published results, the following chapters present new investigations on NaV_2O_5. The fourth chapter concentrates on the determination of the ground state pattern of static lattice distortions. The final two chapters treat the influence of electron-lattice interaction in single and coupled ladder systems.

Chapter 2

α'-NaV_2O_5 and the Hubbard model

In this chapter the compound α'-NaV_2O_5 is introduced. It belongs to the family of vanadates (LiV_2O_5, CaV_2O_5, MgV_2O_5,...) which are low-dimensional strongly correlated electron systems. The physical properties of V_2O_5-compounds have been very intensively investigated in the last few years. In particular the experimental and theoretical studies deal with the unconventional spin and charge excitation spectra. Nevertheless the behavior of the low temperature phase is not completely understood.

This chapter first gives an overview about structure and properties. In addition it presents present knowledge about NaV_2O_5 and open questions. Afterwards a theoretical model is introduced which should help to understand the experimental results. This model, an extended Hubbard model, is the basis of our calculations in the following chapters which primarily treat the charge ordering process as a function of different sets of model parameters. My present chapter often follows references [13] and [14].

2.1 Structure of NaV_2O_5

The first crystallographic structure analyses of NaV_2O_5 were done in the sixties and seventies by means of x-ray scattering [15]. Several different phases could be identified, which have VO_5-pyramids in common as the basic element of the structure.

α'-NaV_2O_5 is a special compound in the system $Na_xV_2O_5$. The α'-crystallographic structure is realized for doping of $0.70 \leq x \leq 1.00$. In the present thesis only

α'-NaV_2O_5 (always: $x = 1$) is treated and as a consequence the identification of the phase is dropped. Other phases of $Na_xV_2O_5$ are characterized by:

- α-phase: $0 < x \leq 0.02$
- β-phase: $0.22 \leq x \leq 0.4$
- α'-phase: $0.70 \leq x \leq 1.00$
- η-phase: $1.28 \leq x \leq 1.45$
- λ-phase: $1.68 \leq x \leq 1.82$

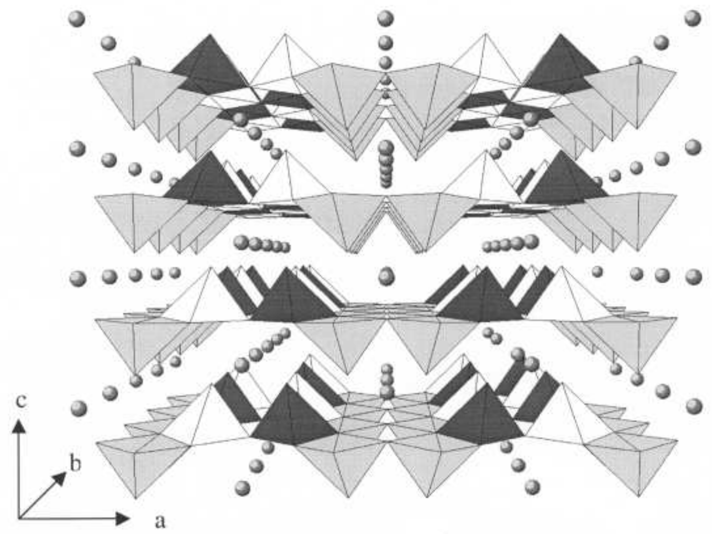

Figure 2.1: Crystallographic structure of NaV_2O_5. The pyramids are built by oxygen atoms around a central vanadium site. The sodium atoms are located between the V_2O_5 layers.

At room temperature α'-NaV_2O_5 crystallizes in space group *Pmmn* [17, 18, 19]. There is one crystallographically independent vanadium atom, that is in mixed-valence state 4.5+. The structure is schematically depicted in figure 2.1. It is mainly determined by the layers formed by the VO_5-pyramids. The sodium atoms, which are mainly acting as charge reservoirs, form chains, which are located between the layers. The coupling in c direction, i.e. between the layers, is very weak, and the properties of this compound are therefore mainly determined by the quasi two-dimensional V_2O_5-layers, shown in

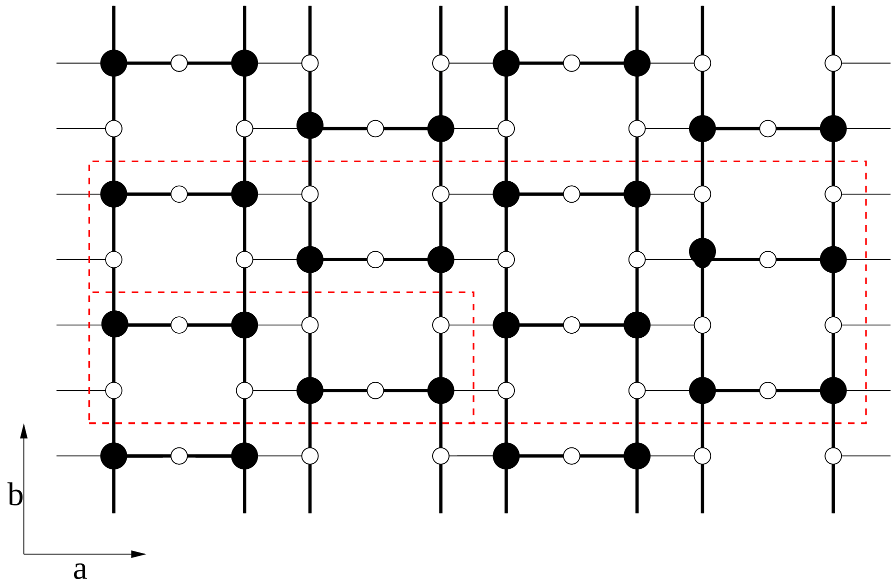

Figure 2.2: One V_2O_5-layer. Small white circles indicate oxygen atoms and big black circles vanadium atoms. Only the oxygen atoms of the ground plane of the pyramids are displayed. The thick lines indicate the V-ladders. The dashed rectangles show the unit cell of the high $(a \times b \times c)$ and the low $(2a \times 2b \times 4c)$ temperature phase. The lattice parameters of the unit cell are $a = 11.294$ Å, $b = 3.605$ Å and $c = 4.755$ Å [16].

figure 2.2. There the large black circles indicate the vanadium atoms and the small white ones the oxygen atoms of the ground plane of the pyramids. The oxygen on top of the pyramids is not important, because it does not couple different vanadium atoms.

2.2 Low temperature phase of NaV$_2$O$_5$

The present thesis concentrates on the investigation of the low temperature phase of NaV_2O_5, where an ordered pattern of the ion charges exists. The formation of charge ordering is a rather general type of phase transition which occurs in three- as well as lower-dimensional solids. It has been known for more than six decades [20] since its discovery in magnetite Fe_3O_4. NaV_2O_5 is another interesting example of a system which shows charge ordering [17]. Here the transition to a charge ordered phase, as observed in the nuclear magnetic resonance experiments [21], occurs at $T_C \approx 34K$, and is accompanied by the formation of a spin gap [22] at the same or [23] slightly lower temperature.

All these measurements are motivated by the experiment [24] carried out by Isobe and Ueda, who measured the temperature dependence of the magnetic susceptibility and obtained the following result (Figure 2.3):

NaV_2O_5 behaves like an $S = \frac{1}{2}$ 1-D anti-ferromagnetic Heisenberg linear chain above the critical temperature T_C. The coupling constant is determined as $J = 560K$ by fitting the experimental results to the theoretical formula. The phase transition at $T_C = 34K$ appears as a rapid decrease of the magnetic susceptibility.

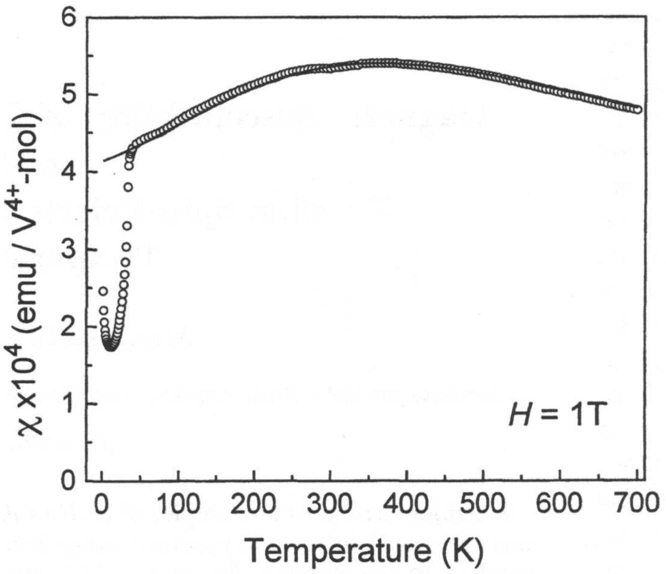

Figure 2.3: Magnetic susceptibility of NaV_2O_5 measured in a field of $H = 1T$. The solid line is a fit to the behavior of the $S = \frac{1}{2}$ 1-D Heisenberg model. The figure is taken from reference [24].

Isobe and Ueda suggested that this could be due to a Spin-Peierls transition, where the linear chain dimerizes below a critical temperature. This dimerization produces two different coupling constants and the ground state energy can therefore be lowered by coupled spin-singlets. Hence NaV_2O_5 would be the second inorganic compound besides $CuGeO_3$, where this phase transition occurs.

But there is evidence [23], that this phase transition is no real Spin-Peierls transition: The estimate for the spin gap Δ_S gives a value of $10\,meV$ [21]. As a result the BCS-ratio

$$\frac{2\Delta_S}{k_b T_C} \approx 6.5$$

is approximately twice as large as the BCS mean-field value of 3.52 for a Spin-Peierls transition. Furthermore the changes at T_C of the dielectric constant and the thermal conductivity differ significantly from the case of $CuGeO_3$, and the magnetic field dependence $\Delta T_C \propto H^2$ is only one fifth of what could be expected for a Spin Peierls transition.

Although in the experiment by Isobe and Ueda only one phase transition has been observed, newer investigations shows that there may be two close-by phase transitions [23]. The first one at T_{C_1} is accompanied by a logarithmic peak in the specific heat [25] while the second one at $T_{C_2} \approx T_{C_1} - 0.3K$ is of mean-field character evident from a jump in the specific heat. NMR measurements suggest that the first transition leads to charge ordering while the second one opens the spin gap [23]. Moreover, measurements of the critical exponents yield $\beta_\delta \approx 0.15...0.2$ for the critical exponent of the lattice distortion δ and $\beta_{\Delta_S} \approx 0.34$ for the critical exponent of the spin gap Δ_S [26, 27, 28, 29]. From these values the existence of two transitions can also be inferred indirectly. Close to the critical point, the spin gap Δ_S due to a lattice distortion δ is expected to obey $\Delta_S \propto \delta^{\frac{3}{4}}$ corresponding to $\beta_{\Delta_S} \propto \frac{3}{4}\beta_\delta$ [30]. This relation is not fulfilled in NaV_2O_5, indicating the existence of two separate transitions.[1]

The structure of the low temperature phase has been under discussion for a long time. On the one hand NMR at $T < T_C$ [21, 23] shows two different vanadium sites (V^{4+} and V^{5+}). On the other hand crystallographic measurements [16, 32] report a superlattice below T_C, which can be described by an F-centered orthorhombic $2a \times 2b \times 4c$ supercell (See figure 2.2.). The superstructure was found to have symmetry $Fmm2$ and an early analysis [16] using superspace symmetry found modulated and nonmodulated chains, which corresponds with three different vanadium sites (V^{4+}, $V^{4.5+}$and V^{5+}). As a result NMR and crystallographic measurements were not in agreement. This problem was solved by a model (proposed by *S. van Smaalen et. al.* [33]), that is characterized by layers with zig-zag charge order on all ladders and stacking disorder, such that the averaged structure has space group $Fmm2$.

2.3 Model

In theoretical condensed matter physics it is important to approximate reality with a treatable model. In the first steps band structure calculations [17, 9]

[1] In this paragraph reference [31] is quoted.

show that the density of states at the Fermi edge is mainly determined by the $3d_{xy}$-orbitals of the vanadium atoms. As a result, a low temperature model can be restricted to these orbitals. Furthermore the single V_2O_5-layers are only weakly coupled and the model is therefore chosen to be two dimensional [17]. It consists of ladders that are shifted in b-direction with respect to each other. The ladders are quarter-filled and are depicted in figure 2.4. In addition, the Coulomb repulsion between neighboring sites V_a, V_b, V_{xy} and the hopping terms t_a, t_b, t_{xy} are marked.

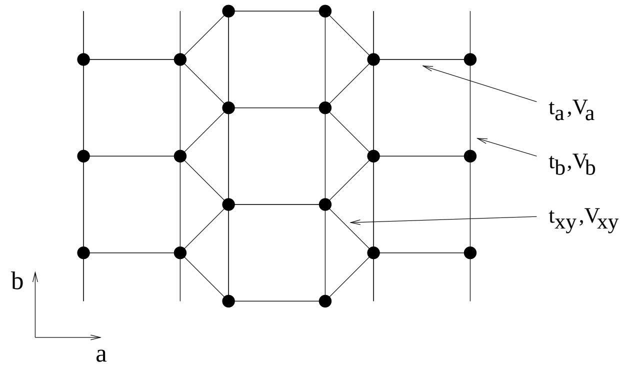

Figure 2.4: Lattice of the vanadium atoms in NaV_2O_5. The Coulomb repulsion to neighboring sites V_a, V_b, V_{xy} and the hopping terms t_a, t_b, t_{xy} are marked

2.3.1 Hubbard model

An appropriate basic model to describe the low energy physics of the electrons on the Vanadium $3d_{xy}$-orbitals appears to be the extended Hubbard model (EHM)

$$H_{\mathrm{EHM}} = -\sum_{\langle ij\rangle,\sigma} t_{ij}(c^\dagger_{i\sigma}c_{j\sigma} + \mathrm{H.c.}) + \sum_{\langle ij\rangle} V_{ij}n_i n_j \tag{2.1}$$

$$+ U\sum_i n_{i\uparrow}n_{i\downarrow} \tag{2.2}$$

where the density operators are given by $n_{i\sigma} = c^\dagger_{i\sigma}c_{i\sigma}$ and $n_i = n_{i\uparrow} + n_{i\downarrow}$. The sum over all next neighbor pairs is indicated by $\langle ij\rangle$. U is the intra-site Hubbard repulsion and V_{ij} is the inter-site Coulomb interaction . The t_{ij} describe the hopping from place i to j. It is important to derive appropriate values for these parameters. This step is explained in subsection 2.3.2.

The static properties of the ground state of doped ladders without coupling to lattice distortions has been extensively investigated using mean field approaches [34, 35, 36] and the density-matrix renormalization-group (DMRG) [37].

The DMRG studies [37] show for quarter-filling that at strong enough Hubbard nearest-neighbor-interaction the ladders exhibit a zig-zag charge order if the repulsion between the electrons on the nearest-neighbor sites exceeds some critical value V_C. The corresponding phase transition is of second-order as a function of V_C. For a very strong inter-site repulsion, phase separation becomes possible. However, reference [37] used parameters inappropriate for NaV_2O_5 (see below). Dynamical properties have been studied with exact numerical diagonalization [38, 13] without taking into account the coupling to the lattice. These studies have been quite successful in understanding NaV_2O_5 dynamical properties above the transition temperature but they could not describe the opening of a spin gap with parameters relevant for α'-NaV_2O_5.

In the present thesis we expand the model by terms which describe lattice-electron-repulsion. This has been already done by reference [39] for small lattices (up to 16 sites) by means of Lanczos methods. Here DMRG is used to diagonalize the Hamiltonian and as a consequence larger systems can be treated. In that way we hope to get a better understanding of the charge order and of the opening of the spin gap in α'-NaV_2O_5.

2.3.2 Model parameters

The Hamiltonian in equation 2.1 includes hopping terms t_{ij} and repulsions between nearest neighbors V_{ij}. In addition a parameter for the Coulomb repulsion U on the site exists.

In the beginning of this section we mentioned that band structure calculations show that the density of states at the Fermi edge is mainly determined by the vanadium atoms. These first principles calculations can also be used to estimate the parameters introduced above. In the present study we use the results of reference [9], which are compatible with these of reference [17].

In figure 2.4 the lattice of the vanadium atoms is depicted. One sees three different nearest neighbors and consequently three different types of hopping terms t_{ij} and Coulomb repulsions V_{ij}. The estimates of reference [9] are quoted in Tab.2.1, where a normalization to t_a is introduced. This henceforth is used in this work when model parameters are quoted. The notations become obvious if one looks at figure 2.4.

Description	Notation	in eV	normalized to t_a
Coulomb repulsion on site	U	≈ 2.80	8.00
Hopping term in a-direction	t_a	≈ 0.35	1.00
Hopping term in b-direction	t_b	≈ 0.17	0.50
Hopping term to next ladder	t_{xy}	≈ 0.12	0.33
Nearest neighbor repulsions	V_{ij}	?	1.00-8.00

Table 2.1: The parameters of the extended Hubbard model for NaV_2O_5 estimated by a first principles calculation [9].

Table.2.1 gives no clear information about the three values of nearest neighbor repulsions which are denoted in figure 2.4 (V_a, V_b, V_{xy}), because their estimates from band structure calculations are imprecise. Some estimates are $V_a = V_b = 0.8eV$ and $V_{xy} = 0.9eV$ [40]. On the other hand an analysis of the Coulomb repulsion

$$V_{ij} = \frac{1}{4\pi\epsilon_0\epsilon_r}\frac{e^2}{d_{ij}} \tag{2.3}$$

gives $V_a = 0.37eV$, $V_b = 0.10eV$ and $V_{xy} = 0.43eV$ [41]. Here the Coulomb repulsions V_{ij} only depend on the distances d_{ij} and the anisotropic dielectric constant ϵ_r. In conclusion the values V_{ij} appear to be smaller than the Coulomb repulsion U on the site. So we will investigate the Hubbard model by keeping the nearest neighbor Coulomb repulsion variable. To simplify the situation we restrict the study to equal repulsion V for each neighbor ($V_a = V_b = V_{xy} = V$).

2.3.3 System sizes and boundary conditions

In subsection 2.3.1, a Hamiltonian for an infinite 2D-model has been defined to describe properties of NaV_2O_5. As a consequence the number of sites in our lattice is infinite too. Such systems cannot be diagonalized by DMRG (Section 3.2) or Lanczos routines (Section 3.1). Due to this fact we restrict ourselves to finite systems with a small number of sites. In this subsection an overview is given of how the finite system sizes and the corresponding boundary conditions are chosen.

In all cases we try to choose the systems as large as possible. In addition we always calculate the properties for different system sizes and carry out a finite size scaling to estimate the values for the infinite system. Furthermore periodic boundary conditions are preferred over open boundary conditions, because they reduce boundary effects. Nevertheless open boundary conditions have been necessary for all DMRG calculations.

Lanczos calculations

Lanczos calculations for the Hubbard model are restricted to about 16 sites. As a consequence the two biggest systems we are able to investigate are

- a single ladder with 8 rungs (Figure 2.5a). Here periodic boundary conditions in b-directions and open boundary conditions in a-directions are chosen. In other words the coupling to the next ladder is neglected by choosing $V_{xy} = t_{xy} = 0$.
- two coupled ladders with 4 rungs per ladder and with periodic boundary conditions in both directions (Figure 2.5b).

DMRG calculations

DMRG calculations have the advantage that they can treat larger systems. Unfortunately the algorithm works worse for periodic boundary conditions and as a result we are restricted to open boundary conditions. The biggest systems we consider are

- a single ladder with 80 rungs and open boundary conditions in both directions (Figure 2.6a).
- two coupled ladders with 24 rungs per ladder and with periodic boundary conditions only in a-direction (Figure 2.6b).

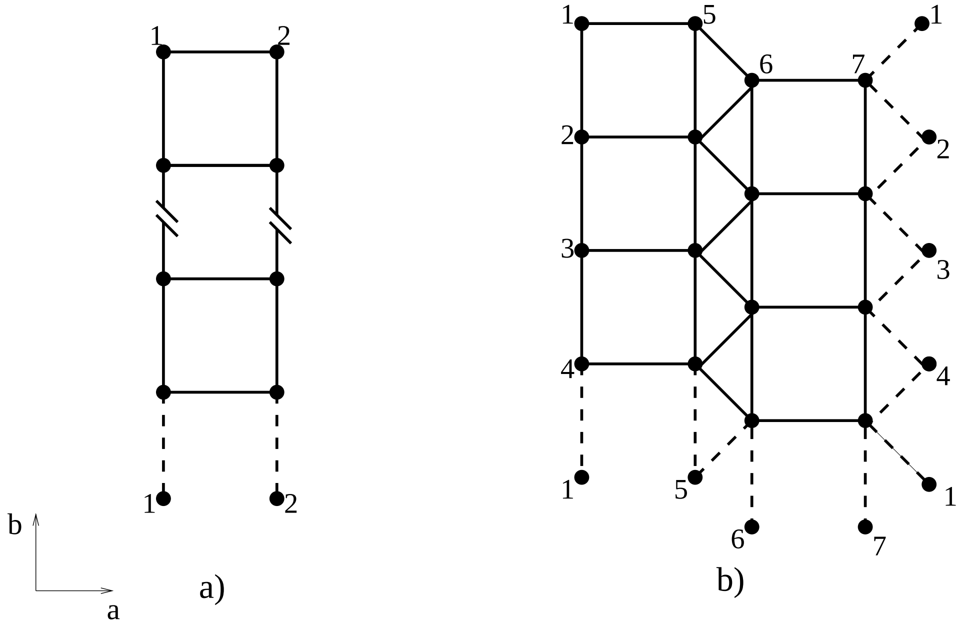

Figure 2.5: Lattices investigated with the Lanczos method. a) shows the single ladder system, b) shows the coupled ladder system. The dashed lines indicate the periodic jumps over the boundary. The lines in the middle of the ladder denote that only a part of the whole lattice is drawn.

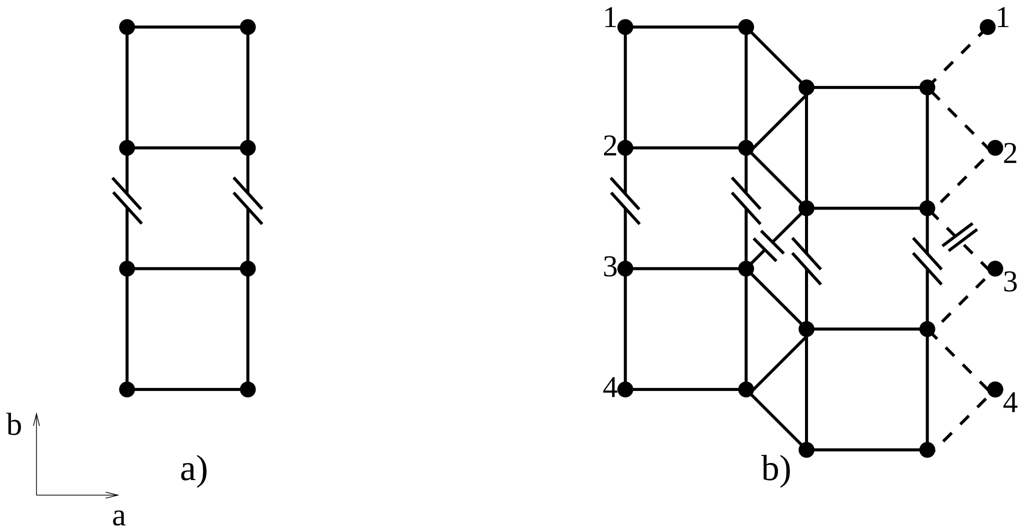

Figure 2.6: Lattices investigated with DRMG. a) shows the single ladder system, b) shows the coupled ladder system. The dashed lines indicate the periodic jumps over the boundary. The lines in the middle of the ladder denote that only a part of the whole lattice is drawn.

2.3.4 Electron-lattice interactions

At $T \ll T_C$ the ions in NaV_2O_5 are displaced from their equilibrium position in the high-temperature phase by distances of the order of 0.05 Å. These displacements which give evidence for a strong electron-lattice coupling have been observed in X-ray diffraction [16, 33, 32] and can be estimated from infrared [42] and Raman scattering experiments [43]. They stabilize the zig-zag ordered phase [34, 36], being probably the crucial element that determines the physics of the charge ordering in this compound. At the same time, the coupling to dynamical phonons induces strong charge fluctuations near T_C which alter the spin-spin exchange J [44].[2]

LDA calculations [9] show that the main mechanism of electron-phonon coupling can be assigned to Holstein-like interaction. In this section, we therefore consider the extended Hubbard Holstein model (EHHM)

$$H = H_{\mathrm{EHM}} + \underbrace{\sum_i \left(\frac{1}{2M}\hat{p}_i^2 + \frac{\kappa}{2}\hat{z}_i^2 \right)}_{\text{harmonic oscillator}} - \underbrace{C \sum_i n_i \hat{z}_i}_{\text{coupling}} \, , \tag{2.4}$$

with H_{EHM} defined in equation 2.1 and M being the mass of the local oscillators. The operators $\hat{z}_i$ and $\hat{p}_i$ are the coordinate and momentum of the oscillator on lattice site i. Further parameters are the Holstein constant C and the lattice force constant κ.

This thesis is restricted to static lattice distortion because interactions with dynamical (quantum) phonons are much more difficult to evaluate. Since the number of phonons is not conserved, the Hilbert space contains an infinite number of states, even for a finite number of lattice sites, and it has to be truncated in some way in order to apply Exact Diagonalization or DMRG methods. Reference [39] includes dynamical phonons, but there the authors have been forced to restrict the calculations to three phonons on the whole lattice, which certainly constitutes an enormous constraint.

To treat only static distortions we neglect the phonon oscillations by setting

$$\hat{p}_i^2 \equiv 0 \qquad \hat{z}_i \rightarrow z_i \tag{2.5}$$

Then the Hamiltonian can be written as follows:

$$H = H_{\mathrm{EHM}} + H_l + H_{e-l} \tag{2.6}$$

[2]This introduction into electron-lattice interactions follows reference [9].

The term H_l is the lattice deformation contribution and H_{e-l} is the electron-lattice interaction. These terms are given by

$$H_l = \kappa \sum_i \frac{z_i^2}{2} \tag{2.7}$$

$$H_{e-l} = -C \sum_i z_i n_i \tag{2.8}$$

The parameters C and κ can be extracted from first-principles band-structure calculations by comparing the total energy and the inter-ionic forces in distorted and undistorted lattices. Reference [9] provides us with a Holstein constant $C = 0.35$ (normalized), which describes the coupling of lattice distortions and electrons and a lattice force constant $\kappa = 0.125$ (also normalized), which includes the resulting force if an atom is displaced from its optimal lattice position.[3]

In the ansatz 2.4 only distortions in one "z"-direction are considered. So one variable z_i, which indicates the distortion, belongs to each site i. This restriction is in good agreement with experimental work on NaV_2O_5. In this context the authors of reference [16] observed zig-zag distortions of the V-ions in c-direction like it is illustrated in figure 2.7.

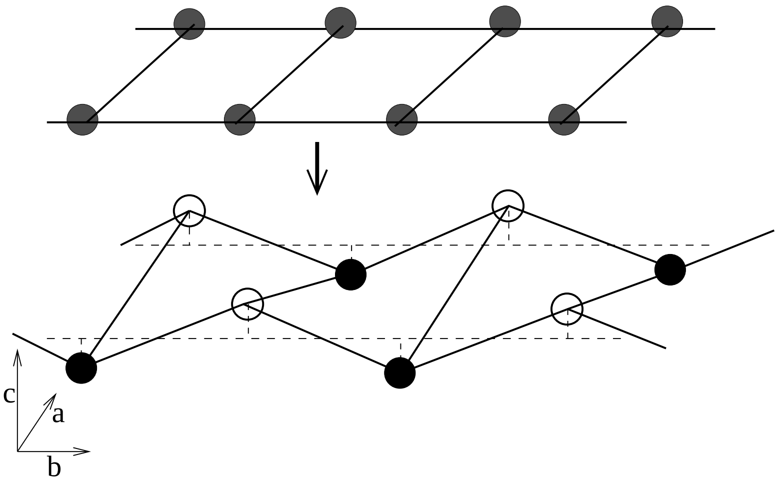

Figure 2.7: Illustrative picture of the zig-zag distortions of the V-ions in NaV_2O_5 like observed by reference [16] in the low temperature phase.

If we study ground state properties of this model, we have to find the optimal set of distortions z_i, which minimizes the ground state energy of the Hamil-

[3] These parameters are derived by considering the distortions of the V-O3 stretching of the $996 cm^{-1}$-phonon mode in reference [9]. They correspond to the distortions of the V2-atoms and of the O32-atoms like mentioned by reference [16].

tonian. In case there is a pure zig-zag pattern of distortions, the number of independent distortions z_i is reduced to one parameter z:

$$z_i = z e^{i\mathbf{Q}R_i} \quad \text{with} \quad \mathbf{Q} = (\pi, \pi) \tag{2.9}$$

The calculations in reference [39] were carried out in this way and produced the result plotted in figure 2.8. There the energies per site are shown for different nearest neighbor repulsions as a function of the zig-zag distortion z. The optimal distortion z_{opt} minimizes the total energy.

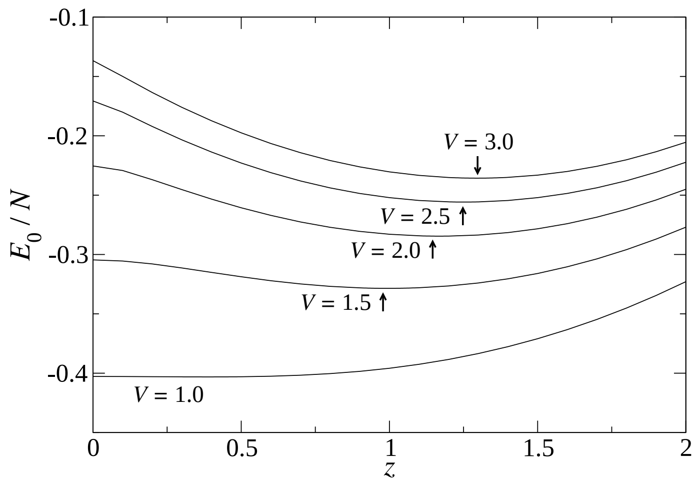

Figure 2.8: Ground state energy per site as a function of the distortion z calculated on an 8×2 system with periodic boundary conditions along the ladder and $C = 0.35$. From bottom to top: $V = 1.0, 1.5, 2.0, 2.5, 3.0$. The arrows indicate the position of the minimum. Figure and text are taken from reference [39].

But this approach, assuming zig-zag distortions was ad hoc. In the present thesis, we do not impose this assumption, but treat all z_i independently. Monte Carlo calculations using tempering methods can than be used to obtain the ground state pattern of distortions, which turns out to indeed be a purely zig-zag pattern. Such calculations are done in chapter 4.

2.3.5 Order parameters

We have mentioned several times that for an appropriate set of model parameters we obtain zig-zag charge ordering in the quarter-filled Hubbard model. In this subsection we define observables to determine the charge ordering of the ground state. Figure 2.9 illustrates the zig-zag charge order.

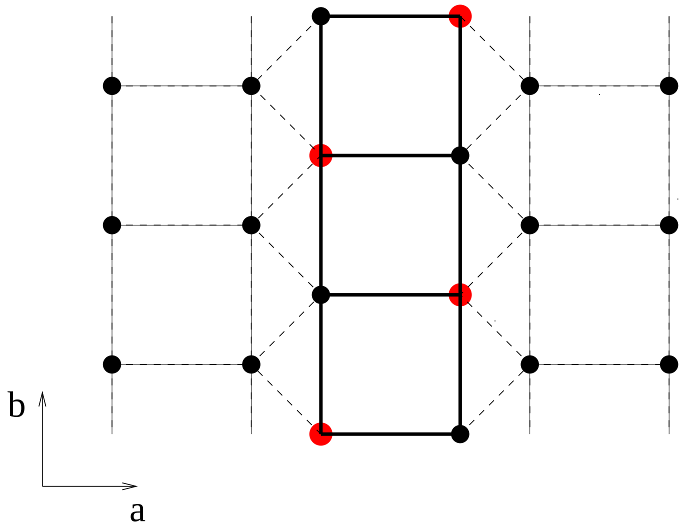

Figure 2.9: Schematic picture of a zig-zag charge ordered ladder. The large red circles mark the charged sites in the ladder.

To investigate the connections between lattice distortion and charge ordering we define a static charge structure factor

$$S_{CO}(\mathbf{q}) = \frac{1}{N} \sum_{ij} e^{i\mathbf{q}(\mathbf{R}_i - \mathbf{R}_j)} \left(\langle n_i n_j \rangle - \langle n \rangle^2 \right) \tag{2.10}$$

where $\hat{n}_i$ is the electron density operator at site i and N is the total number of sites in a single ladder. The sum over i and j includes all sites in a single ladder. Definition 2.10 gives an individual static charge structure factor for each individual ladder, if the system consists of more than one single ladder. Due to the symmetry of the system this static charge structure factor must be equal on each ladder. The zig-zag charge order parameter m_{CO} can be expressed in terms of the structure factor as

$$m_{CO}^2 = \frac{1}{N\langle n \rangle^2} S_{CO}(\mathbf{Q}), \quad \mathbf{Q} = (\pi, \pi). \tag{2.11}$$

The term $\langle n \rangle^2$ in the denominator ensures that the order parameter is equal to unity for full ordering , which in NaV_2O_5 corresponds to the charges of V ions within a rung to be equal to +5 and +4, respectively. This charge order parameter has to be determined individually for each single ladder.

In the same way a static distortion structure factor $S_{DO}(\mathbf{q})$ is defined for each ladder as

$$S_{DO}(\mathbf{q}) = \frac{1}{N^2} \sum_{ij} e^{i\mathbf{q}(\mathbf{R}_i - \mathbf{R}_j)} z_i z_j \tag{2.12}$$

where z_i and z_j are the distortions on site $\mathbf{R}_i$ and $\mathbf{R}_j$.

2.3.6 Order or Disorder

In the case of coupled ladders it has not been clear for a long time, whether charge order occurs on all or only on every second ladder. This questions seems to has been answered by reference [33], which explains the experimental data by a model with zig-zag charge order on all ladders and stacking disorder.

The distinction between these two situations turns out to be unexpectedly difficult for our theoretical considerations. The main reason is the equivalence of each ladder in a system of coupled ladders. As we will see, a state in which only every second ladder orders does not even show up in correlations of charge densities between different ladders. In order to interpret correlation data, we developed the following simplified picture. Unfortunately we will see in the end, that we are not able to make a decision by calculating charge density-density correlations.

First we assume that the ground state wave vector $|\Psi_a\rangle$ consists of a total charge ordered wave vector $|\Psi_O\rangle$ and a total charge disordered wave vector $|\Psi_D\rangle$:

$$|\Psi_a\rangle = a|\Psi_O\rangle + \sqrt{1-a^2}|\Psi_D\rangle \tag{2.13}$$

So the ordering of the ground state $|\Psi_a\rangle$ only depends on the factor a which can vary between 0 and 1. In addition these vectors are only defined for one single ladder. A totally ordered vector $|\Psi_O\rangle$ can be written as

$$\begin{aligned} |\Psi_O\rangle = \frac{1}{\sqrt{2}} (\, & |0\rangle_1 \otimes |1\rangle_2 \otimes |1\rangle_3 \otimes |0\rangle_4 \otimes |0\rangle_5 \otimes |1\rangle_6 \otimes \ldots + \\ & |1\rangle_1 \otimes |0\rangle_2 \otimes |0\rangle_3 \otimes |1\rangle_4 \otimes |1\rangle_5 \otimes |0\rangle_6 \otimes \ldots). \end{aligned} \tag{2.14}$$

(The asymmetric contribution would also be possible and would likely have a slightly larger energy.) Here the vector $|0\rangle_i$ indicates no electron on site i and the vector $|1\rangle_i$ denotes one electron on site i. The sites are numbered as demonstrated in figure 2.10. The two components of $|\Psi_O\rangle$ constitute the two possibilities to construct a total charge ordered state in a single ladder. The total charge disordered wave vector $|\Psi_D\rangle$ can be written as

$$|\Psi_D\rangle = \frac{1}{\sqrt{2^N}} \, (\, (|0\rangle_1 + |1\rangle_1) \otimes (|0\rangle_2 + |1\rangle_2) \otimes (|0\rangle_3 + |1\rangle_3) \otimes \ldots) \tag{2.15}$$

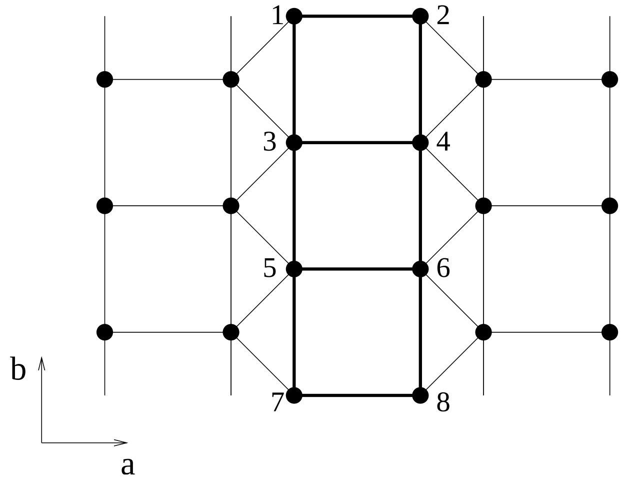

Figure 2.10: The picture shows how the sites in a ladder are numbered.

The scalar product

$$\langle \Psi_D | \Psi_O \rangle = \frac{1}{\sqrt{2^{N-1}}} \tag{2.16}$$

becomes very small for large N. Here N denotes the number of sites. So we consider the two components of $|\Psi_a\rangle$ as orthogonal which also justifies the normalization in equation 2.13.

Now we consider the ground state vector $|\Phi\rangle$ of two coupled ladders, which we assume to consist of wave vectors like $|\Psi_a\rangle$ for each single ladder. The ladders can order independently, which is described by an individual coefficient a for each ladder. As a result the ground state vector is composed of a vector $|\Psi_a\rangle$ and a vector $|\Psi_b\rangle$, which are defined in equation 2.13. A situation with $a \neq b$, i.e. the ladders ordering differently, cannot be detected by merely determining the order parameter m_{CO} for each ladder. This becomes obvious, if we consider the symmetry and write the ground state as

$$|\Phi\rangle = c(a,b) \, \left(|\Psi_a\rangle^{L1} \otimes |\Psi_b|\rangle^{L2} + |\Psi_b\rangle^{L1} \otimes |\Psi_a\rangle^{L2} \right). \tag{2.17}$$

We see that $|\Phi\rangle$ consists of two parts, which form a symmetric state. (The asymmetric contribution would again also be possible). Here $L1$ and $L2$ denote the ladder to which the vector belongs. $c(a,b)$ is a normalization factor given by

$$c(a,b) = \frac{1}{\sqrt{2}\sqrt{1 + \left(ab + \sqrt{1-a^2}\sqrt{1-b^2}\right)^2}} \tag{2.18}$$

If one calculates the order parameter m_{CO} of the state $|\Phi\rangle$, one obtains the same values for each ladder independent of coefficients a and b.

Now we calculate charge density-density pair correlations $\langle n_i n_j \rangle$ in the two ladder system. With the vector $|\Phi\rangle$ derived above there are only three different density-density pair correlations:

- correlations $\langle n_i n_j \rangle$ for sites i and j in the same ladder and the same zig-zag-modulated sub-lattice. They are identified by $\langle n_1 n_4 \rangle$.
- correlations $\langle n_i n_j \rangle$ for sites i and j in the same ladder but in different zig-zag-modulated sub-lattices. They are identified by $\langle n_1 n_2 \rangle$.
- correlations $\langle n_i n_j \rangle$ for sites i and j in different ladders. They are identified by $\langle n_{L1} n_{L2} \rangle$.

The correlations are illustrated in Fig.2.11 and their values are calculated in equations 2.19, 2.20 and 2.21.

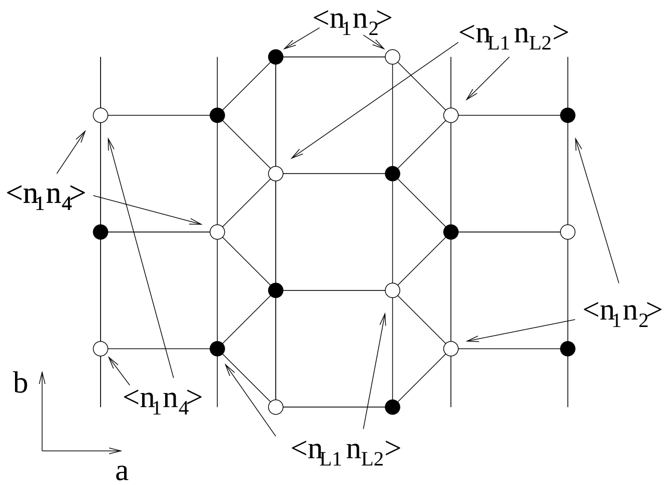

Figure 2.11: The figure shows some examples for the three different types of density-density pair correlations. White and black sites indicate the two different zig-zag modulated sub-lattices in each ladder. Note: Sites of the same color in different ladders do not belong to the same sub-lattice.

$$\langle n_1 n_4\rangle(a,b) = \frac{2+a^2+b^2+2\,\left(a\,b+\sqrt{1-a^2}\,\sqrt{1-b^2}\right)\,\left(2\,a\,b+\sqrt{1-a^2}\,\sqrt{1-b^2}\right)}{4\,\left(2+2\left(a\,b+\sqrt{1-a^2}\,\sqrt{1-b^2}\right)^2\right)} \tag{2.19}$$

$$\langle n_1 n_2\rangle(a,b) = \frac{2-a^2-b^2+2\sqrt{1-a^2}\,\sqrt{1-b}\,\left(a\,b+\sqrt{1-a^2}\,\sqrt{1-b^2}\right)}{4\,\left(2+2\left(a\,b+\sqrt{1-a^2}\,\sqrt{1-b^2}\right)^2\right)} \tag{2.20}$$

$$\begin{aligned}\langle n_{L1} n_{L2}\rangle(a,b) &= c(a,b)(((\langle\psi_a\psi_b| + \langle\psi_b\psi_a|)\hat{n}_{L1}\hat{n}_{L2}(|\psi_a\psi_b\rangle + |\psi_b\psi_a\rangle)) \\ &= \frac{1}{4} \end{aligned} \tag{2.21}$$

In equation 2.21 we used

$$\langle\psi_a\psi_b|\hat{n}_{L1}\hat{n}_{L2}|\psi_a\psi_b\rangle = \langle\psi_a|\hat{n}_{L1}|\psi_a\rangle\langle\psi_b|\hat{n}_{L2}|\psi_b\rangle \tag{2.22}$$

$$\langle\psi_a\psi_b|\hat{n}_{L1}\hat{n}_{L2}|\psi_b\psi_a\rangle = \langle\psi_a|\hat{n}_{L1}|\psi_b\rangle\langle\psi_b|\hat{n}_{L2}|\psi_a\rangle \tag{2.23}$$

with

$$\begin{aligned}\langle\psi_a|\hat{n}_{L1}|\psi_b\rangle &= \left(\langle\psi_O|a + \langle\psi_D|\sqrt{1-a^2}\right)\hat{n}_{L1}\left(|\psi_O\rangle b + |\psi_D\sqrt{1-b^2}\rangle\right) \\ &= \frac{1}{2}ab + \frac{1}{2}\sqrt{1-a^2}\sqrt{1-b^2} \\ &= \frac{1}{2}\langle\psi_a|\psi_b\rangle. \end{aligned} \tag{2.24}$$

With these and similar relations we can calculate $\langle n_{L1} n_{L2}\rangle(a,b) = \frac{1}{4}$. This equation shows that it is difficult to determine if each or only every second ladder shows charge ordering since the charge correlation between ladders is actually independent of a and b. Next we calculate the zig-zag order parameter, defined in equation 2.11, as a function of coefficients a and b.

$$\begin{aligned} m^2_{CO}(a,b) &= 2*(\langle n_1 n_4\rangle(a,b) - \langle n_1 n_2\rangle(a,b)) \\ &= \frac{a^2+b^2+2\,a^2\,b^2+2\,a\sqrt{1-a^2}\,b\sqrt{1-b^2}}{2+2\left(a\,b+\sqrt{1-a^2}\,\sqrt{1-b^2}\right)^2} \end{aligned} \tag{2.25}$$

Equation 2.25 implies that we can obtain the same charge order parameters for different sets of a and b. If a is equal to b each ladder orders in the same way. Then equation 2.25 reduces to

$$m_{CO} = a = b. \tag{2.26}$$

Next we calculate $\langle n_1 n_4 \rangle$ and $\langle n_1 n_2 \rangle$ with equations 2.19, 2.20 and 2.26 as a function of m_{CO}^2 in the case $a = b$. That yields the following equations:

$$\langle n_1 n_4 \rangle_{a=b}(m_{CO}^2) = \frac{1 + m_{CO}^2}{4} \tag{2.27}$$

$$\langle n_1 n_2 \rangle_{a=b}(m_{CO}^2) = \frac{1 - m_{CO}^2}{4} \tag{2.28}$$

Furthermore we want to know, if these relations between order parameter and the density-density correlations are similar for coefficients $a \neq b$. For that purpose we calculate the difference between $\langle n_1 n_4 \rangle(a, b)$ (Equation 2.19) and $\frac{1+m_{CO}^2(a,b)}{4}$ (with Equation 2.25) and the difference between $\langle n_1 n_2 \rangle(a, b)$ (Equation 2.20) and $\frac{1-m_{CO}^2(a,b)}{4}$ (with Equation 2.25):

$$\langle n_1 n_4 \rangle(a, b) - \frac{1 + m_{CO}^2(a, b)}{4} = 0 \tag{2.29}$$

$$\langle n_1 n_2 \rangle(a, b) - \frac{1 - m_{CO}^2(a, b)}{4} = 0 \tag{2.30}$$

The differences vanish for both cases and as a result the relations between order parameter and the density-density correlations are always the same (also when $a \neq b$):

$$\langle n_1 n_4 \rangle(m_{CO}^2) = \frac{1 + m_{CO}^2}{4} \tag{2.31}$$

$$\langle n_1 n_2 \rangle(m_{CO}^2) = \frac{1 - m_{CO}^2}{4} \tag{2.32}$$

As a result we have no change do distinguish between the two cases (each ladder orders or only every second ladder orders) in our model, if we only consider density-density pair correlations.

Chapter 3

Computational methods

3.1 Exact Diagonalization[1]

This work deals with strongly correlated electrons which are described by a Hubbard model. After locating a useful model we must find suitable numerical methods to calculate eigenvalues and observables. The Exact Diagonalization (ED) presents a very powerful method for evaluating finite systems [45, 46, 13]. Nevertheless the limitation to small systems is a severe drawback of ED. The Lanczos method, which we use in this work, is restricted to about 16 sites for the Hubbard model. As a consequence we also apply DMRG which is presented in section 3.2. In the sequel, an overview of Exact Diagonalization is given and the main ideas of the Lanczos algorithm are illustrated. For more details we refer to the literature mentioned above. In the last subsection we introduce the Davidson algorithm, that is used in our DMRG routine.

3.1.1 The Power Method

First of all we have to find a useful basis. Then we can transfer the Hamiltonian of the system into a Hamilton matrix and determine the eigenvalues and eigenstates by diagonalization. The power method is the simplest technique to calculate the eigenvector which corresponds to the "dominant eigenvalue". The denotation "dominant eigenvalue" will become clear when one looks at the following lines.

[1] This section often follows reference [14].

We consider an arbitrarily chosen normalized vector $|\phi_0\rangle$ and determine its behavior if one applies the Hamilton matrix $\mathcal{H}$ M-times.

$$\begin{aligned} \mathcal{H}^{M-1}|\phi_0\rangle &= \mathcal{H}^{M-1}\sum_{l=0}^{N} c_l|\psi_l\rangle \\ &= \sum_{l=0}^{N} c_l\ \varepsilon_l^{M-1}|\psi_l\rangle \\ &= c_0\ \varepsilon_0^{M-1}\left(|\psi_0\rangle + \sum_{l=1}^{N}\frac{c_l}{c_0}\left(\frac{\varepsilon_l}{\varepsilon_0}\right)^{M-1}|\psi_l\rangle\right), \end{aligned} \tag{3.1}$$

Here ε_l and $|\psi_l\rangle$ are the eigenvalues and eigenvectors of $\mathcal{H}$. Provided that M is a sufficiently high natural number, $c_0 \neq 0$, and

$$|\varepsilon_0| > |\varepsilon_l|, \quad \text{for all } l > 0, \tag{3.2}$$

equation 3.1 converges to the eigenstate $|\psi_0\rangle$. This state belongs to the "dominant eigenvalue" ε_0 specified above. Next we will introduce the Krylov-space and determine its most important characteristics. Afterwards the Lanczos algorithm, an improvement of the power method, is introduced.

3.1.2 The Krylov-space

If $\mathcal{H}$ is an $(N \times N)$-matrix and M is a natural number $M < N$, then the so called Krylov-space is given by

$$K_M = \text{linspan}\left\{|\phi_0\rangle, \mathcal{H}|\phi_0\rangle, \mathcal{H}^2|\phi_0\rangle, \ldots, \mathcal{H}^{M-1}|\phi_0\rangle\right\} \tag{3.3}$$

where $|\phi_0\rangle$ is a normalized random vector.

If M is sufficiently high, this space is an approximately invariant subspace of the Hilbert space. In this context an M-dimensional subspace $\mathcal{G}$ with $M < N$ is called invariant subspace, if

$$|\phi\rangle \in \mathcal{G} \Longrightarrow \mathcal{H}|\phi\rangle \in \mathcal{G} \tag{3.4}$$

for every element $|\phi\rangle$ of $\mathcal{G}$. The advantage of an invariant subspace is the possibility to calculate eigenvalues of the large $(N \times N)$-matrix $\mathcal{H}$ by diagonalizing an $(M \times M)$-matrix. If an arbitrary basis $|\gamma_1\rangle, \ldots, |\gamma_M\rangle$ is used, $\mathcal{G}$ can be written as an $(N \times M)$-matrix, where the columns $|\gamma_i\rangle$ of the matrix are the basis vectors of the subspace. If $\mathcal{G}$ is an invariant subspace, then the matrix product $\mathcal{HG}$ is again an $(N \times M)$-matrix, where the columns are linear combinations of vectors $|\gamma_i\rangle$. Now we can define an $(M \times M)$-matrix $\mathcal{H}_M$ by

$$\mathcal{HG} = \mathcal{GH}_M. \tag{3.5}$$

The next lines show the purpose of this equation. If we solve the eigenvalue problem

$$\mathcal{H}_M|\psi\rangle = \varepsilon|\psi\rangle \tag{3.6}$$

of $\mathcal{H}_M$, then we also determine the eigenvalues of $\mathcal{H}$. This becomes obvious if (3.6) is used in (3.5)

$$\mathcal{H}[\mathcal{G}|\psi\rangle] = \varepsilon[\mathcal{G}|\psi\rangle]. \tag{3.7}$$

To proof the claim that the Krylov-space is an approximately invariant subspace for sufficiently large M we apply the Hamiltonian matrix to the basis vectors given in equation 3.3. Then the following expression is achieved:

$$\left\{\mathcal{H}|\phi_0\rangle, \mathcal{H}^2|\phi_0\rangle, \ldots, \mathcal{H}^M|\phi_0\rangle\right\} \tag{3.8}$$

All elements of equation 3.8 except the last vector belong to K_M. But if we remember the power method and consider equation 3.1 we can also see the element $\mathcal{H}^M|\phi_0\rangle$ as an element of K_M. This method tells us that $\mathcal{H}^{M-1}|\phi_0\rangle$ is approximately proportional to the eigenstate $|\psi_0\rangle$. On the other hand we can argue for the term $\mathcal{H}^M|\phi_0\rangle$ in the same way. As a consequence $\mathcal{H}^M|\phi_0\rangle$ is approximately proportional to $|\psi_0\rangle$ and $|\psi_0\rangle$ is approximately proportional to $\mathcal{H}^{M-1}|\phi_0\rangle$. Then we see that also $\mathcal{H}^M|\phi_0\rangle$ is approximately proportional to $\mathcal{H}^{M-1}|\phi_0\rangle$ and belongs to the Krylov-space K_M in equation 3.3. So K_M is an approximately invariant subspace.

3.1.3 The Lanczos Algorithm

The Lanczos procedure starts with a normalized vector $|\phi_0\rangle$. This vector can be chosen at random as long as it has finite overlap with the ground state. Now we construct an orthogonal set of vectors by the following rule:

$$|\tilde{\phi}_1\rangle = \mathcal{H}|\phi_0\rangle - \varepsilon_0|\phi_0\rangle \tag{3.9}$$

$$|\tilde{\phi}_{n+1}\rangle = \mathcal{H}|\phi_n\rangle - \varepsilon_n|\phi_n\rangle - k_n|\phi_{n-1}\rangle \tag{3.10}$$

$$\varepsilon_n = \langle\phi_n|\mathcal{H}|\phi_n\rangle \tag{3.11}$$

$$k_n = \langle\phi_{n-1}|\mathcal{H}|\phi_n\rangle \tag{3.12}$$

$$|\phi_{n+1}\rangle = \frac{|\tilde{\phi}_{n+1}\rangle}{\parallel |\tilde{\phi}_{n+1}\rangle \parallel} \tag{3.13}$$

The orthogonality can be proved by induction. It is readily verified that $|\tilde{\phi}_1\rangle$ and $|\phi_0\rangle$ are orthogonal:

$$\begin{aligned}\langle\phi_0|\tilde{\phi}_1\rangle &= \langle\phi_0|\mathcal{H}|\phi_0\rangle - \varepsilon_0\langle\phi_0|\phi_0\rangle \\ &= \varepsilon_0 - \varepsilon_0 = 0\end{aligned} \tag{3.14}$$

Next we consider

$$|\tilde{\phi}_2\rangle = \mathcal{H}|\phi_1\rangle - \varepsilon_1|\phi_1\rangle - k_1|\phi_0\rangle. \tag{3.15}$$

We see the orthogonality to $|\phi_0\rangle$

$$\begin{aligned}\langle\phi_0|\tilde{\phi}_2\rangle &= \langle\phi_0|\mathcal{H}|\phi_1\rangle - \varepsilon_1\langle\phi_0|\phi_1\rangle - k_1\langle\phi_0|\phi_0\rangle \\ &= k_1^* - 0 - k_1 = 0\end{aligned} \tag{3.16}$$

and to $|\phi_1\rangle$

$$\begin{aligned}\langle\phi_1|\tilde{\phi}_2\rangle &= \langle\phi_1|\mathcal{H}|\phi_1\rangle - \varepsilon_1\langle\phi_1|\phi_1\rangle - k_1\langle\phi_1|\phi_0\rangle \\ &= \varepsilon_1 - \varepsilon_1 - 0 = 0\end{aligned} \tag{3.17}$$

where we used that k_1 is real. This is easily shown by

$$k_1^* = \langle\phi_1|\mathcal{H}|\phi_0\rangle = \langle\phi_1|\tilde{\phi}_1\rangle + \varepsilon_0\underbrace{\langle\phi_0|\phi_0\rangle}_{=0} = \|\ |\phi_n\rangle\ \| \in \mathbb{R}. \tag{3.18}$$

We can complete the proof, if we deduce the orthogonality for a set of n+1 vectors from orthogonality up to the n-th step. So we conclude with the following lines by taking into account the iteration rules mentioned above (3.9)-(3.13):

$$\begin{aligned}\langle\phi_n|\tilde{\phi}_{n+1}\rangle &= \underbrace{\langle\phi_n|\mathcal{H}|\phi_n\rangle}_{=\varepsilon_n} - \varepsilon_n\underbrace{\langle\phi_n|\phi_n\rangle}_{=1} - k_n\underbrace{\langle\phi_n|\phi_{n-1}\rangle}_{=0} = 0 \\ \langle\phi_{n-1}|\tilde{\phi}_{n+1}\rangle &= \underbrace{\langle\phi_{n-1}|\mathcal{H}|\phi_n\rangle}_{=k_n} - \varepsilon_n\underbrace{\langle\phi_{n-1}|\phi_n\rangle}_{=0} - k_n\underbrace{\langle\phi_{n-1}|\phi_{n-1}\rangle}_{=1} = 0 \\ \langle\phi_i|\tilde{\phi}_{n+1}\rangle &= \langle\phi_i|\mathcal{H}|\phi_n\rangle - \varepsilon_n\underbrace{\langle\phi_i|\phi_n\rangle}_{=0} - k_n\underbrace{\langle\phi_i|\phi_{n-1}\rangle}_{=0} \\ &= \left(\langle\phi_n|\mathcal{H}|\phi_i\rangle\right)^* \\ &= \Big(\langle\phi_n|\tilde{\phi}_{i+1}\rangle + \varepsilon_i\langle\phi_n|\phi_i\rangle + k_i\langle\phi_n|\phi_{i-1}\rangle\Big)^* \\ &= 0\end{aligned}$$

Note: $i < n-1$.

Therefore the Hamilton matrix represented in the Krylov basis is tridiagonal and has the following form:

$$\mathcal{H}_M = \begin{pmatrix} \varepsilon_0 & k_1 & 0 & \cdot & \cdot & \cdot \\ k_1 & \varepsilon_1 & k_2 & 0 & \cdot & \cdot \\ 0 & k_2 & \varepsilon_2 & k_3 & 0 & \cdot \\ \cdot & 0 & k_3 & \varepsilon_3 & k_4 & \ddots \\ \cdot & \cdot & 0 & k_4 & \varepsilon_4 & \ddots \\ \cdot & \cdot & \cdot & \ddots & \ddots & \ddots \end{pmatrix} \tag{3.19}$$

The eigenvalues of this matrix converge to the eigenvalues of the original Hamiltonian matrix when M becomes sufficiently large. In addition the ground state of $\mathcal{H}$ can be calculated by

$$|\Psi\rangle = \mathcal{G}|\psi\rangle, \tag{3.20}$$

where $|\psi\rangle$ is the eigenvector with lowest energy of the matrix $\mathcal{H}_M$. With this ground state we can determine the expectation value of a observable O in the straightforward way $\langle\Psi|O|\Psi\rangle$.

3.1.4 Davidson algorithm[2]

Last but not least we introduce the Davidson algorithm, which we used for our DMRG calculations. The basic idea of this alternative method to treat large matrix problems can be viewed as follows:

An intermediate set of vectors is established in terms of which the actual eigenvectors of $\mathcal{H}$ can be expanded. If this intermediate set of vectors $\{\mathbf{b}_p; p = 1, ..., P\}$ is cleverly chosen, then the approximation $\mathbf{x}_k$ to a true eigenvector $\mathbf{c}_k$, written in the form

$$\mathbf{x}_k = \sum_{p=1}^{P} \mathbf{b}_k \, a_{pk} \tag{3.21}$$

will converge to $\mathbf{c}_k$ even when P is much less than N and when $\{\mathbf{b}\}$ is a very incomplete set of basis vectors. If these basis vectors are organized as the columns of a matrix $\mathbf{B}$, and the expansion coefficients are placed in a column

[2]This subsection follows reference [47].

vector $\mathbf{a}_k$, then the variational approximation to the solution of the matrix eigenvalue problem

$$\mathcal{H}\,\mathbf{c}_k = \lambda_k\,\mathbf{c}_k \tag{3.22}$$

in the subspace becomes

$$\mathbf{B}^T\,\mathbf{H}\,\mathbf{B}\,\mathbf{a}_k = \mu_k^P\,\mathbf{B}^T\,\mathbf{B}\,\mathbf{a}_k, \quad k = 1, ..., P \tag{3.23}$$

in which the superscript T denotes matrix transpose. If the eigenvalues μ_k^P of this reduced problem are numbered in increasing order then, by the Hylleraas-Undheim-MacDonald variational principle [48] (which states that as the size of the basis increases, each eigenvalue tends to the true eigenvalue), the eigenvalues of the original problem 3.22 satisfy

$$\lambda_k \le \mu_k^P, \quad k = 1, ..., P\,. \tag{3.24}$$

Further, if $\{\mathbf{b}\}$ is simply augmented by an additional vector, then

$$\mu_k^P \le \mu_k^{P-1}, \quad k = 1, ..., P-1\,. \tag{3.25}$$

Hence, a general strategy is possible in which the eigenvalues $\{\mu_k^P, k = 1, ..., K; P = K, K+1, ...\}$ form monotonic nonincreasing sequences that converge to the desired exact eigenvalues $\{\lambda_k, k = 1, ..., K\}$.

If $\mathbf{x}_k$ is an approximation to $\mathbf{c}_k$, then the correction $\delta_k = \mathbf{c}_k - \mathbf{x}_k$ is given by solving

$$\begin{aligned} \mathbf{r}_k &= (\mathcal{H} - \lambda_k\mathbf{1})\mathbf{x}_k\,, \\ (\mathcal{H} - \lambda_k\mathbf{1})\delta_k &= -\mathbf{r}_k\,. \end{aligned} \tag{3.26}$$

The correction δ_k may be approximated by replacing λ_k by the Rayleigh quotient

$$\rho_k = \frac{\mathbf{x}_k^T\,\mathcal{H}\,\mathbf{x}_k}{\mathbf{x}_k^T\,\mathbf{x}_k} \tag{3.27}$$

and approximating the inverse of $(\mathcal{H} - \rho_k\mathbf{1})$ by $(\mathbf{D} - \rho_k\mathbf{1})^{-1}$, where $\mathbf{D}$ is the diagonal of $\mathcal{H}$. Thus,

$$\delta_k \approx -(\mathbf{D} - \rho_k\mathbf{1})^{-1}\mathbf{r}_k\,. \tag{3.28}$$

Simply adding δ_k to $\mathbf{x}_k$ to get a new estimate of $\mathbf{c}_k$ is found not to work well. If, however, $\mathbf{x}_k$ is the result of a variational calculation in a subspace

B, as described above, then δ_k is a good choice for the next addition to $\{\mathbf{b}\}$. This procedure is iterated until a suitable convergence criterion is met. In the original paper by Davidson [49], only one vector was added to **B** at each iteration. The modification suggest by Liu [50] was to add a correction vector for each desired root on each iteration. In practice, due to limitations in computer memory, a compromise is made, and corrections to as many vectors as possible are added each time.

3.2 Density Matrix Renormalization Group (DMRG)

The density matrix renormalization group (DMRG) is an alternative method to determine the lowest eigenvalues of a many particle Hamiltonian and has become a standard method to determine ground state properties of large 1-dimensional spin and fermion systems in recent years. Furthermore DMRG can still be used for larger systems, which show a nearly 1-dimensional structure. In particular, it is applicable to the ladder-like geometries studied in the present thesis, and, with more effort, also to the systems of two coupled ladders studied in chapter 6.

DMRG has been invented by Steven R. White in 1992 [51]. Since then a lot of great improvements and extensions on DMRG have been developed, but in the following explanations we only concentrate on the main ideas. For further information we refer to reference [12].

The outline of this chapter[3] is as follows: First it is briefly discussed why one needs an alternative to Exact Diagonalization, then the numerical renormalization group (NRG) procedure [52] is introduced. Afterwards we discuss the Density Matrix Projection and focus on the algorithms for finite, infinite and 2-dimensional systems.

3.2.1 Motivation

In this diploma thesis we deal with strongly correlated electron systems, which must be described by many-particle models. For our purposes we choose the Hubbard model, where one finds four different states per site ($|\uparrow\rangle$, $|\downarrow\rangle$, $|\uparrow\downarrow\rangle$, $|0\rangle$). If we treat a Hubbard system, which consists of n sites a basis of the Hilbert space is given by

$$|i_1\rangle \otimes |i_2\rangle \otimes ... \otimes |i_n\rangle. \tag{3.29}$$

Due to the fact that we have four states per sites we obtain 4^n basis states. As a consequence the number of basis states increases very rapidly with the system size n and Exact Diagonalization fails for large systems, because we run out of memory and/or CPU time. As a result we can only deal with small systems. In the Hubbard model we are restricted to about 16 sites, for example. Hence we need an alternative procedure.

[3]The chapter often follows reference [12].

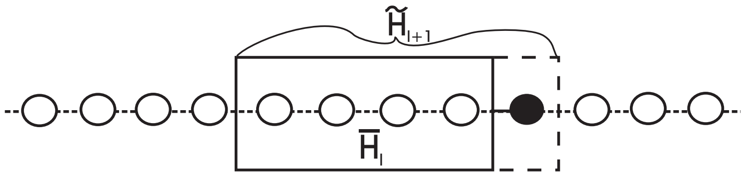

Figure 3.1: A depiction of the NRG procedure

3.2.2 Numerical Renormalization Group

The DMRG algorithm has been developed from the numerical renormalization group (NRG). The goal of NRG is to determine ground state properties of 1-dimensional systems. We can consider an infinite 1D-Hubbard chain, for instance. Then an NRG procedure proceeds as follows:

1. Isolate a portion of the system containing L sites. Here L is chosen to be small enough so that the Hamiltonian H_L can be diagonalized exactly (Fig.3.1).

2. Diagonalize H_L numerically, obtain the m lowest eigenvalues and eigenvectors.

3. Transform H_L and other operators in the "block" of length L to a new basis consisting of the m lowest eigenvectors of H_L, i.e. form $\rightarrow \overline{H_L}$. Note that $\overline{H_L}$ is a diagonal matrix with m elements.

4. Add a site to $\overline{H_L}$ to form $\widetilde{H}_{L+1}$. In order to do this, the interaction between the block of length L and the additional site added must be reconstructed.

5. Repeat starting with step 2, substituting $\widetilde{H}_{L+1}$ for H_L (Fig.3.2).

Generally we iterate this process until the result converges. The advantage of NRG is that the number of states m kept at each step is held constant. So time and memory required for each diagonalization stay the same, and the computer time needed is linear in L. As a consequence we can treat bigger systems.

The big disadvantage of the method is that it works only for very special cases. To keep the advantages and to remove the disadvantages we need a procedure which selects a better set of m states to which we restrict our Hamiltonian (step number 2). DMRG constitutes such a procedure by doing a density matrix projection.

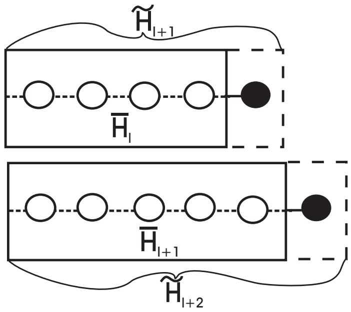

Figure 3.2: A depiction of the NRG procedure, when it starts to repeat

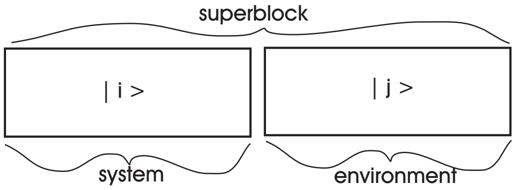

Figure 3.3: A superblock divided into a system and an environment block

3.2.3 Density Matrix Projection

This subsection explains the main ideas of the density matrix projection. Again we consider an isolated portion of the system, which we can diagonalize exactly. We call this small system "superblock". In the next step we divide the superblock into a "system block" and an "environment block" (Fig.3.3). The basis of the system block is described by states $|i\rangle$ and the the basis of the environment block by states $|j\rangle$. Now we calculate the ground state and express the result by vectors of the system and of the environment block:

$$|\psi\rangle = \sum_{ij} \psi_{ij} |i\rangle \otimes |j\rangle \tag{3.30}$$

The density operator belonging to $|\psi\rangle$ is given by:

$$\hat{\rho} = |\psi\rangle\langle\psi|. \tag{3.31}$$

Now we introduce a reduced density operator, which only affects the system block. We achieve this operator by calculating the trace with the basis vectors $|j\rangle$ of the environment block (Equation 3.32).

$$\underbrace{\hat{\rho}^r = \sum_j \langle j|\hat{\rho}|j\rangle}_{\text{operator notation}} \Rightarrow \underbrace{\rho^r_{ii'} = \sum_j \psi_{ij}\, \psi^*_{i'j}}_{\text{matrix notation}} \tag{3.32}$$

Now we want to define a procedure for producing a set of states for the system block $|u^\alpha\rangle$, $\alpha = 1, ..., m$, with $|u^\alpha\rangle = \sum_i u_i^\alpha |i\rangle$, which is optimal for representing ψ in some sense. Due to the fact that we only allow m states, we cannot represent $|\psi\rangle$ exactly, if $l > m$, when l is the number of system block states $|i\rangle$. We want to construct an accurate approximation for $|\psi\rangle$ by

$$|\psi\rangle \approx |\overline{\psi}\rangle = \sum_{\alpha,j} c_{\alpha,j} |u^\alpha\rangle |j\rangle. \tag{3.33}$$

In other words, we wish to minimize

$$S = \left| |\psi\rangle - |\overline{\psi}\rangle \right|^2 \tag{3.34}$$

by varying over all $c_{\alpha,j}$ and u^α, subject to $\langle u^\alpha | u^{\alpha'} \rangle = \delta_{\alpha\alpha'}$.

If we solve this problem[4], we obtain the following result: We can minimize S if we diagonalize the reduced density matrix (Equation 3.32). The eigenstates of $\hat{\rho}^r$ with the m lowest eigenvalues determine the optimal reduced basis with the states $|u^\alpha\rangle$. With this knowledge we can form a more effective method than NRG. This method is called DMRG (density matrix renormalization group) and is a combination of density matrix (DM) projection and numerical renormalization group (NRG).

3.2.4 Infinite System Algorithm

The infinite system algorithm is the most straightforward extension of NRG. It works for infinite systems with reflection symmetry and forms the easiest DMRG procedure. The superblock configuration for L sites is shown in figure 3.4. There $\overline{H}_l$ is the Hamiltonian of the system block in the reduced basis and the solid dots represent single sites. The right block $\overline{H}_l^R$ is formed by relabeling the sites in the system block so that they are reflected onto the right part of the lattice. This block forms the environment block. The finite system algorithm then proceeds as follows (Fig.3.4):

1. Form a superblock containing L sites which is small enough to be exactly diagonalized.

2. Diagonalize the superblock Hamiltonian H_L^{super} numerically, obtaining only the ground state eigenvalue and eigenvector $|\psi\rangle$ using the Lanzcos or Davidson algorithm.

[4]For details we refer to reference [12].

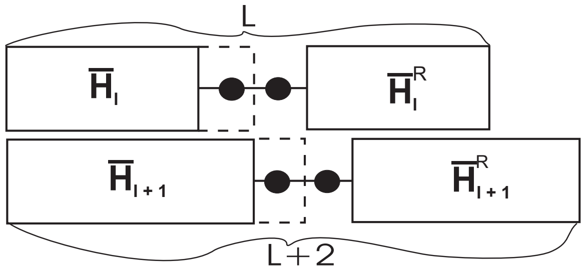

Figure 3.4: A depiction of the infinite system algorithm

3. Form the reduced density matrix $\rho_{ii'}$ for the new system block from $|\psi\rangle$ using equation 3.32. Note that $l' = l = L/2 - 1$.

4. Diagonalize $\rho_{ii'}$ with a dense matrix diagonalization routine to obtain the m eigenvectors with the largest eigenvalues.

5. Construct H_{l+1} and other operators in the new system block and transform them to the reduced density matrix eigenbasis to obtain $\overline{H}_{l+1}$.

6. Form a superblock of size $L+2$ using $\overline{H}_{l+1}$, two single sites and $\overline{H}_{l+1}^R$.

7. Repeat starting with step 2, substituting H_{L+2}^{super} for H_L^{super}.

Although this procedure is very similar to NRG, it includes the big advances of the density matrix projection. Nevertheless the infinite system algorithm has to be stopped at some size because of bad convergence. As a consequence the ground state is not accurate. This problem can be solved by the finite system algorithm, which allows to get iteration convergence to the ground state.

3.2.5 Finite System Algorithm

The finite system algorithm represents a possibility to treat finite systems by DMRG more efficiently. It is similar to the infinite system algorithm, but now the environment block is chosen in a different way: It is chosen so that the size of the superblock is kept fixed at each step. Suppose that we have run the infinite system algorithm until the superblock reaches size L, but have stored all the $\overline{H}_{l'}^R$ for $l' = 1, ..., L/2 - 2$ as well as all the additional operators to build up the system block. Then we can continue to build up the system block, but keep $L = l + l' + 2$ fixed by using the appropriate previously stored $\overline{H}^R_{l'}$. The finite size algorithm then proceeds as follows (Figure 3.5):

1. Carry out the infinite system algorithm until the superblock reaches size L, storing $\overline{H}^R_l$ and the operators needed to connect the blocks at each step.
2. Carry out steps 3-5 of the infinite system algorithm to obtain $\overline{H}_{l+1}$. Store it. (Now $l \neq l'$.)
3. Form a superblock of size L using $\overline{H}_{l+1}$, two single sites and $\overline{H}^R_{l'-1}$. The superblock configuration is given by first picture of figure 3.5, where $l' = L - l - 2$.
4. Repeat steps 2-3 until $l = L - 3$ (i.e. $l' = 1$). This is the left to right phase of the algorithm (second picture of figure 3.5).
5. Carry out steps 3-5 of the infinite system algorithm, reversing the roles of $\overline{H}_l$ and $\overline{H}^R_{l'}$, i.e. switch directions to build up the right block and obtain $\overline{H}^R_{l+1'}$ (third picture of figure 3.5). Store it.
6. Form a superblock of size L using $\overline{H}_{l-1}$, two single sites and $\overline{H}^R_{l'+1}$.
7. Repeat steps 5-6 until $l = 1$. This is the right to left phase of the algorithm.
8. Repeat starting with step 2.

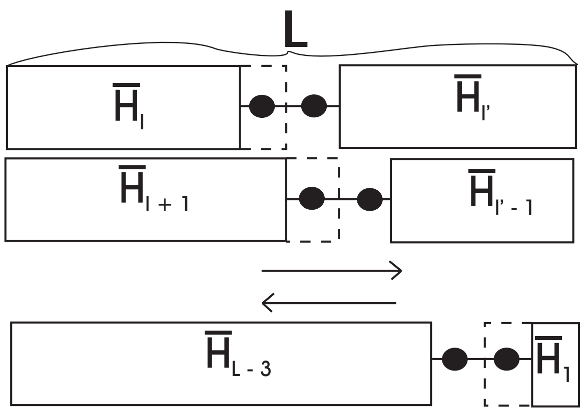

Figure 3.5: A depiction of the finite system algorithm

This procedure runs like a zipper repeatedly from left to right and then right to left through a superblock that is always of the same size. Each time the zipper changes direction, a new set of stored blocks is used as the environment block. In this way, the representations of the stored blocks are iteratively improved and the zipping can be repeated until convergence is reached.

3.2.6 Ladders and 2D-lattices

The restriction to 1D-lattices is very discontenting. Modifications to DMRG have been developed which allow to treat lattices with a nearly 1D-structure too. The single and coupled ladder systems, which we investigate in this thesis, are examples of such structures.

In principle these modified DMRG algorithms work in two steps. First the ladder is mapped on a 1D-chain like it is demonstrated in figure 3.6 and afterwards a finite system algorithm is carried out for this chain.

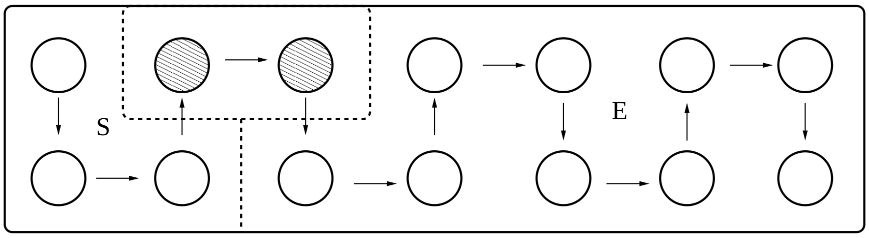

Figure 3.6: Schematic representation of the mapping of a ladder on a 1D-chain. The arrows indicate the direction in which the DMRG algorithm is iterating through the lattice. The system block (**S**) and the environment block (**E**) are indicated by letters.

These algorithms can be extended to more two-dimensional systems. The disadvantage in this context is the worsening of convergence, because the sites in a 2D-lattice interact with sites far away in the 1D-DMRG-chain (Figure 3.7). In practice the number of sites in x-direction must be strongly (more than linear) reduced for an extension in y-direction. Nevertheless four chains (two coupled ladders) like used in this thesis can be treated quite well by DMRG.

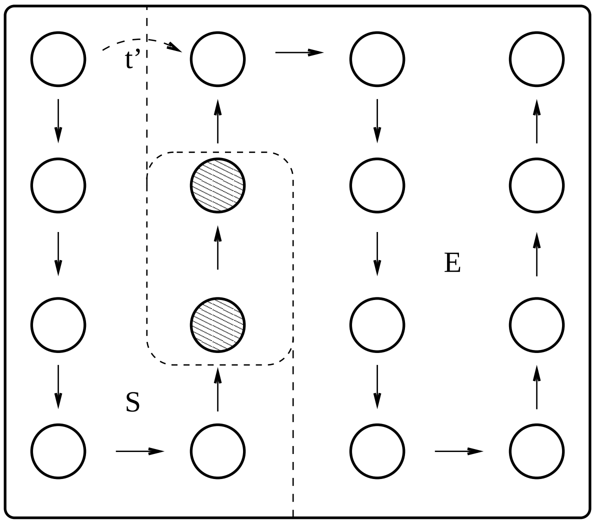

Figure 3.7: Schematic representation of the mapping of a 2D-lattice on a 1D-chain. One sees that neighboring sites in the 2D-lattice can be far away from each other in the 1D-DMRG-chain.

3.3 Simulated Annealing and Tempering[5]

In this thesis we include terms in the Hubbard model to describe the coupling between electrons and lattice distortions[6] which are external parameters to the quantum Hamiltonian of the electrons. We need to calculate the absolute ground state of this system, i.e. the state with the minimum energy as a function of distortions. We will do this with the help of a Monte Carlo procedure.

The most popular method to approach such minimization tasks is Simulated Annealing [53, 54]. However, Simulated Annealing [55] contains the risk to pass the global minimum and to get only a local minimum. As a consequence we will use Parallel Tempering [56, 10] to solve this problem. Tempering is related to Simulated Annealing, but reduces the risk to find only a local minimum instead of the global minimum.

3.3.1 Simulated Annealing

The concept behind Simulated Annealing is borrowed from physics, specifically from thermodynamics. The method copies the way liquids freeze and crystallize during an annealing process. At high temperatures the particles can move freely. Differences of potential energies of various configurations are overcome by the particles due to their high kinetic energy. When the liquid is cooled down slowly, an ordering process sets in, thermal mobility is lost and some final configuration (e.g. an ideal crystal) is obtained. Ideally this is a configuration where the cost function (free energy) attains its absolute minimum. In this context we face the problem that the liquid is possibly cooled down too quickly. As a consequence the system can end up in some local minimum of energy (meta-stable) instead of becoming an ideal crystal. This corresponds to a poly-crystalline or amorphous state. For our minimization task, as we are interested in finding a global minimum, we try to simulate a slow cooling process on the computer. So we introduce an artificial temperature T and a probability distribution

$$p_E(\mathbf{x}|T) = \frac{1}{Z} e^{-H(\mathbf{x})/T} \tag{3.35}$$

$H(\mathbf{x})$ denotes the cost function which must be minimized and can depend on a set of variables $\mathbf{x}$ that is either discrete or continuous. The quantity Z

[5]This section often follows references [10] and [53].
[6]See subsection 2.3.4.

is the normalization factor and corresponds to the partition function of the canonical ensemble.

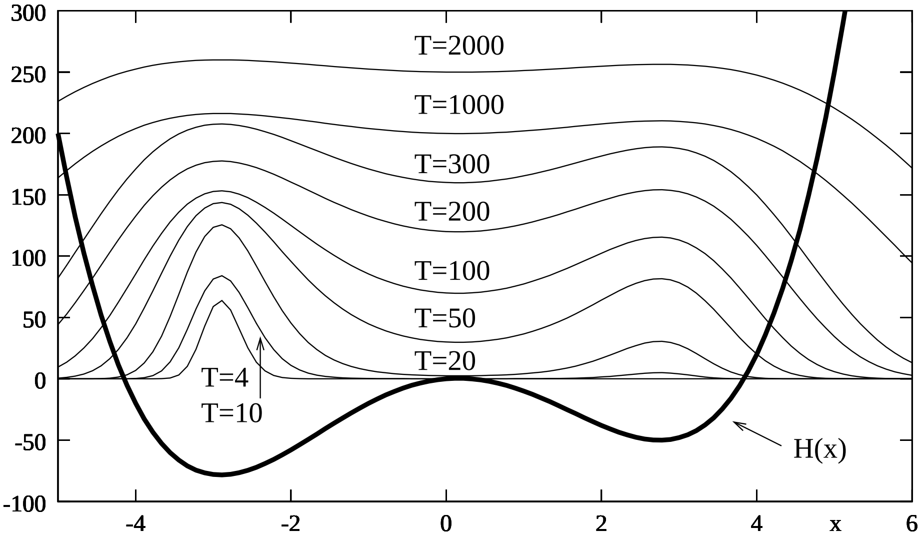

Figure 3.8: The Figure displays a cost function $H(\mathbf{x})$ (Equation 3.36) and the Boltzmann distribution $p_E(\mathbf{x}|T)$ (Equation 3.35) at different temperatures T.

For instance, we can consider the cost function

$$H(x) = x^4 - 16x^2 + 5x \tag{3.36}$$

to get a better understanding for this method. The extrema of this example have the coordinates

x	$H(x)$
-2.9035	-78.3323
0.1567	0.3912
2.7468	-50.0589

Figure 3.8 displays the cost function $H(x)$ and the Boltzmann distribution $p_E(x|T)$ for various temperatures T. At temperatures much higher than the potential barrier $T \gg 50$ the Boltzmann distribution is rather flat. As soon as the temperature is lower than the potential barrier, e.g. $T = 20$, the probability in the barrier is almost zero and two separate peaks develop. If the temperature is even lower than the difference of the two minima, e.g. $T = 10$, the probability in the local minimum becomes negligible and the probability is concentrated merely around the global minimum.

The purpose of the distribution p_E is to assign high probability to states $\mathbf{x}$, where $H(\mathbf{x})$ is small, i.e. near the global minimum. As a consequence a random walker will spend a long time near the optimum states. In addition the walker can also go back to higher values of $H(\mathbf{x})$ and leave a local minimum. The probability for this process is determined by the temperature. Thus simulated annealing constitutes an improvement to methods which do not contain a possibility to escape a local minimum.

When we calculate the expectation value of H for a certain temperature we get

$$\langle H \rangle_T = \int_{\mathbf{x}} p_E(\mathbf{x}|T) H(\mathbf{x}). \tag{3.37}$$

The minimum of H as well as the corresponding state $\mathbf{x}$ are found by cooling

$$\min H(\mathbf{x}) = \lim_{T \to 0} \langle H \rangle_T \tag{3.38}$$

$$\mathbf{x_{min}} = \lim_{T \to 0} \max_{\mathbf{x}} .p_E(\mathbf{x}|T) \tag{3.39}$$

If we implement a Simulated Annealing algorithm we must focus on three steps (generation of states, acceptance of states, cooling scheme).

First we discuss the **Generation of states**. In the vicinity of the current point $\mathbf{x_n}$ we create a trial point $\mathbf{x}_t$ at random. A typical probability distribution of $\mathbf{x}_t$ is given by a Gaussian

$$p_{\mathbf{x}}(\mathbf{x}_t - \mathbf{x}_n) \propto \prod_i e^{-(\mathbf{x}_{t,i} - \mathbf{x}_{n,i})^2/(2{\sigma_i}^2)} \tag{3.40}$$

Note that $\mathbf{x}_{n,i}$ is the i-th component of the vector $\mathbf{x}_n$ which contains the set of parameters in which the function has to be minimized.

The second step is the **Acceptance of states** where we use the Metropolis probability

$$q = min\{1, \frac{p_E(\mathbf{x}_t|T)}{p_E(\mathbf{x}_n|T)}\} \tag{3.41}$$

with which the new position will be accepted. That means that if $q = 1$ we always accept and if $q < 1$ we draw a pseudo random number r from a uniform distribution in the interval $[0, 1)$. For $r < q$ we accept the $\mathbf{x}_t$ as the new state $\mathbf{x}_{n+1}$. Otherwise the old state is kept and we assign $\mathbf{x}_{n+1} = \mathbf{x}_n$. In this way we obtain a series of points $\mathbf{x}_i$ which form a Markov Chain $(\mathbf{x}_1, \mathbf{x}_2, \mathbf{x}_3, ..., \mathbf{x}_n)$. That means that

$$P(\mathbf{x}_{n+1}|\mathbf{x}_n, \mathbf{x}_{n-1}, ..., \mathbf{x}_1) = P(\mathbf{x}_{n+1}|\mathbf{x}_n). \tag{3.42}$$

So the probability to pass to $\mathbf{x}_{n+1}$ only depends on the current point $\mathbf{x}_n$ and not on the history of the walker. It can be shown that the trajectory of the random walker reproduces the probability distribution

$$\lim_{N\to\infty} \frac{1}{N}\sum_{i=1}^{N} \delta(\mathbf{x}-\mathbf{x}_i) = p_E(\mathbf{x}_n|T). \tag{3.43}$$

Furthermore this implies that the expectation values can be calculated by averaging over the Markov Chain.

$$\langle H(\mathbf{x})\rangle_T = \int_{\mathbf{x}} H(\mathbf{x}) p_E(\mathbf{x}_n|T) = \lim_{N\to\infty} \frac{1}{N}\sum_{i=1}^{N} \int_{\mathbf{x}} H(\mathbf{x})\delta(\mathbf{x}-\mathbf{x}_i) \tag{3.44}$$

$$= \lim_{N\to\infty} \frac{1}{N}\sum_{i=1}^{N} H(\mathbf{x}_i) \tag{3.45}$$

Last but not least we have to deal with the **Cooling scheme**. At every temperature T_k we let the walker do a fixed number n of steps. Then we lower the temperature according to a simple prescription. Of common use is the formula

$$T_k = T_0 q^k \tag{3.46}$$

with $q = 0.95$, for instance.

The disadvantage of Simulated Annealing is that all proposed cooling schemes include a considerable risk to become trapped into a local minimum. In this context Tempering provides us with an alternative.

3.3.2 Tempering Methods

Tempering methods [56] have been developed to correct the weaknesses of Monte Carlo methods which get easily trapped in a local minimum. So they also constitute an improvement of the simulated annealing algorithm.

Tempering arises from the same idea as Simulated Annealing. So we once more look at the annealing process of liquids. Errors in the crystals signify a meta stable state and only a local minimum of the cost function. These meta stable states can be removed if we heat the material above the transition temperature and cool it down afterwards. Now we have the possibility to repeat this process several times. In solid state physics errors in the structure of crystals are also removed in such a way.

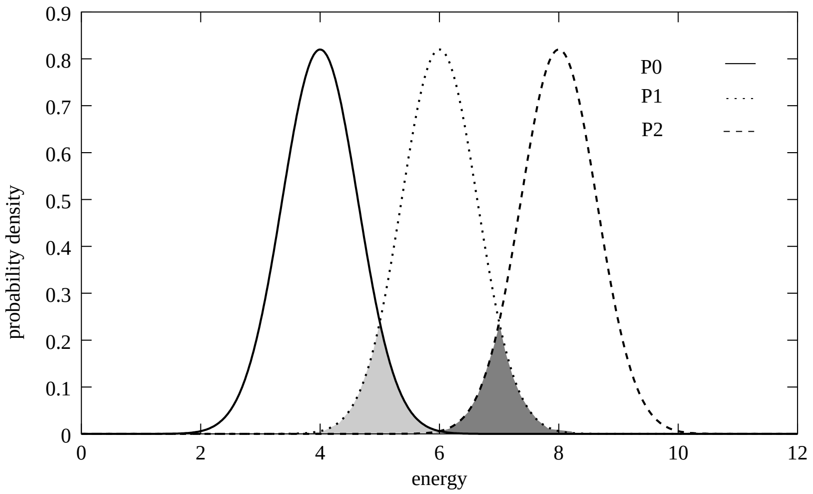

Figure 3.9: The overlap of energy distributions at different temperatures must be nonzero.

As a consequence the main idea of the tempering method consists of copying this process. This happens by treating the inverse temperature β as a dynamical variable. Instead of cooling down $T = \frac{1}{\beta}$ by a cooling scheme we introduce a sequence $\beta_0 < \beta_1 < ... < \beta_n$, where β_n denotes a sufficiently large inverse temperature. From time to time, a change in β is proposed and, if accepted, the updating continues at a new temperature. If the step is made to a lower β, a larger change in the configuration becomes possible.

A necessary condition for the efficiency of the method is a sufficient overlap of the energy distribution functions of β_i and β_{i+1}. Otherwise, a change in temperature would almost always be rejected. In the canonical ensemble, the distribution function depends only on the energy of each configuration. Here, the structure of the system enters through the density of states. In this case, the two-dimensional plot of figure 3.9 illustrates the minimal requirement. If the overlap (gray area in figure 3.9) is too small, states allowing a swapping are rare and the procedure fails.

There are two different approaches for the implementation of the ideas sketched above. "Simulated Tempering" methods use only one walker running through the phase space at different temperatures. After having performed at least one single sweep at β_i, let the walker be at the position $\mathbf{x}$. Now, we choose with equal probability whether to try to move to β_{i+1} or to β_{i-1}. If $i = 0$ or $i = n$, there is only one possible direction and a move in this direction is proposed with probability $\frac{1}{2}$. The step to adjacent temperature is accepted with the Metropolis-Hastings probability

$$\alpha_{i\rightarrow i\pm1} = min\{1, \frac{e^{-\beta_{i\pm1}H(x)+g_{i\pm1}}}{e^{-\beta_i H(x)+g_i}}\}. \tag{3.47}$$

In order to ensure an approximately random walk through all temperatures, the constants g_i, have to be tuned with delicate precision. Due the fact that an appropriate choice of these weights g_i is difficult, we prefer "Parallel Tempering" in this thesis and drop details on Simulated Tempering here.

"Parallel Tempering" methods consider a separate walker at each temperature allowing adjacent walkers to swap their positions from time to time. The composite Monte Carlo method is based on two different kinds of steps.

- Update the L copies of the system with a usual Metropolis sweep or a cluster algorithm.
- Swap the β values.

The swapping can be carried out as follows:

1. Propose to substitute the configuration at β_0 for that at β_1 and vice versa. Decide the acceptance of the swap by using the Metropolis method.
2. Propose to substitute the (possibly new) configuration at β_1 for that at β_2 and vice versa. Again, decision is made using the Metropolis scheme.
3. Continue this procedure for β_{i-1} and β_i until $i = L$.

It is very important for the efficiency of the method that only neighboring β values are proposed to be swapped. The Metropolis Hastings probability for swapping is given by

$$p_{swap} = \min\{1, \frac{\frac{1}{Z(\beta_{i+1})}e^{-\beta_i H(\mathbf{x}_{i+1})}\frac{1}{Z(\beta_i)}e^{-\beta_{i+1}H(\mathbf{x}_i)}}{\frac{1}{Z(\beta_i)}e^{-\beta_i H(\mathbf{x}_i)}\frac{1}{Z(\beta_{i+1})}e^{-\beta_{i+1}H(\mathbf{x}_{i+1})}}\}. \tag{3.48}$$

Therefore, the two partition functions $Z(\beta_i)$ and $Z(\beta_{i+1})$ cancel (which is a serious advantage in comparison to the Simulated Tempering method), and we obtain

$$p_{swap} = \min\{1, \frac{e^{-\beta_i H(\mathbf{x}_{i+1})-\beta_{i+1}H(\mathbf{x}_i)}}{e^{-\beta_i H(\mathbf{x}_i)-\beta_{i+1}H(\mathbf{x}_{i+1})}}\}. \tag{3.49}$$

This method is often used to investigate phase transitions. In our case we use it to find the global minimum of the function $H(\mathbf{x})$. Therefore we choose a sequence of inverse temperatures $\beta_0 < \beta_1 < ... < \beta_n$, which must fulfill several conditions:

- Due to the fact that the overlap of energy distributions at different temperatures must be large enough, the difference between adjacent β-values has to be sufficiently small.
- The "Parallel Tempering" procedure must provide an approximately Random walk in β which moves between low and high temperatures often enough, so that one escapes every local minimum and covers the whole phase space.
- We have to choose a sufficiently large β_n (respectively a small temperature).

If we fulfill these conditions we can apply the ideas ($T \to 0$ and $\beta \to \infty$) of subsection 3.3.1 (See equations 3.38, 3.39 and 3.44, 3.45) to get the lowest energy. In other words, the expectation value at the lowest temperature (highest β) converges with a high probability to the exact minimum.

Chapter 4

Ordering pattern of lattice distortions

In this chapter we investigate the pattern of lattice distortions in the ground state of the model described in subsection 2.3.4. This model includes the coupling of the electrons to static lattice distortions. The Hamiltonian is given by equation 2.6 and contains a set of independent distortions z_i. To obtain the absolute ground state of equation 2.6 we have to find the set of distortions z_i which minimize the ground state energy. Thus, we search for the optimal set of distortions first. Afterwards the resulting (purely zig-zag) pattern will be used in the chapters 5 and 6 for DMRG calculations on much bigger systems.

In the sequel, we will use the parallel tempering method (described in section 3.3) to evidence that the distortions are zig-zag ordered in the ground state. As a consequence this approach eliminates the constraints made by reference [39]. There zig-zag distortions have been assumed a priori which reduces the independent z-values to one[1]. In each Monte Carlo step we diagonalize the resulting Hamiltonian with a Lanczos routine to obtain the ground state energy of the corresponding configuration. Moreover, the parallel tempering routine allows swaps of the configurations to another temperature (inverse temperature β). Thus "β" here is a fictitious inverse temperature, introduced only to allow the set of distortions z_i to reach its optimal pattern, while the electronic energy is always calculated in the $T = 0$ ground state.

Due to the fact that the Lanczos method is restricted to small systems we are just able to handle systems with a maximum of 16 sites. Moreover, the

[1] See subsection 2.3.4 and equation 2.9 for details.

number of tempering steps increases linearly with the number of sites in the system and the number of discrete temperatures in the procedure. As a consequence we only use the parallel tempering method for single ladders with 4 and 6 rungs which means 8 and 12 sites in the system. For systems[2] consisting of one ladder with 8 rungs and two coupled ladders with 4 rungs we do not use tempering, but only one very low temperature. Certainly this increases the risk to become trapped in a local minimum, but the results obtained from the smaller systems help to interpret the output of these calculations. For coupled ladders we must perform further calculations to be secure of how the distortions order.

4.1 Distortions for a single ladder

For the systems consisting of a single ladder we use periodic boundary conditions in b-direction and the parameters quoted in subsection 2.3.2. Due to the fact that the nearest neighbor repulsion V is not known well, we investigate the system for different values of these parameters.

V	0.0	0.5	1.0	1.5	2.0	2.5	3.0

Table 4.1: We execute parallel tempering for this set of nearest neighbor repulsions V for systems of size 4×2 and 6×2.

Moreover we choose seven discrete temperatures for our tempering procedure. Their inverse values are specified in table 4.2.

β	50	100	200	400	1000	3000	10000

Table 4.2: Inverse tempering temperatures $\beta = 1/T$ for the parallel tempering procedure for systems of size 4×2 and 6×2.

Before we present the results we will demonstrate the time evolution of a parallel tempering process by an example. We choose the system of size 4×2 with a nearest neighbor repulsion $V = 0.5$. In figure 4.1 we consider one of the seven configurations of the parallel tempering process and plot a part of the time evolution. The upper plot shows the tempering temperature as a function of the swapping step. The configuration walks through all different

[2]These systems consist of 16 sites.

discrete temperatures. The energy per site at each swapping step is plotted below. One sees that at low temperatures (high inverse temperature β) the energies become very small and vary unspectacularly. There the configuration is situated near a minimum. The parallel tempering routine sometimes allows the configuration to walk back to higher temperatures. Then the configuration can move to higher energies too and can escape local minima in that way.

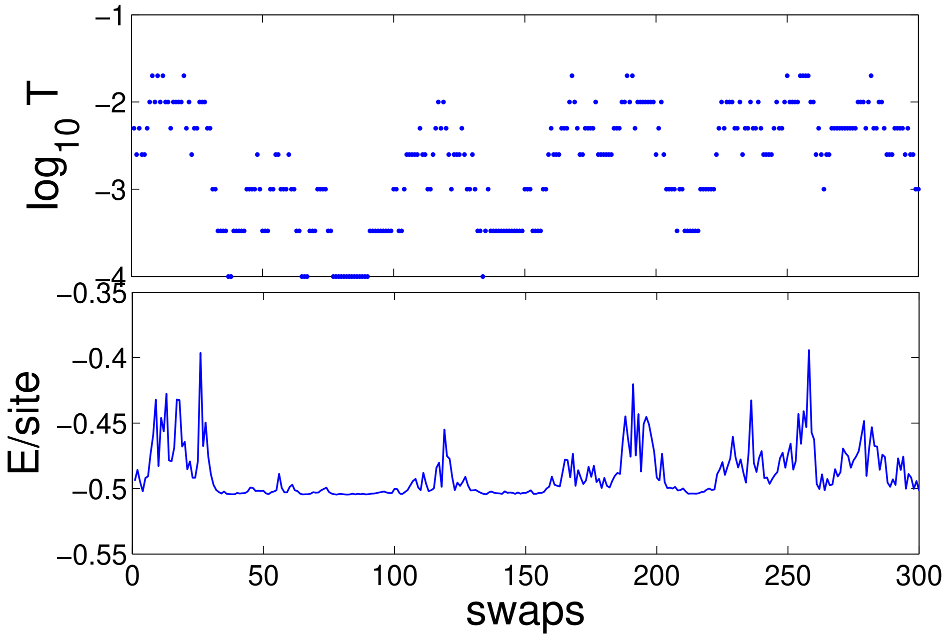

Figure 4.1: Energy per site and tempering temperature as a function of the swapping step for a configuration of size 4×2 with a nearest neighbor repulsion $V = 0.5$.

We calculated these time evolutions up to 600 swaps for systems of size 4×2 and up to 100 swaps for systems of size 6×2. Between each swapping we executed 10 to 20 updates on each site. For all V-values the configuration at lowest temperature (highest inverse temperature $\beta = 10000$) varies unspectacularly around the same energy per site. These configurations are always situated near the global minimum of energy and should provide a good approximation for the ground state of the Hamiltonian 2.6 introduced in section 2.3.4. Figure 4.2 illustrates this for the system of size 4×2 at a V-value of 1.5. All other calculations, at different V and/or different lattice size show the same features. The solid line shows the energies of a specific configuration which walks around at different temperatures. The dashed line shows the energy of the configuration with the lowest temperature at this swapping step. As a consequence the lines agree with each other if the "not-dashed" configuration is also at the lowest temperature. For a better understanding of this process we refer to subsection 3.3.2.

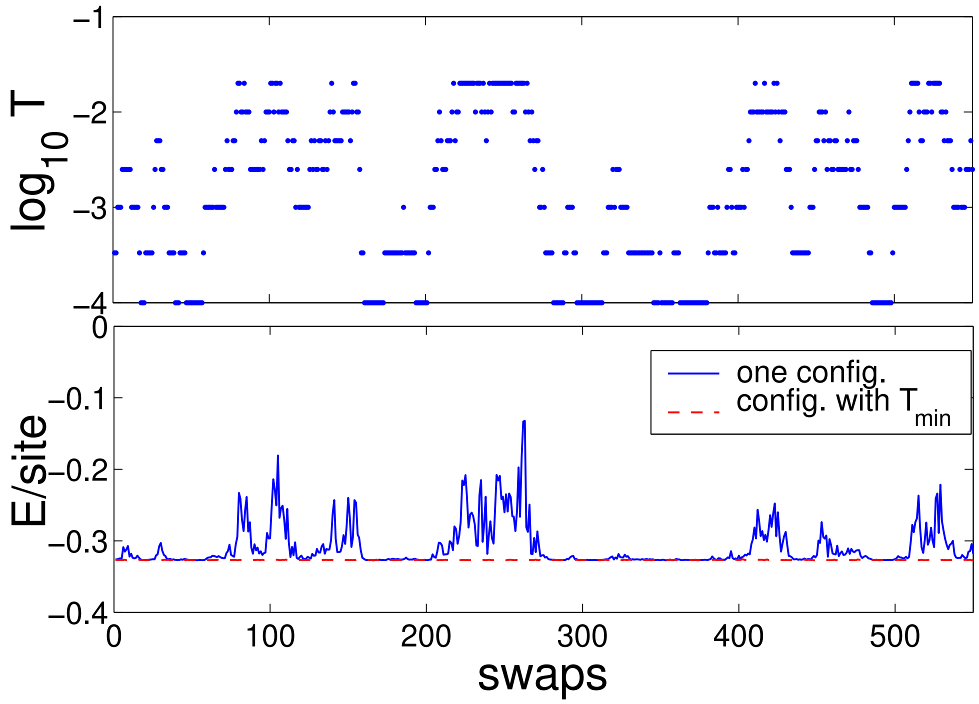

Figure 4.2: Energy per site and tempering temperature as a function of the swapping step for a configuration (solid line) of the system of size 4×2 with a nearest neighbor repulsion $V = 1.5$. The dashed line always shows the energy of the configuration which is currently at the lowest temperature in the parallel tempering set of configurations.

Now we concentrate on configurations at the lowest temperature which should give a good approximation of the ground state. First we consider the distortions for different V-values. They are plotted for the 4×2-system in figure 4.3 and become nearly 0 for V-values smaller than 1. At $V = 1$ the single peak at $z = 0$ splits into two symmetric peaks. Thus there are finite distortions at $V \geq 1$ in each configuration. In order to investigate their spatial pattern we examine the static distortion structure factor $S_{DO}(\mathbf{q})$ which has been defined in equation 2.12. We calculate $S_{DO}(\mathbf{q})$ for all momenta $\mathbf{q}$ at each time step of the simulation at the lowest temperature. In figures 4.4 and

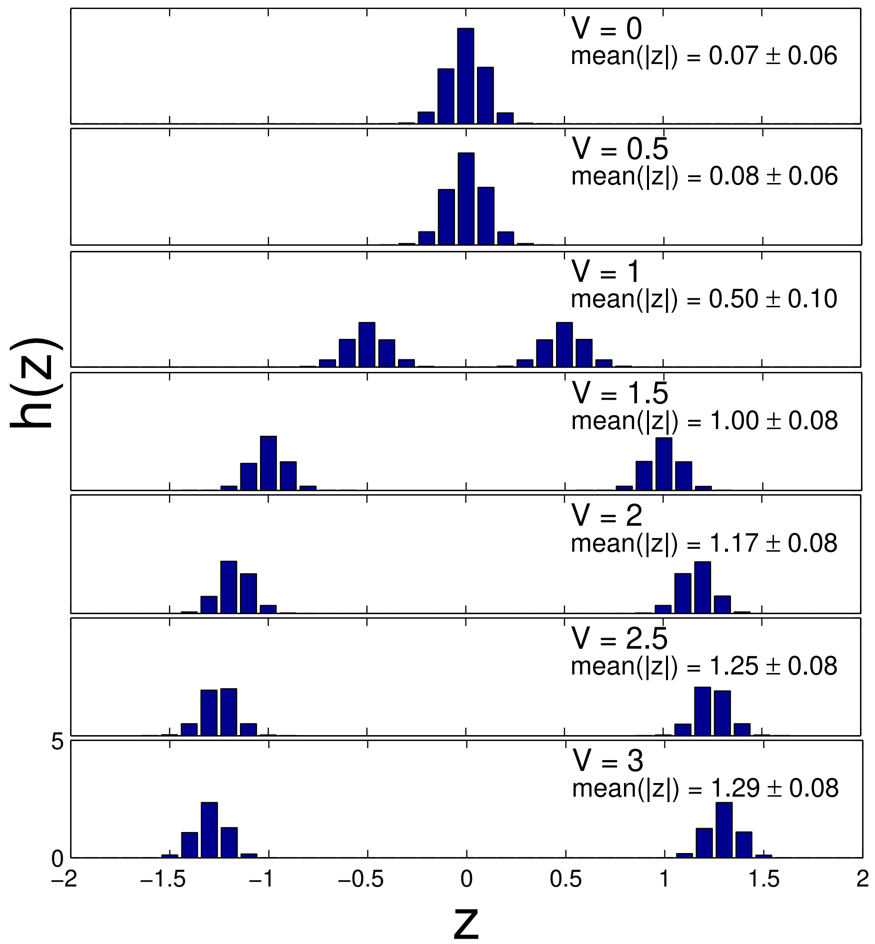

Figure 4.3: Distortions on all sites and at all time steps are plotted in a histogram which shows their frequency. Size of the system: 4×2.

4.5 we plot the $S_{DO}(\mathbf{q})$-values for every momentum in a separate histogram, which shows the their frequency.

The results allow a clear interpretation: For V-values lower than 1 all structure factors vanish. Thus the distortions vanish up to small uncorrelated fluctuations (see figure 4.3). For higher V-values the structure factor at $\mathbf{q} = (\pi, \pi)$ is finite whereas it still vanishes at all other momenta. Thus the system orders in a pure zig-zag pattern, both at size 4×2 and 6×2.

For the system with 8 rungs (16 sites) we used only one very low temperature ($T = \frac{1}{3000}$). As a consequence there is the risk to become trapped in a local minimum. But due to the fact that there don't seem to be dangerous local minima for smaller systems (4×2 and 6×2) we can assume this for this system (8×2), too. So we proceed like in figure 4.4 and figure 4.5 to obtain figure 4.6, which then shows the same features like the others. In addition this is confirmed by the energy evaluation in figure 4.7, where the energies at different Monte Carlo steps are depicted. For V-values 0.0, 0.5 and 1.0 the energies vary only in a small range. Moreover one doesn't find a lower energy than the starting energy, where all distortions are chosen equal zero. So the system starts at the optimal configuration and stays in the area of this optimal configuration of distortions. For the higher V-values one sees clearly that the starting configuration isn't optimal. As a consequence the Monte Carlo simulation iterates to configurations with lower energies, which possess zig-zag lattice distortions. There the energy varies only in a small range, which means that a minimum is nearly reached.

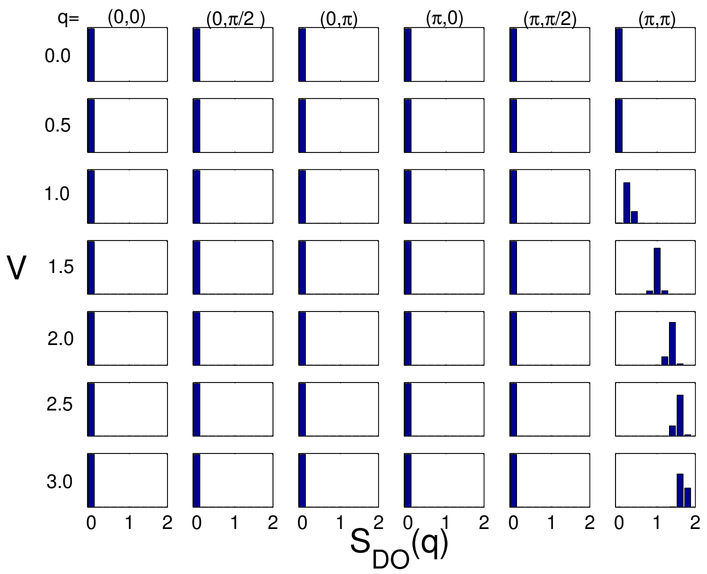

Figure 4.4: Frequency of the $S_{DO}(\mathbf{q})$-values for each V-value and each momentum $\mathbf{q}$. Size of the system: 4×2.

To sum up we can say that our parallel tempering calculations clearly indicate a pure zig-zag pattern for the Hamiltonian in equation 2.6 with the model parameters of subsection 2.3.2 for $V \geq 1$, whereas the distortions fluctuate in a small range around zero for smaller V. As a consequence we can from now on restrict all calculations on single ladders to a pattern of zig-zag distortions, as indicated in equation 2.9.

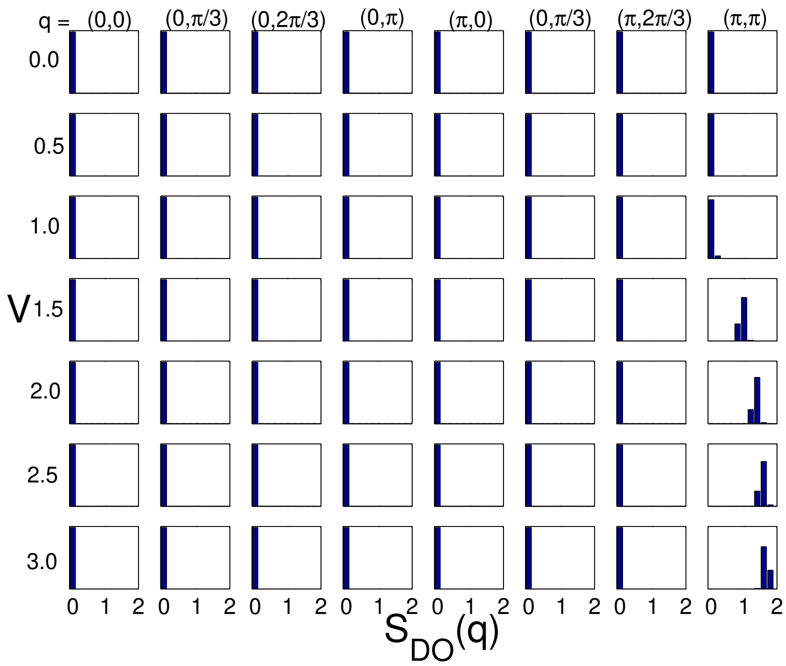

Figure 4.5: Frequency of the $S_{DO}(\mathbf{q})$-values for each V-value and each momentum $\mathbf{q}$. Size of the system: 6×2.

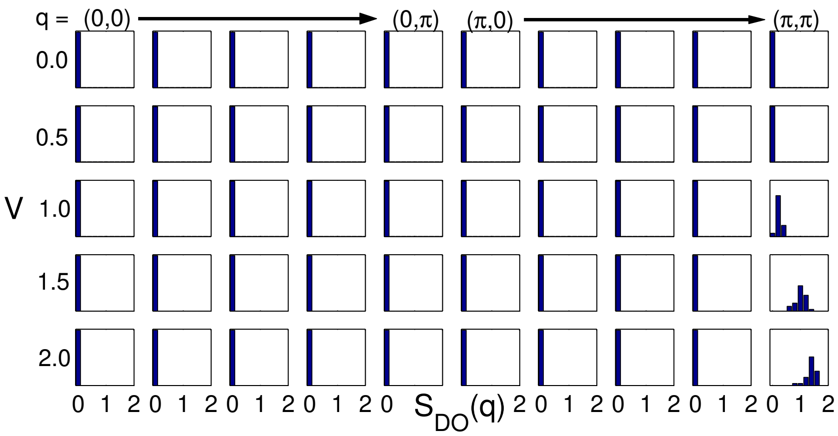

Figure 4.6: Frequency of the $S_{DO}(\mathbf{q})$-values for each V-value and each momentum $\mathbf{q}$. Size of the system: 8×2.

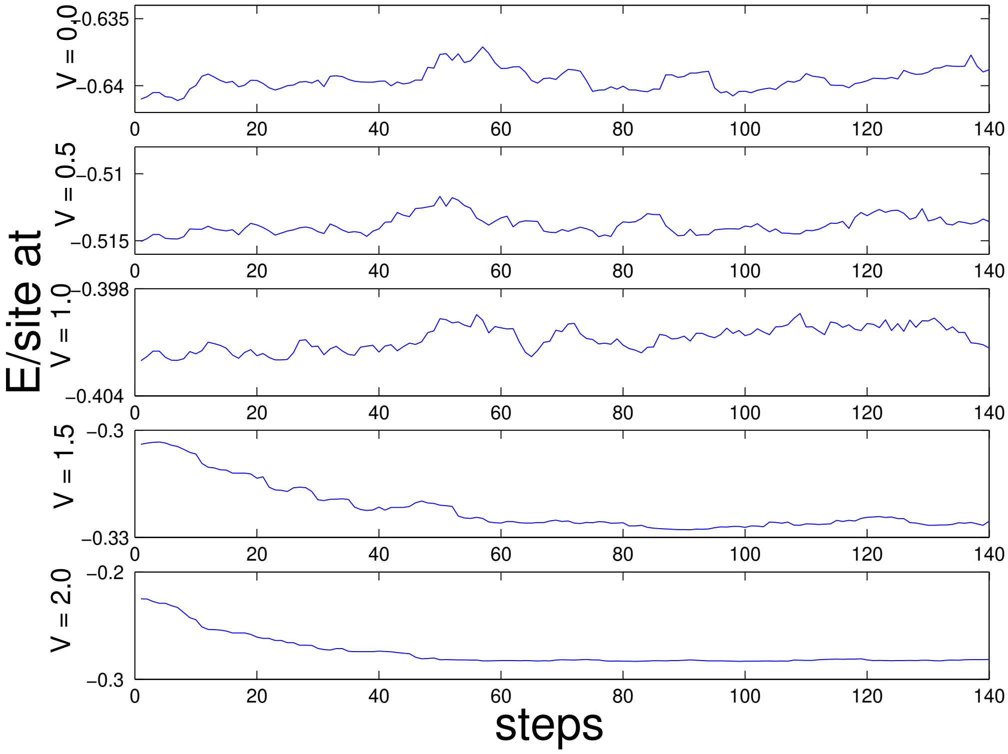

Figure 4.7: Energy per site as a function of the Monte Carlo time at different V-values. Only every fourth time step is plotted. Size of the system: 8×2.

4.2 Distortions for coupled ladders

Now we pay our attention to systems consisting of coupled ladders. Once more this contains the problem that we are restricted to a maximum of 16 sites per system with the Lanczos method. As a result we are just able to handle a system of two ladders with 4 rungs per ladder. For this system we use periodic boundary conditions in each direction and the model parameters quoted in subsection 2.3.2. We need to clarify the ordering pattern of distortions on each ladder, and whether both ladders order simultaneously.

Due to the fact that parallel tempering in systems of 16 sites is very time-consuming we must restrict ourselves to only one very low Monte Carlo temperature. We choose $T = \frac{1}{3000}$ and we carry out our calculations for V-values of $0.5, 1.0, 1.5$ and 2.0. The results are presented in figures 4.8, 4.9 and 4.10 and clearly show zig-zag ordering of the lattice distortions on both ladders simultaneously for the V-values 1.5 and 2.0. For V-values 0.5 and 1.0 one obtains a vanishing distortion structure factor for each momentum, which signifies vanishing distortions on each site too. The distortions have the same order of magnitude on each ladder. This follows from figure 4.9, which shows that the standard deviation is small in comparison to the absolute $S_{DO}(\mathbf{q})$-values at $\mathbf{q} = (\pi, \pi)$. The other distortion structure factors vanish for all V-values on each ladder and consequently their differences vanish too. Because the two ladders are equivalent, the data in figure 4.9 should be symmetric about zero. Deviations from this symmetry are an indication of the convergence of the Monte Carlo data.

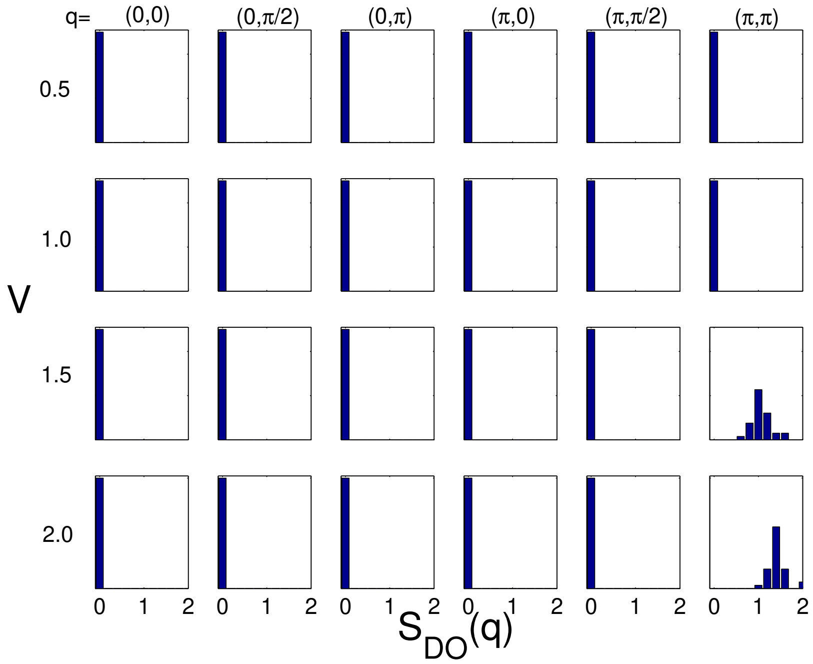

Figure 4.8: Frequency of the static distortion structure factor $S_{DO}(\mathbf{q})$ at the first ladder in the system $4 \times 2 \times 2$ as a function of the V-value and the momenta $\mathbf{q}$. (Monte Carlo simulation at $T = \frac{1}{3000}$)

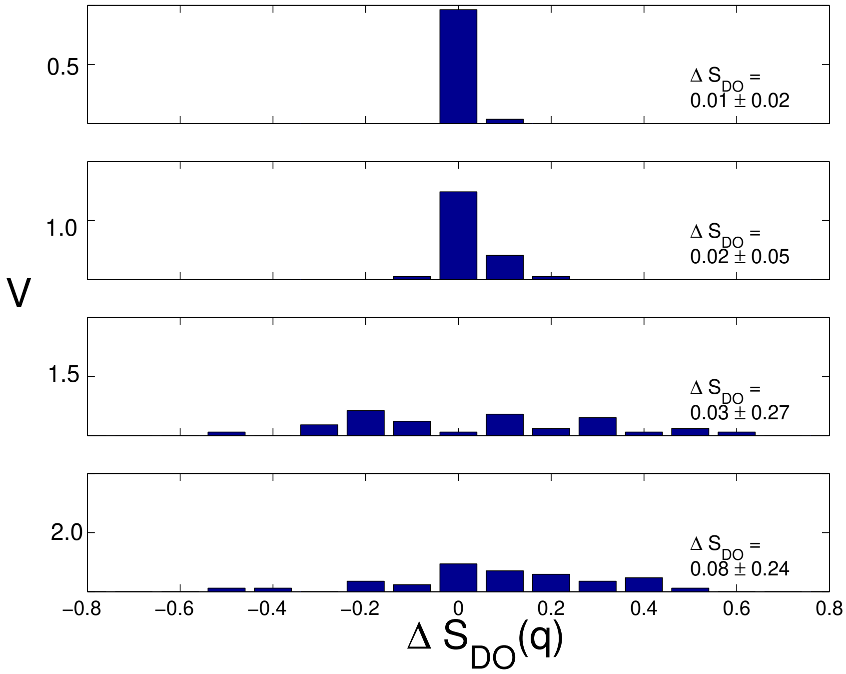

Figure 4.9: Frequency of the difference between the static distortion structure factor $S_{DO}(\mathbf{q})$ on the first and the second ladder of a $4 \times 2 \times 2$-system as a function of the V-value at the momentum $\mathbf{q} = (\pi, \pi)$. (Monte Carlo simulation at $T = \frac{1}{3000}$)

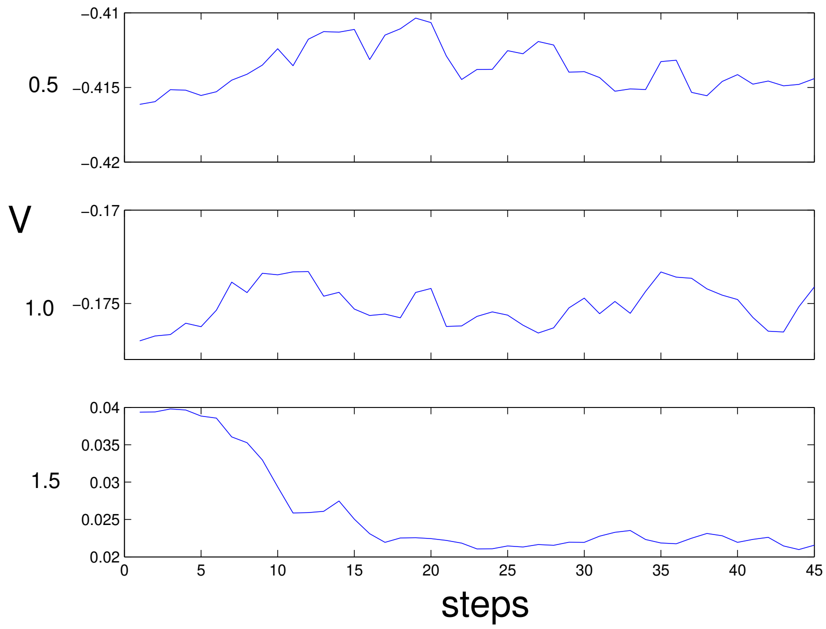

Figure 4.10: Time evolution of the energy in a Monte Carlo simulation for a system of size $4 \times 2 \times 2$ ($T = \frac{1}{3000}$). All distortions have been treated independently.

The starting configuration always consists of vanishing distortions on each site. Figure 4.10 shows that the system is situated in a minimum for $V = 0.0$ and $V = 0.5$ in the beginning, because energies only vary in a small range around the starting configuration, which has minimal energy. For $V = 1.5$ and $V = 2.0$ (not shown) the starting configuration has a relative high energy which is rapidly reduced by walking to zig-zag configurations of distortions. Having reached a nearly optimal zig-zag configuration, the energies again only vary in a small range. While this procedure cannot guarantee that the minimum obtained is a global one, the evidence for a purely zig-zag ordering pattern in each ladder is very strong. We conclude that we can reduce the configuration space for the distortions to two parameters, a zig-zag distortion of size z_1 for the first and of size z_2 for the second ladder.

With this reduced set of parameters we can perform a parallel tempering procedure with three discrete temperatures quoted in table 4.3 for V-values $0.5, 1.0, 1.5$ and 2.0. The results are summarized by figure 4.11, which shows

β	100	300	600

Table 4.3: Inverse tempering temperatures $\beta = 1/T$ for the parallel tempering procedure for systems of size $4 \times 2 \times 2$.

the distortions z_1 and z_2 as a function of the tempering time steps at the lowest tempering temperature. Together with figure 4.12 these results confirm the calculations above. For $V \leq 1.0$ one obtains vanishing distortions. For higher V-values one observes distortions with similar size on each ladder. We also see that the average distortion on each ladder is not symmetric about zero. Thus one should ideally have Monte Carlo runs which are much larger than these presented here, which took about two weeks each.

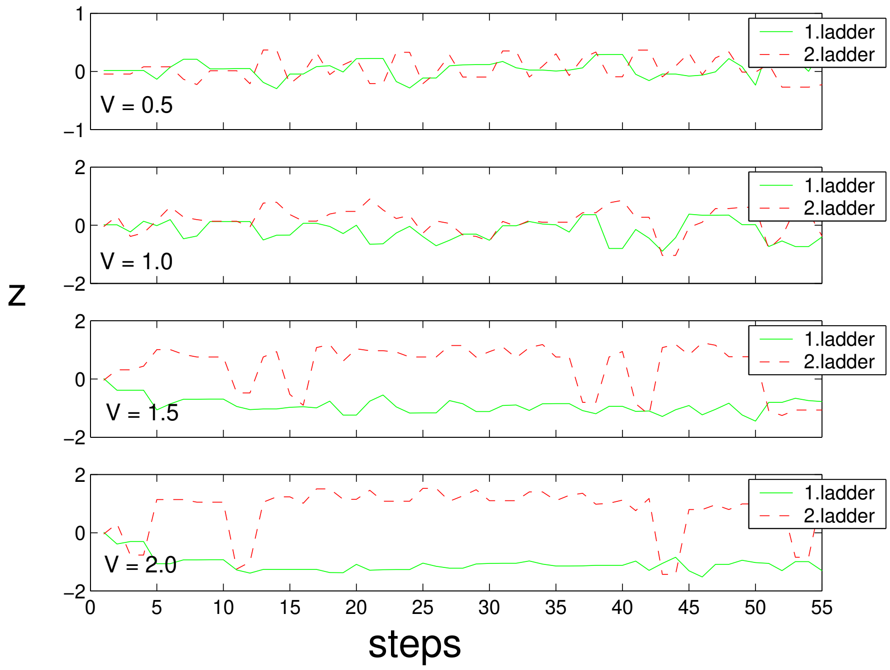

Figure 4.11: Zig-zag distortions for the first ladder z_1 and the second ladder z_2 as a function of the tempering time steps in the system $4 \times 2 \times 2$ for different V-values.

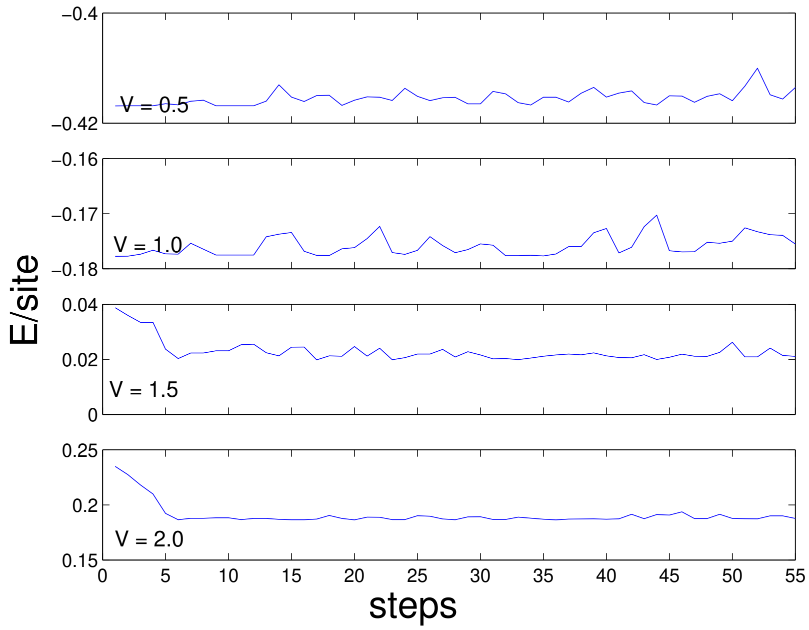

Figure 4.12: Energies per site in the system $4 \times 2 \times 2$ with fixed zig-zag distortions z_1 and z_2 on each ladder as a function of the tempering time steps.

To conclude this chapter we note that our calculations clearly show a zig-zag ordering pattern of the distortions in single ladders as well as in coupled ladders. Furthermore the distortions are of similar size on each ladder in coupled ladders systems. As a consequence we can henceforth calculate the ground state by assuming zig-zag lattice distortions on each ladder. This reduces the number of free parameters to one for one ladder and two for two coupled ladders, and we find the optimal state by plotting the energy as a function of these parameters. We finally compare the ground state energies of the two scenarios $z_1 = z_2 = z$ and $z_1 = z$, $z_2 = 0$. The results are shown in figure 4.13 where we see that the completely symmetric case always has lower energy than the completely asymmetric one. In the remaining DMRG calculations we therefore restrict the parameter space to a single parameter $z_1 = z_2 = z$.

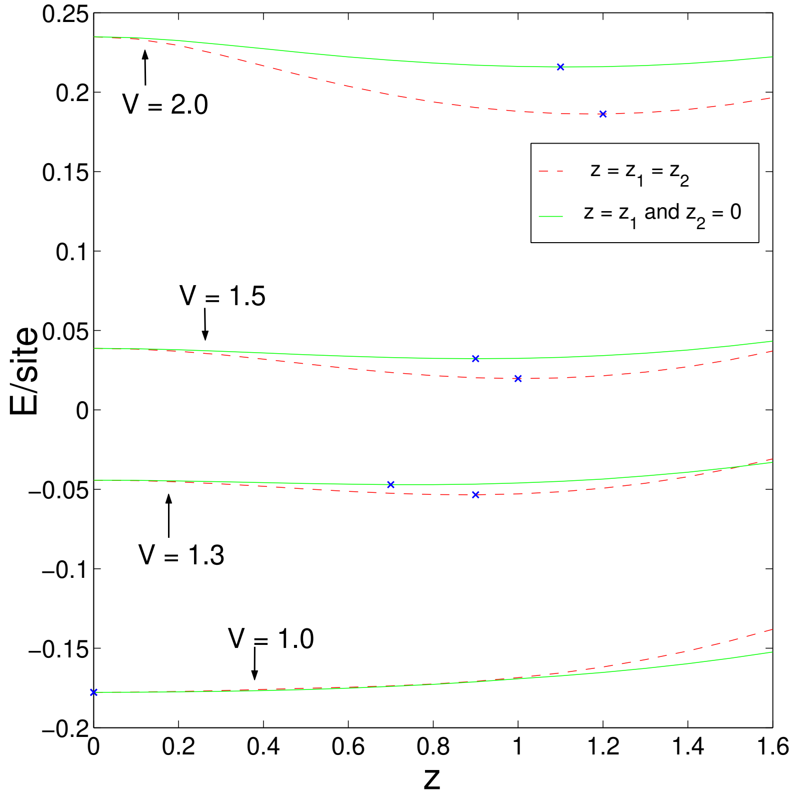

Figure 4.13: Energy per site as a function of the distortion z for four different V-values. Zig-zag distortions are assumed and we distinguish between the two cases $z_1 = z_2 = z$ (dashed line; both ladders have equal distortions) and $z_1 = z$, $z_2 = 0$ (solid line; only one ladder shows distortions). The crosses denote the points of minimal energy.

Chapter 5

Influence of electron-lattice interactions on single ladders

In this chapter we investigate the influence of zig-zag lattice distortions on the charge order parameter introduced in equation 2.11, for the case of single ladders. We also determine the effect on the spin gap. The model parameters have been selected as quoted in subsection 2.3.2. The calculations have been performed by DMRG which constitutes an enormous improvement compared to reference [39]. There the same calculations were performed with a Lanczos routine. As a consequence the authors could only treat systems up to 16 sites, where finite size effects considerably influence the results. Our DMRG calculations eliminate this limitation. We could handle systems up to 160 sites but we had to restrict ourselves to systems with open boundary conditions[1]. Technical aspects of the DMRG calculations are summarized in the appendix.

In the present section we first use the Hamiltonian in equation 2.1 to determine the order parameter without coupling to the lattice. In the next step we calculate the ground state of the Hamiltonian 2.6, which includes coupling to static lattice distortions. We perform both calculations for different lattice sizes and do a finite size scaling in the end. To sum up we discuss the differences between the two results.

[1]See subsection 2.3.3 for a description of the different boundary conditions.

5.1 Ground state properties without electron-lattice interactions

In this section we determine the ground state properties of the Hamiltonian in equation 2.1. We concentrate on the charge order parameter m_{CO} and the spin gap Δ_S defined as follows

$$\Delta_S(L) = E_0(L, N, S_z = 1) - E_0(L, N, S_z = 0) \tag{5.1}$$

where $E_0(L, N)$ is the ground state energy of the ladder system with $2L$ sites and N electrons, with $N = L$ for quarter filling. We calculate the ground state for different lengths L of the ladder:

L	16	24	36	48	64	80

So m^2_{CO} and Δ_S become functions of L and must be extrapolated to $L \to \infty$. Moreover, we investigate the ground state as a function of the nearest neighbor repulsion V, because it is very difficult to determine this parameter in first principles calculations[2], and because NaV_2O_5 is probably close to a quantum critical point of charge order [40], which we can find in that way.

In figure 5.1 we have calculated the charge order parameter m^2_{CO} defined by equation 2.11. We consider the system sizes mentioned above and vary the V-values in a range from 0 to 8. One sees that the value of the order parameter depends extremely on the length of the system. For $V \leq 2.35$ the order parameter m^2_{CO} becomes smaller, when the length L of the system increases. For $V \geq 2.50$ the order parameter m^2_{CO} shows a contrary behavior. There, the order parameter m^2_{CO} becomes larger if one uses larger systems. In addition we have observed an $1/L$-dependence of the order parameters m^2_{CO}, and as a result we have performed a finite size scaling by a linear fit in $1/L$ through the data points from the larger system sizes ($L \geq 36$). In alternative fits which include both $1/L$ and $1/L^2$ terms, the coefficient of the quadratic term is quite small in most cases (similar to [37]). The $1/L$-fits are illustrated in figure 5.1 and allow an estimation of the order parameter m^2_{CO} of the infinite system.

To illustrate the quantum phase transition to a charge ordered state we draw the order parameter m^2_{CO} as a function of the nearest neighbor repulsion V in figure 5.2. There the order parameter is plotted for the finite systems mentioned above. In addition we include the $L \to \infty$ extrapolated values, which we obtained from the finite size scaling. The error bars, which are indicated in the figure, are derived from the linear fit in $1/L$.

[2]See also subsection 2.3.2.

To investigate the critical behavior of the quantum phase transition we have tried to find a critical exponent α_{CO} of the charge order parameter m_{CO}^2 by fitting

$$m_{CO}^2 = \text{const} * \left(\frac{V - V_C}{V_C}\right)^{\alpha_{CO}} \tag{5.2}$$

through the relevant data points of the extrapolated order parameter in figure 5.2. We have obtained a quite good estimation for the critical V-value $V_C = 2.1 \pm 0.1$, but we have not been able to get an accurate value for the critical exponent α_{CO}, which is however definitely much larger than unity.

In figure 5.3 we compare our DMRG calculations with the results of reference [39]. There the authors have used a Lanczos method to determine the ground state. Due to this fact they have been restricted to very small systems (4 and 8 rungs) and the order parameters have been extremely size dependent. In addition they estimated the order parameter by an $1/L$-extrapolation. Certainly, this estimation is very imprecise and doesn't give the exact value of the order parameter in the thermodynamic limit. In contrast to this, our calculations constitute an enormous improvement as demonstrated in figures 5.2 and 5.3. We clearly see a quantum phase transition to a charge ordered state and can estimate an accurate critical value V_C.

We have also investigated the spin gap behavior of the system by calculating the spin gap Δ_S defined in equation 5.1. The results are strongly size-dependent like it is illustrated in figure 5.4. There, the spin gap is plotted for different V-value as a function of the inverse length $1/L$ of the system. We can observe that Δ_S becomes smaller for larger system sizes and also for larger V-values. A finite size scaling by a linear fit in $1/L$ ($L \geq 36$) provides us with the $L \to \infty$ extrapolated values of the spin gap. In figure 5.4 we also find spin gaps which become negative if we extrapolate $L \to \infty$. That should not be possible, because we must always obtain an $S_z = 0$-ground state in our systems. As a consequence we can estimate the minimum error of the extrapolated values for the spin gap by these negative values. Then the error of Δ_S in figure 5.4 is about 0.002 and it follows that the single ladder without electron-lattice interaction does not have a spin gap within this accuracy.

This result is not surprising. *M. Vojta et. al.* [37] have performed similar calculations with parameters less appropriate for NaV_2O_5 ($U/t_a = 4$, $V/t_a = 0$ or $V/t_a = 1$) and varied $\frac{t_a}{t_b}$ in the range from 0 to 2. Spin gaps could be only observed for $\frac{t_a}{t_b} \leq 0.8$, whereas for NaV_2O_5, $\frac{t_a}{t_b} \approx 2$. This agrees with results obtained by the derivation of an effective exchange Hamiltonian of a quarter-filled ladder in the strongly charge-ordered regime [37, 13]. In subsequent sections we will also investigate the spin gap in the low temperature phase when including electron-lattice coupling and/or in the case of coupled ladders.

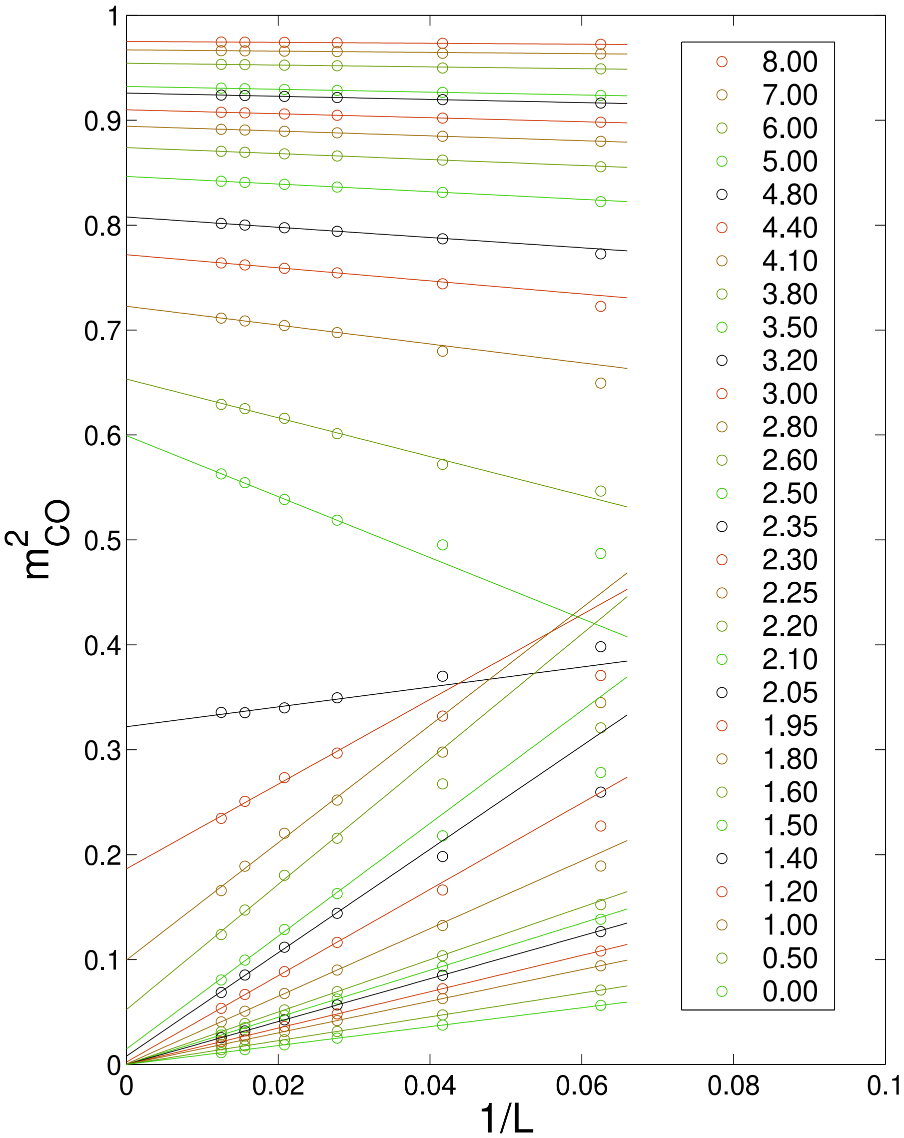

Figure 5.1: Finite size scaling for the charge order parameter m^2_{CO} versus the inverse length of a single ladder without electron-lattice interactions. A linear fit in $1/L$ through the data points $L \geq 36$ yields the value for the extrapolated order parameter ($L \to \infty$). The caption shows the values of the nearest neighbor repulsion V. The smallest V-values correspond to the smallest m^2_{CO}-values. One can obtain the V-value corresponding to the $1/L$-fit by counting the lines.

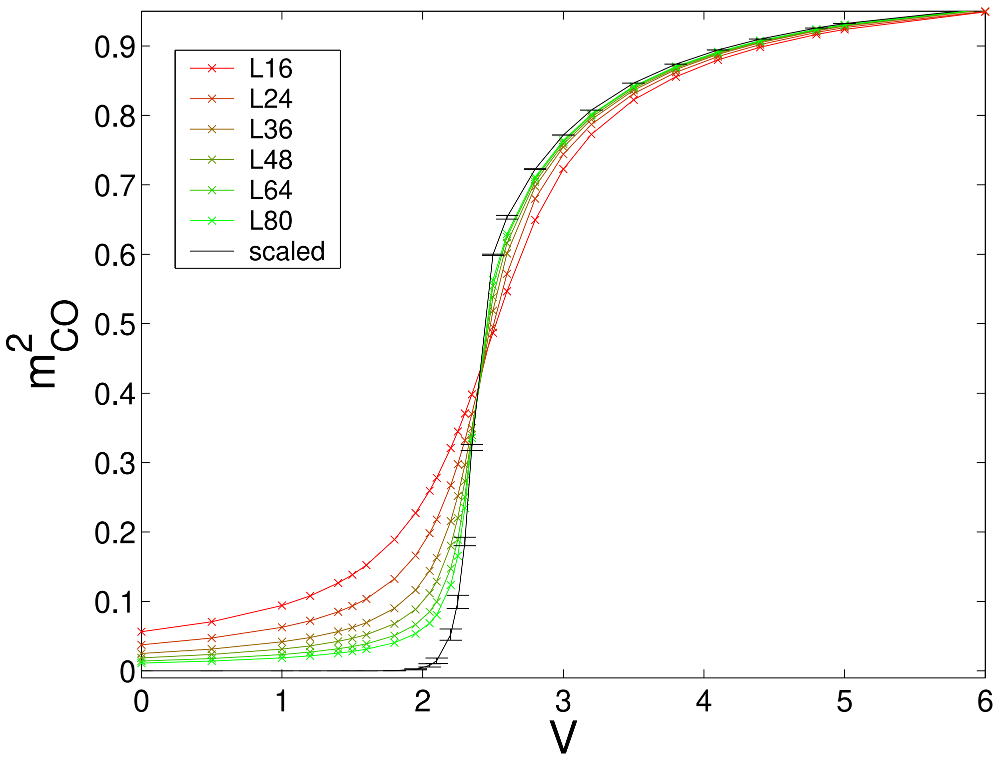

Figure 5.2: Order parameter m^2_{CO} as a function of the nearest neighbor repulsion V for a single ladder without electron-lattice interactions. The black line shows the $L \to \infty$ extrapolated values of the order parameter and their errors obtained from the fit.

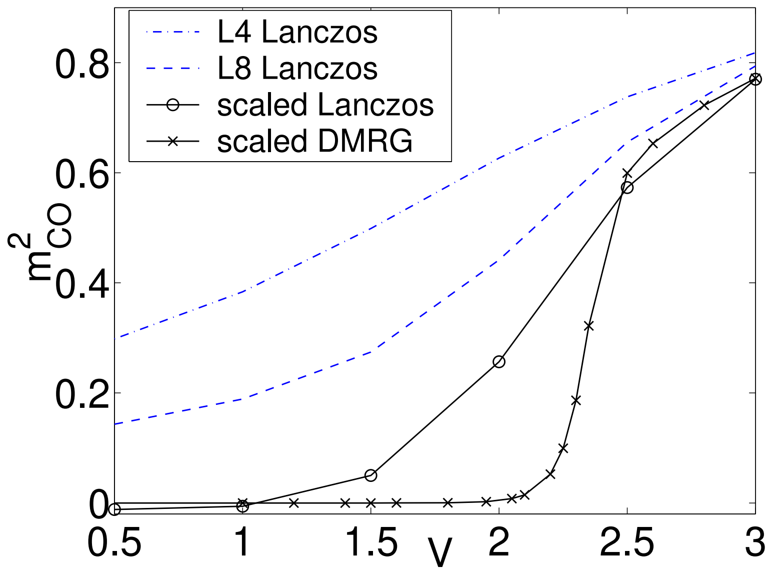

Figure 5.3: Lanczos calculations [39] compared to our DMRG calculations. The order parameter is drawn as a function of the V-value.

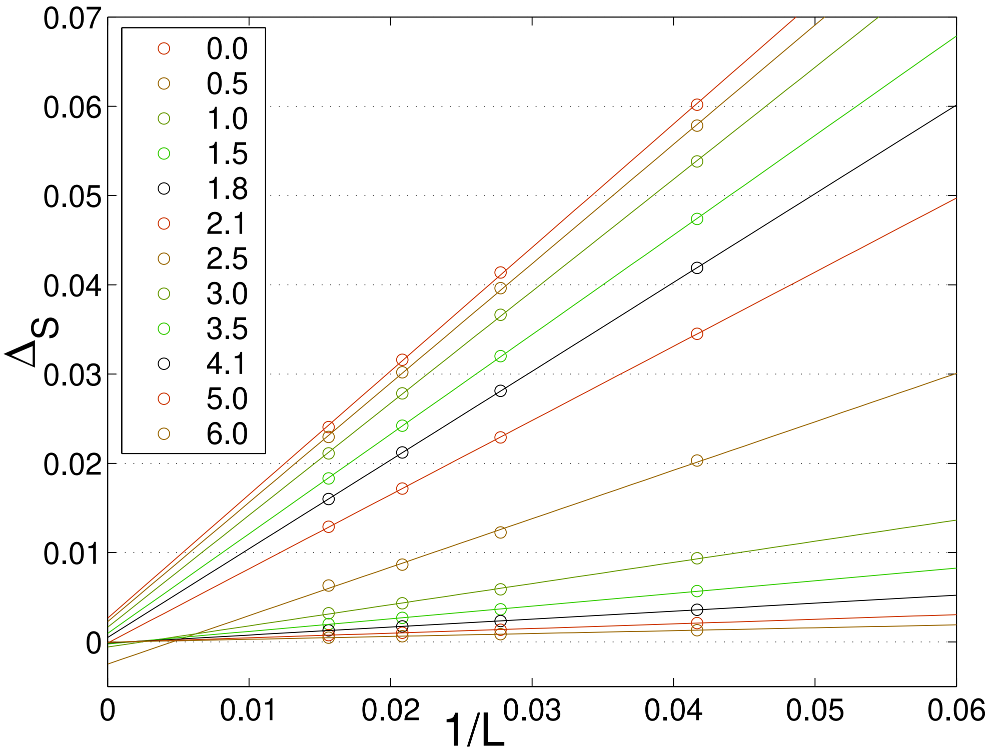

Figure 5.4: Finite size scaling for spin gap Δ_S versus the inverse length of a single ladder without electron-lattice interactions. A linear fit in $1/L$ through the data yields the value for the extrapolated spin gap ($L \to \infty$). The caption shows the values of the nearest neighbor repulsion V. The largest V-values correspond to the smallest spin gaps Δ_S. One can obtain the V-value corresponding the $1/L$-fit by counting the lines.

5.2 Ground state properties with electron-lattice interactions

Now we want to determine the charge order parameter m^2_{CO} and the spin gap Δ_S in a system which includes electron-lattice interactions and consists of a single ladder. Therefore we calculate the ground state of the Hamiltonian in equation 2.6. We assume zig-zag modulated distortions in the ladder because of the results of chapter 4. So we can reduce the number of independent distortions by equation 2.9 to one parameter z. In the present chapter we have calculated the ground state energy per site as a function of the parameter z by DMRG. The value z_{opt} which minimizes the total energy then corresponds to the "real" ground state of the system.

The optimal value of the zig-zag distortions z as a function of different nearest neighbor repulsions V is presented in figure 5.5. We have performed the calculations for ladders of length $L = 16, 24, 36, 48, 64$. The optimal z-values show only small finite size effects and as a consequence we only plot the values for $L = 64$. The z_{opt}-value has been calculated with an accuracy of 0.02. We can observe vanishing distortions for $V \leq 0.95$. For higher V-values ($V \geq 0.96$) we obtain zig-zag lattice distortions with values up to approximately 1.4.

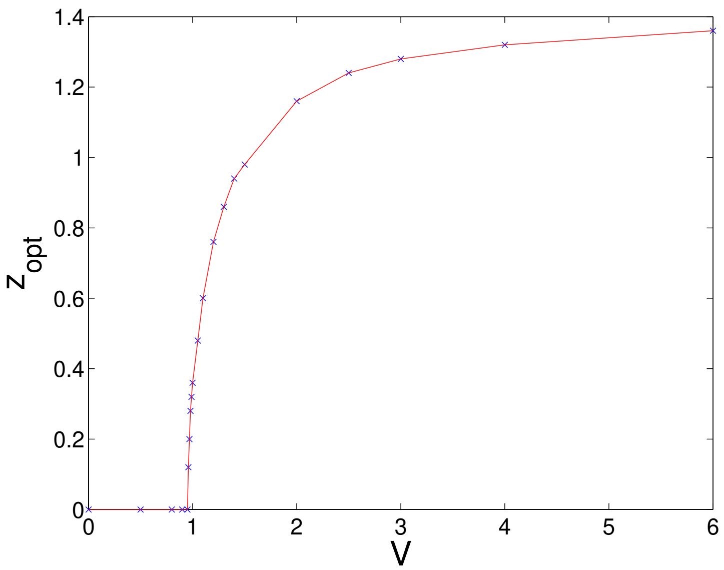

Figure 5.5: Optimal zig-zag distortions z_{opt} as a function of the nearest neighbor repulsion V in a system consisting of a single ladder of length $L = 64$. Accuracy: $\Delta z_{opt} = \pm 0.02$.

Certainly these finite distortions influence the charge order parameter for nearest neighbor repulsions $V > 0.95$. In figure 5.6 the order parameter is plotted as a function of the inverse length $1/L$ for different V-values. The order parameters aren't strongly size dependent (for $V \geq 1.00$) and a linear fit in $1/L$ seems to be appropriate to get $L \to \infty$ extrapolated values. As a result a finite size scaling is performed in figure 5.6. This yields scaled values of the order parameters, which are illustrated in figure 5.7 with the errors obtained by the fit. Moreover, the order parameters of the finite systems are depicted in figure 5.6. The order parameters increase rapidly at $V = 0.95$ due to the influence of the lattice distortions. An error analysis of the order parameter provides us with an accuracy of about 0.02.

The critical behavior has been investigated by fitting a critical exponent for the distortions α_D and for the charge order parameter α_{CO}. Our estimations yield $\alpha_D = 0.30...0.55$, $\alpha_{CO} = 0.50...0.80$ and a very accurate $V_C = 0.95 \pm 0.01$. In figure 5.8 we compare z_{opt} and m_{CO}. Here we have normalized the maximal distortion to the maximal value of the extrapolated order parameter m_{CO}. A comparison between the two functions shows that the critical exponent for the distortions α_D must be smaller than the α_{CO}-value and that charge order and zig-zag distortions concurrently occur at V_C.

The authors of reference [39] have treated these static distortions with a Lanczos method. Due to the small finite size effects for $V \geq 1.00$ their estimation of the charge order parameter m_{CO}^2 is much more accurate than for the system without lattice distortions. This is demonstrated in figure 5.9, which compares the DMRG calculations for large systems with the Lanczos results.

Last but not least we have investigated the behavior of the spin gap in this system. We have performed the same finite size scaling as in the previous section. The result is presented in figure 5.10 and shows vanishing spin gaps Δ_S for all V-values within the accuracy of our calculations, which is estimated as in the previous section. By considering the negative extrapolated values, we have concluded that the error must be at least 0.002.

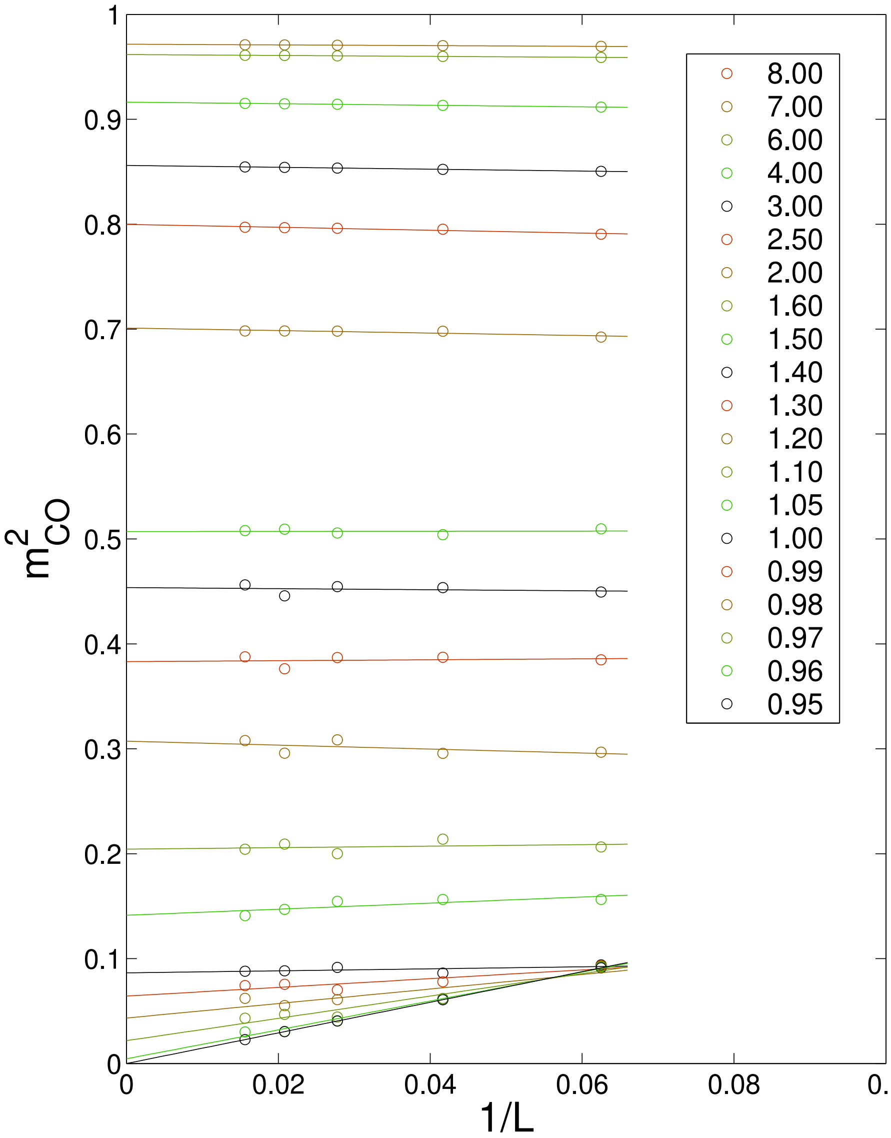

Figure 5.6: Finite size scaling for the charge order parameter m^2_{CO} versus the inverse length of a single ladder with static lattice distortions. A linear fit in $1/L$ through the data points $L \geq 36$ yields the value for the extrapolated order parameters ($L \to \infty$). The caption shows values of the nearest neighbor repulsion V. The largest V-values correspond to the smallest spin gaps Δ_S. One can obtain the V-value corresponding the $1/L$-fit by counting the lines.

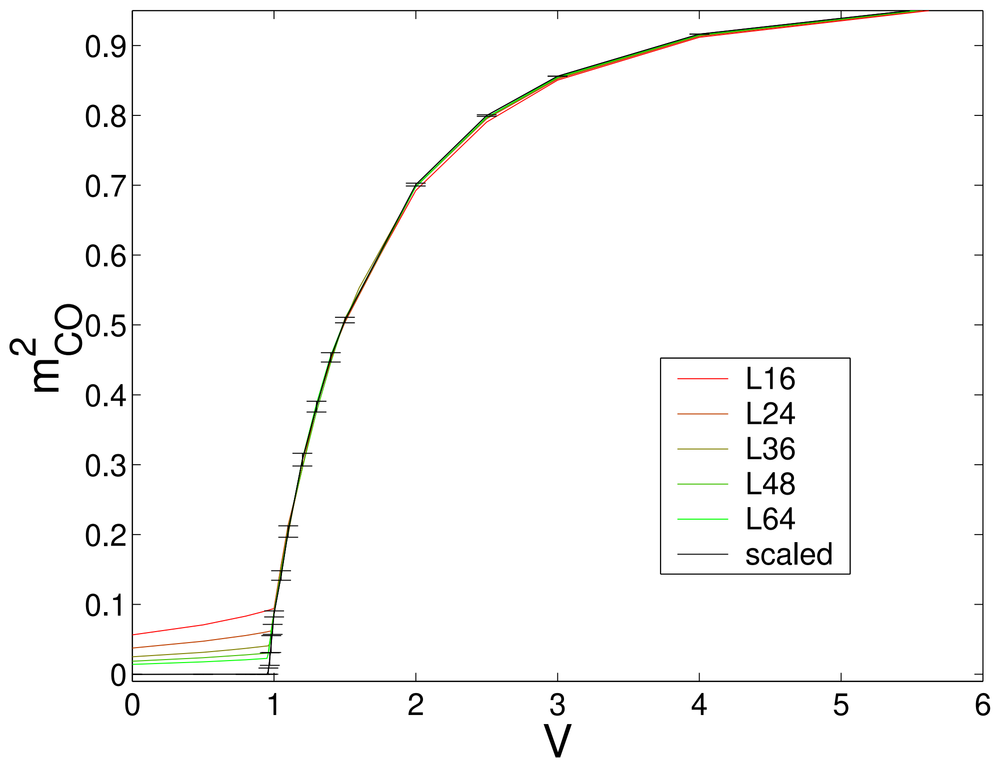

Figure 5.7: Order parameter m^2_{CO} as a function of the nearest neighbor repulsion V for a single ladder with static lattice distortion. The black line shows the $L \to \infty$ extrapolated values for the order parameter and their errors obtained from the fit.

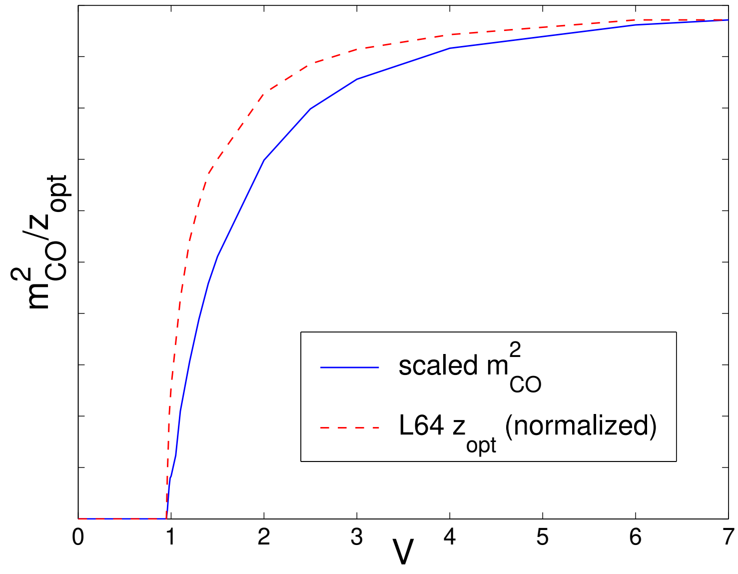

Figure 5.8: The critical behavior of the distortions z_{opt} compared with the critical behavior of the charge order parameter m^2_{CO}. The curves are normalized to the same maximum and illustrate that the critical exponent of the distortions α_D must be smaller than the α_{CO}-value.

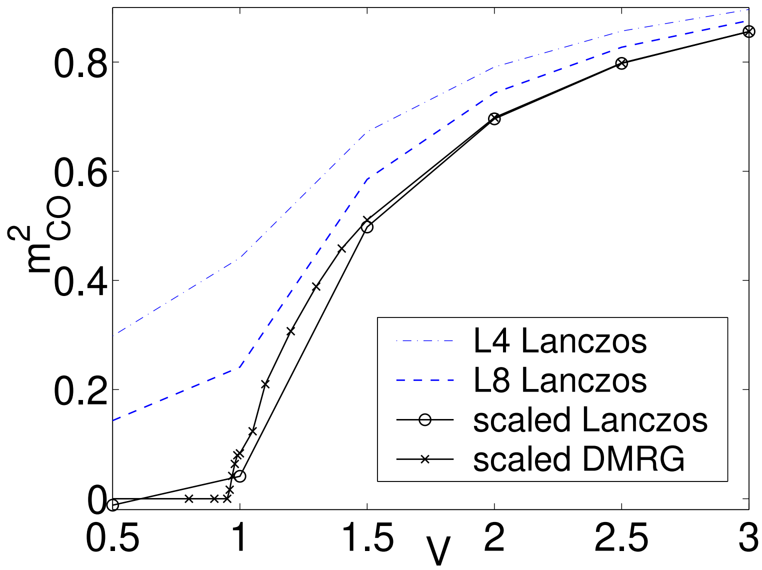

Figure 5.9: The Lanczos calculations compared with the DMRG calculations. The order parameter is plotted as a function of the V-value.

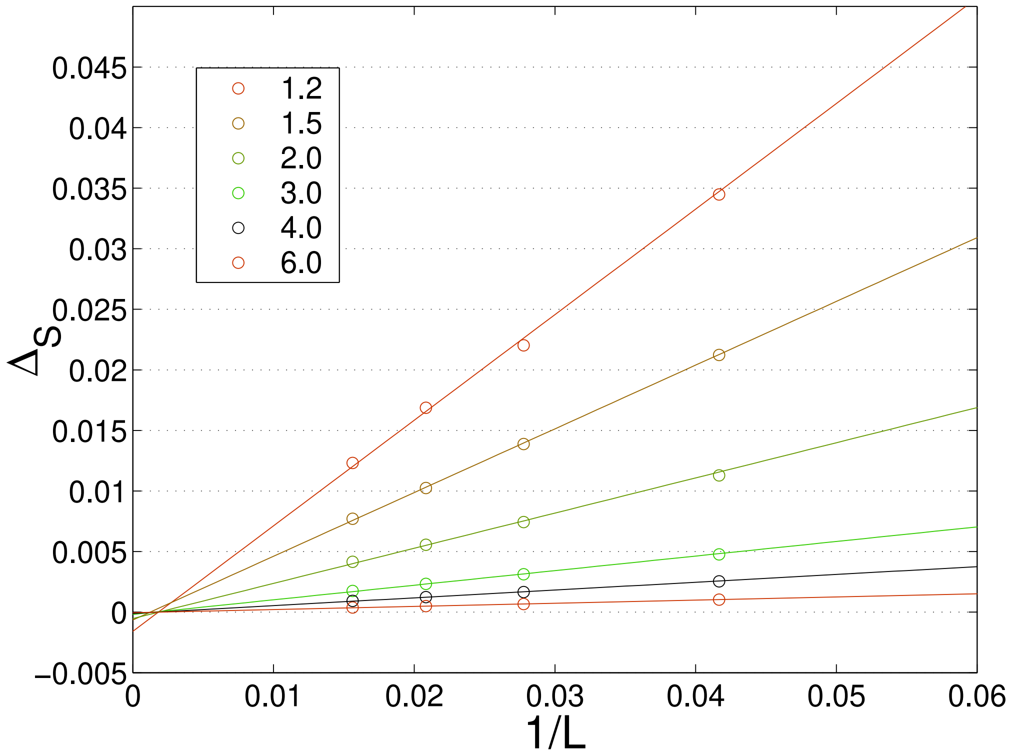

Figure 5.10: Finite size scaling for spin gap Δ_S versus the inverse length of a single ladder with static lattice distortions. A linear fit in $1/L$ through the data points from the larger system sizes ($L = 36, 48, 64$) yields the value for the extrapolated spin gap ($L \to \infty$). The caption shows the values of the nearest neighbor repulsion V. The largest V-values correspond to the smallest spin gaps Δ_S. One can obtain the V-value corresponding the $1/L$-fit by counting the lines.

5.3 Discussion of the results

The calculations in this chapter show a phase transition to a charge ordered state when the nearest neighbor repulsion V increases. The electron-lattice interactions cause a drastic decrease of the critical V-value V_C and a change of the critical exponent from much larger than unity to 0.5...0.8, i.e. a change in the universality class of this quantum phase transition. To demonstrate these facts the curves for the scaled value of the order parameter ($L \to \infty$) are plotted in figure 5.11. We estimated the critical V-values with $V_C = 2.1 \pm 0.1$ without electron-lattice coupling and $V_C = 0.95 \pm 0.01$ with coupling to static lattice distortions. Unfortunately the coupling of electrons to static lattice distortions cannot explain the opening of a spin gap in the low temperature phase of NaV_2O_5.

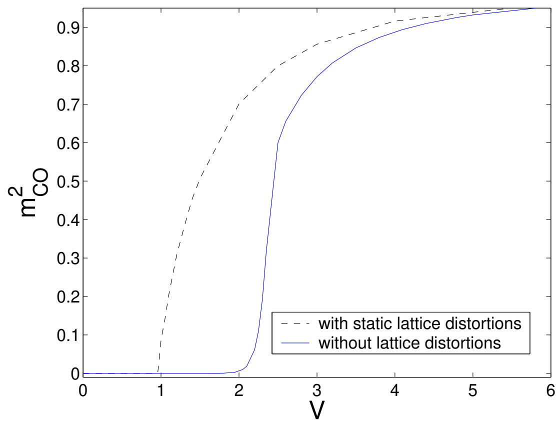

Figure 5.11: The scaled values for the order parameter m_{CO}^2 with (dashed line) and without (solid line) static lattice distortions in a single ladder system. Here the extrapolated values ($L \to \infty$) are presented.

In this thesis we only treat the coupling of the electrons to static lattice distortions and neglect dynamical phonons[3]. Reference [39] has shown that dynamical phonons have a strong influence on the charge order parameter in the vicinity of the phase transition. An analysis of the correlations of the dynamically induced distortions revealed that phonons indeed favor zig-zag lattice distortions. Moreover reference [39] has shown that using just static distortions overestimates the actual value of lattice distortion, but well away from the transition point this dynamical effect is very small and a description by static distortions gives already accurate results.

[3]The treatment of dynamical phonons is rather difficult. Details are mentioned in section 2.3.4.

Chapter 6

Influence of electron-lattice interactions on systems consisting of coupled ladders

Now we turn our attention to systems consisting of two coupled ladders, using Lanczos calculations as well as DMRG calculations. The model parameters and boundary conditions have been chosen as quoted in subsection 2.3.2 and 2.3.3. The Hamiltonian introduced in subsection 2.3.4 has been used to describe electron-lattice interactions.

The behavior of the charge order parameter is the main focus of this chapter. In the beginning we present Lanczos calculations for systems consisting of two coupled ladders with four rungs per ladder and with periodic boundary conditions in both directions. Afterwards, DMRG calculations for larger systems with open boundary conditions in b-direction are shown. We study the effects of the electron-lattice interactions and consider the differences between single and coupled ladder systems. The ground state of the Hamiltonian has always been calculated by taking into account the results of chapter 4, i.e. by using a zig-zag pattern of distortions. In addition, we restrict the calculations to equal zig-zag lattice distortions on both ladders. A possible generalization would be to allow different distortions on the two ladders.

6.1 Lanczos for coupled ladders

Some of the results obtained by the Lanczos calculations have already been presented in chapter 4. In this section we compare the charge order parameters m^2_{CO} of four different systems (Figure 6.1):

- one ladder system with 4 rungs *without electron-lattice interactions*
- one ladder system with 4 rungs *with electron-lattice interactions*
- a system of two coupled ladders with 4 rungs per ladder *without electron-lattice interactions*
- a system of two coupled ladders with 4 rungs per ladder *with electron-lattice interactions*

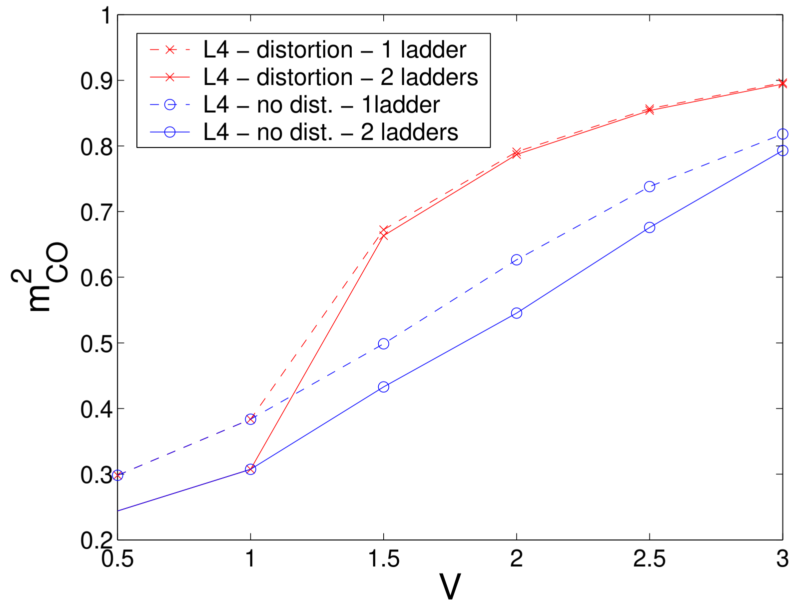

Figure 6.1: Charge order parameter m^2_{CO} as a function of the V-value for four different cases.

Figure 6.1 shows that the order parameter always decreases if we include the coupling to neighboring ladders. The decrease is much larger if we don't take into account the electron-lattice interactions. If we include electron-lattice interactions by static distortions, the order parameters of the single ladder and the two ladder system become very similar in size for V-values larger than 1.5. We see that the coupling to the next ladder isn't important for the order parameters in systems including the interactions between electrons and static lattice distortions. To investigate these issues for larger systems too, DMRG calculations have been performed.

6.2 DMRG for coupled ladders without electron-lattice interactions

In section 3.2 we mentioned that DMRG algorithms converge worse for two dimensional systems. So we can treat only smaller systems in this chapter than in the previous one, because two coupled ladders are "more 2-dimensional" than a single ladder.

First we have investigated the ground state of systems without electron-lattice interactions for systems of 8 and 12 rungs and plotted the charge order parameter m_{CO}^2 as a function of the V-value. We have performed a $1/L$ extrapolation to $1/L = 0$. Due to the fact that we use only two data points at a small system size, this procedure does not give the exact value of the order parameter, but provides a possibility to determine an approximate value of the interaction V at which the phase transition occurs as well as the $m_{CO}^2(V)$-dependence. The results are illustrated in figure 6.2 and are compared to single ladders of the same lengths in figure 6.3.

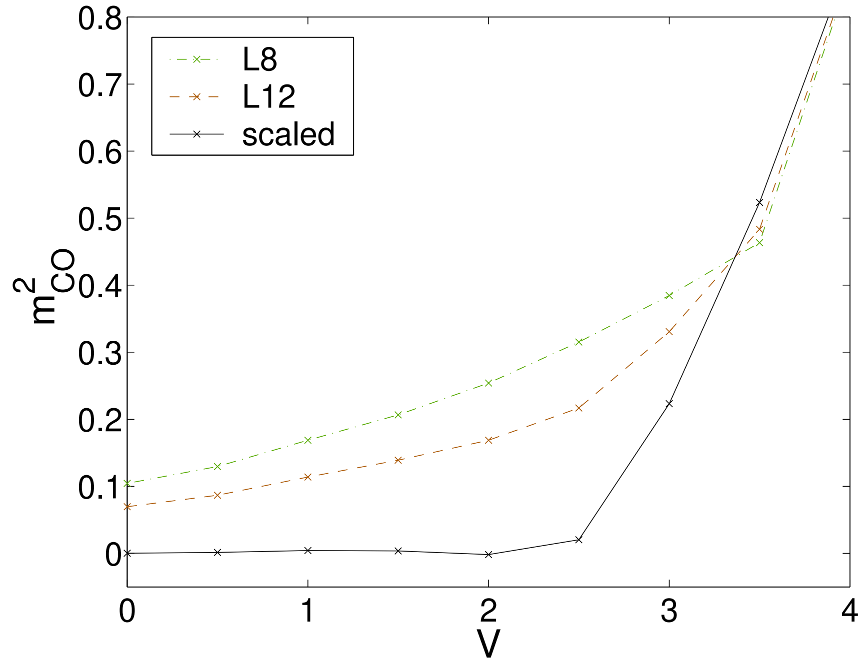

Figure 6.2: Charge order parameter m_{CO}^2 as a function of the V-value in coupled ladder systems of 8 and 12 rungs without electron-lattice interactions. A finite size scaling has been performed like in the previous chapter by an extrapolation in $1/L$.

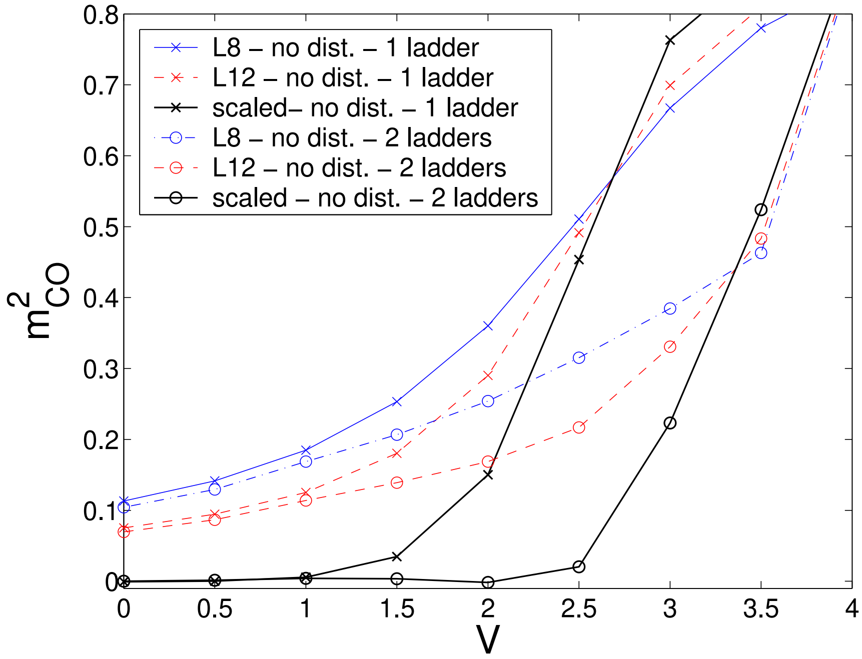

Figure 6.3: Charge order parameter m^2_{CO} as a function of the V-value in coupled ladder systems of 8 and 12 rungs without electron-lattice interactions compared to the results in single ladder systems of the same lengths. In addition an $1/L$ extrapolation to $1/L = 0$ has been performed for the present values (L8 and L12) for both cases.

Figure 6.2 and 6.3 confirm the Lanczos calculations. The order parameter is decreased by taking into account the coupling to the neighboring ladder. The drastic shift of the critical V-value is clearly illustrated in figure 6.3. We observe a shift of about unity of the extrapolated curve for coupled ladders in comparison to the extrapolated curve for a single ladder. Therefore the critical value V_C for charge ordering in the case of two coupled ladders can be assumed to be about unity larger than the value for a single ladder[1]. As a result our estimation for the critical value V_C in coupled ladders without lattice distortions yields about 3, considerably higher than in a single ladder.

[1]The critical value $V_C = 2.1 \pm 0.1$ in a single ladder without lattice distortions has been determined in section 5.1.

6.3 DMRG for coupled ladders with electron-lattice interactions

For systems including electron-lattice interactions we treat coupled ladders with 12 and 16 rungs[2]. Therefore we calculate the ground state of the Hamiltonian in equation 2.6. We assume zig-zag modulated distortions of the same size on both ladders. So the ground state energy is a function of only one parameter z. Then we can find the optimal distortion z_{opt} which minimizes the total energy in the same way as in section 5.2. Our calculations show that in the present case of coupled ladders with static lattice distortions the distortion z_{opt} is equal to the distortion z_{opt} of a single ladder with static lattice distortions. The charge order parameters mentioned in this section are calculated for the ground state with lowest energy, i.e. for zig-zag distortions z_{opt}.

Once more a finite size scaling for the charge order parameter has been performed (Figure 6.4). A comparison to single ladders of the same lengths is shown in figure 6.5. The calculations of this section show an interesting feature for systems including electron-lattice interactions. The order parameter isn't size dependent for V-values larger than unity (Figure 6.4) and doesn't depend on the coupling to the neighboring ladder (Figure 6.5).

Finally, the results of DMRG calculations on coupled ladders are summarized. Figure 6.6 shows the order parameter with and without coupling of the electrons to static lattice distortions. Moreover, the extrapolated value for the single ladder system without distortions is illustrated. The order parameter of a single ladder with static lattice distortions is not shown, because it agrees with the order parameter of coupled ladders with static lattice distortions. From these results we conclude that the coupling of the electrons to static lattice distortions stabilizes the system. The order parameter becomes less size dependent (Figure 6.4) and is not influenced by the coupling to the neighboring ladder (Figure 6.5). For systems without lattice distortions we observe a contrary behavior. The order parameter is strongly influenced by the size of the system and by the coupling to the neighboring ladder.

We have also investigated the spin gap behavior in coupled ladders, but we have not been able to determine an accurate extrapolated value of Δ_S. Due to the restriction to smaller systems in coupled ladders the finite size scaling

[2] Larger system sizes than in section 6.2 are possible because static zig-zag lattice distortions enhance the convergence of the DMRG program.

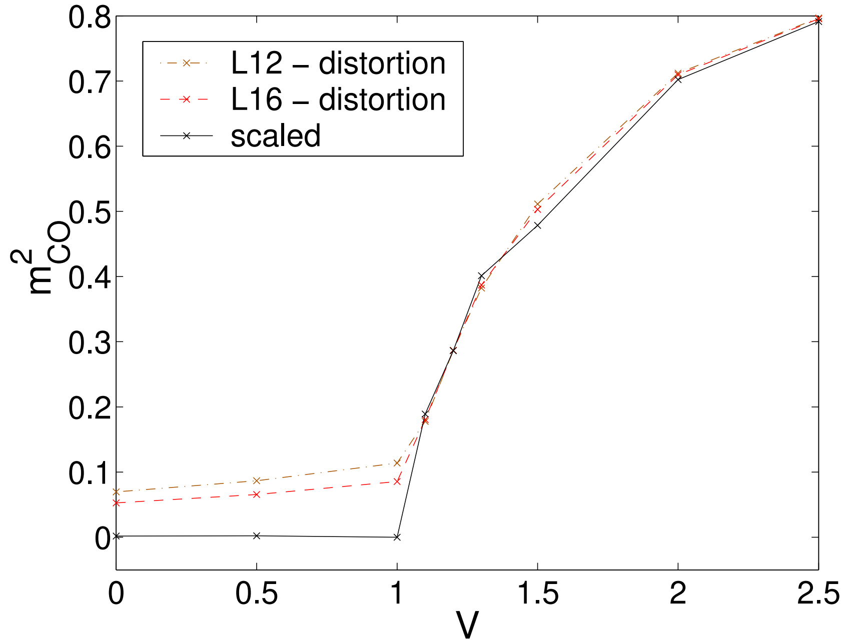

Figure 6.4: Charge order parameter m^2_{CO} as a function of the V-value in coupled ladder systems of 12 and 16 rungs with static lattice distortions. In addition a finite size scaling has been performed like in the previous section.

has been too imprecise. As a consequence we could not answer the question, whether the coupling to the neighboring ladder opens a spin gap.

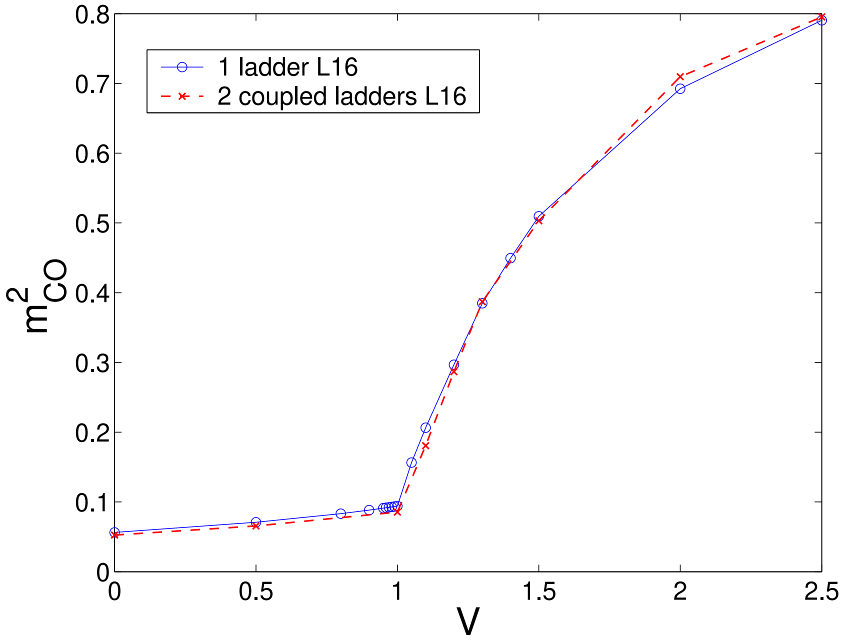

Figure 6.5: Charge order parameter m_{CO}^2 as a function of the V-value in a coupled ladder system of 16 rungs with static lattice distortions compared to the result in a single ladder system of the same length.

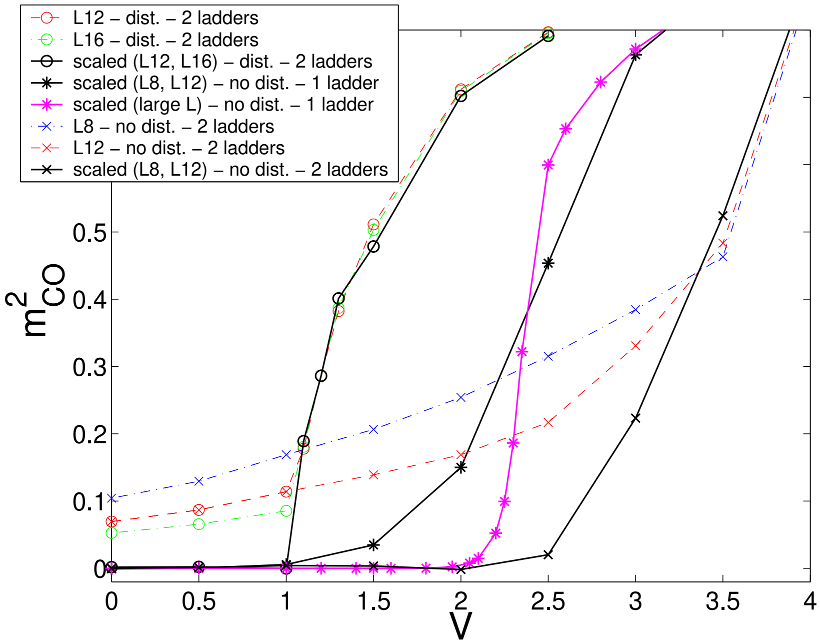

Figure 6.6: Charge order parameter m^2_{CO} as a function of the V-value in coupled ladder systems with and without static lattice distortions. In addition two extrapolated order parameters of a single ladder without lattice distortions are depicted. The first extrapolation only includes the systems with 8 and 12 rungs, the second extrapolation includes large systems up to 80 rungs. With distortions, single and coupled ladders agree.

Chapter 7

Conclusions

The goal of this work has been to investigate the charge order process in the compound α'-NaV_2O_5 in the low temperature phase including coupling to lattice distortions. For that purpose we have considered an extended Hubbard model together with a Holstein coupling to the lattice, using parameters from first-principles calculations (Reference [9]).

To investigate the Hubbard-Holstein model we have restricted ourselves to classical static lattice distortions. These distortions have at first been treated as being independent for each lattice site. We have performed a Monte-Carlo procedure combined with a Lanzcos diagonalization to find the configuration of distortions which minimizes the ground state energy. Our calculations clearly indicate a pure zig-zag pattern of lattice distortions for nearest-neighbor repulsion V larger than about unity. For smaller V-values we have always found vanishing distortions on all sites. We have performed these calculations also for coupled ladder systems, where we have obtained similar results (zig-zag distortions of the same order of magnitude on each ladder).

Due to these results we have then restricted our calculations to zig-zag lattice distortions, when investigating the influence of the lattice distortions on the charge order parameter. We have applied DMRG to determine the charge order parameter as a function of the nearest-neighbor repulsion V. After performing a finite size scaling analysis, we have been able to estimate the critical V-value $V_C = 2.1 \pm 0.1$ for the transition to a charge ordered state for a single ladder system without any coupling to the lattice, with a critical exponent of much larger than unity. When electron-lattice interactions are included, charge order occurs concurrently with finite static lattice distortions at a strongly reduced critical V-value $V_C = 0.95 \pm 0.01$, and a change in the universality class of the corresponding quantum phase transition takes place, with a critical exponent of 0.5...0.8. In addition the finite size effects of the charge order parameter become very small above the critical value V_C in systems with static lattice distortions.

Modifying our model by including the coupling to the next ladder has yielded a transition to charge order at a considerably larger Coulomb repulsion in the systems without electron-lattice coupling. On the other hand the order parameter is not influenced by the coupling to the neighboring ladder in systems with static lattice distortions. Our results for the charge order parameter are summarized in figure 6.6.

Last but not least we have considered the spin gap Δ_S of the single ladder system. For that purpose we have performed DMRG calculations which have shown a vanishing spin gap for the system without coupling as well as for the system with electron-lattice coupling for all V-values. Thus coupling to static lattice distortions does not cause a spin gap in single ladder systems with parameters appropriate for NaV_2O_5.

Our calculations show that the coupling of the electrons to lattice distortions considerably influence the charge order process in NaV_2O_5. The coupling to neighboring ladders doesn't seem to be important for charge ordering in systems with static lattice distortions. Dynamical quantum phonons may change this behavior. Moreover, the opening of the spin gap in the low temperature phase cannot be explained by the coupling to static lattice distortions. This feature may be described by including further hopping processes (e.g. diagonal hopping), the coupling in c-direction and/or the treatment of dynamical phonons.

Appendix A

Details on DMRG calculations

We have performed our DMRG calculations with a DMRG program developed by Reinhard M. Noack written in the computer language C++. The convergence of our DMRG calculations has strongly depended on the system sizes and the model parameters which we have used. As a consequence it has always taken some time to find the appropriate DMRG settings. These settings and all occured problems are summarized in this appendix.

A.1 Iteration steps

For all systems we have used the Davidson algorithm to diagonalize the superblock (See subsection 3.2.3). The number of iteration steps and the settings at each step are quoted for different systems in the tables A.1 and A.2. The notations in the tables are as follows:

- maxstates: Maximum states of the reduced basis
- davideps: Exit condition of the Davidson algorithm
- maxiter: Maximum iterations of the Davidson algorithm
- david dim: Dimensions used in the Davidson algorithm

The convergence of systems with lattice distortions has been better than for systems without lattice distortions. Nevertheless we have used the same DMRG input settings for both cases. For coupled ladders convergence has

step	maxstates	davideps	maxiter	david dim
1	100	1e-3	5	6
2	200	1e-4	5	6
3	300	1e-4	5	5
4	450	1e-4	5	5
5	600	1e-5	5	5
6	800	1e-5	5	5
7	800	1e-4	5	5

Table A.1: DMRG settings for single ladders with 64 rungs.

step	maxstates	davideps	maxiter	david dim
1	200	1e-4	5	6
2	300	1e-4	5	5
3	450	1e-4	5	5
4	500	1e-5	7	7
5	600	1e-5	7	7
6	600	1e-5	7	7
7	800	1e-5	7	7
8	800	1e-5	7	7
9	800	1e-5	7	7

Table A.2: DMRG settings for coupled ladders with 16 rungs.

been worse than for a single ladder. Moreover, CPU time has increased from about 6 hours (64 rungs in a single ladder) to about 2 days (16 rungs in coupled ladders). The convergence has also become worse for large nearest neighbor repulsions ($V > V_C$).

We have checked out several DMRG settings to get better convergence and to treat larger systems. Our experience show that double or triple the number of iterations through the lattice does not automatically yield much better results as the iteration settings mentioned in the tables. As a result it is difficult to reach better convergence if the settings mentioned in the tables are not sufficient. Nevertheless it can be usefull to append some iterations through the lattice to consider if the results change a lot.

An other possibility to improve convergence is to increase the number of states of the reduced density matrix (*maxstates*). That would advance the result in all probability, but is connected with an increase of main memory and CPU time. As a consequence we have been restricted to about 1000 states of the reduced density matrix.

We also performed runs with different settings for the parameters *davideps, maxiter, david dim*, which influence the diagonalization of the superblock by the Davidson algorithm. Our attempts weren't able to improve convergence and we observed that DMRG convergence was only marginally influenced by the variation these parameters.

Last but not least we would like to annotate that it is difficult to determine if the calculations are converged and if they yield to the ground state of the system. It can happen that increasing the number of states and iterations do not change the results, but that is no guaranty that we have converged to the ground state. It is also possible that the algorithm converged to a excited state. As a consequence DMRG results must be always carefully considered and checked if their behavior has a physical motivation.

A.2 Warm up

The DMRG input contains a couple of settings for the warm up phase. They constitute a possibility to build up the system in a certain way in the warm up iteration, which is equal to infinite system algorithm. Particularly for systems without reflection symmetrie **rsym =0** these settings are important. A detailed explanation of them is given in the file *infinite.txt* of the DMRG program.

A.3 Reflecton symmetrie (rsym)

Convergence has become better and CPU time has been saved if we have used reflection symmetry(**rsym = 1**) for single ladders. We have also used reflection symmetry for coupled ladders, but that seems to frustrate the system in some way during the iteration process. Due to this fact we suggest to deactivate reflection symmetry(**rsym = 0**) for coupled ladders.

A.4 Batch system and memory (savetodisk)

We have performed your calculation at Unix/Linux computers of Institute of Theoretical Physics of the TU Graz. We managed most of our DMRG jobs by the batch system Condor (*http://www.cs.wisc.edu/condor/*) and used the special compile command *condor_compile*.

An other important feature of the DMRG program is the possibility to decide either to store the different system blocks and and operators in the main memory (**savetodisk = 0**) or to store them on the hard disk space (**savetodisk = 1**). For Condor jobs it is not possible in an easy way to choose (**savetodisk = 1**), because jobs can be repartioned to an other computer during their execution. So the data must be stored on a non local hard disk space, which enormously stress the local network due to the fact that a large amount of data must be transfered from the local computer to the non local hard disk space. Consequently we do not recommend to use **savetodisk = 1** for Condor Jobs.

Nevertheless it is necessary in some cases to choose **savetodisk = 1**. If system size and the number of states of the reduced basis are choosen large (e.g. 2 ladders with 24 rungs and 900 states) the amount of data can require a main memory of more than one GByte. If such a main memory is not available, we are forced to store the data on the hard disk and to manage our jobs without the batch system Condor.

A.5 Output file

The DMRG program create an output file, which includes a large amount of data. The size of the output file is determined by the setting of the DMRG input parameter **print level**. A print level of 0 creates a smaller output file, which include only few main informations. A print level of 1 includes e.g. information about discarded weight and CPU time at the current iteration step. These information can be helpful to control convergence. To analyse the discarded weights we used a perl script from R. Noack. In that way we got information about convergence. So we recommend to choose the print level at least to 1 and not smaller. Higher print levels include e.g. information about all operators of which the Hamiltonian is constructed.

The output file includes all informations about correlation functions or local operators, which were set in the DMRG input. In this context we recommend to display all maybe interesting operators, because one has to repeat the whole calculation to get operators, which are not quoted in the inputfile. To pick the informations form the output file we used perl scripts. Afterwards the output of these perl scripts were analysed and illustrated by Matlab scripts.

A.6 Extend the program

The DMRG program allows in an easy way to construct new lattices and operators. This requires only some extensions in the C++ file *lattice.cc*. We used this feature to include coupled ladders systems in the program. In the same one can construct new operators for measurements.

A.7 Calculation of the order parameter

We have determined the charge order parameter by averaging the density-density correlations $\langle \hat{n}_{xy}\hat{n}_{x'y'}\rangle$ with $x = \frac{L}{2}-1, \frac{L}{2}, \frac{L}{2}+1, \frac{L}{2}+2$; $x' = 1...L$ and $y, y' = 1, 2\,(, 3, 4)$. Moreover, it is important to determine the order parameter by

$$m_{CO}^2 = \frac{1}{N^2\langle n\rangle^2}\sum_{ij} e^{i(\pi,\pi)(\mathbf{R}_i-\mathbf{R}_j)}\left(\langle n_i n_j\rangle - \langle n\rangle^2\right)$$

and not by

$$m_{CO}^2 = \frac{1}{N^2\langle n\rangle^2}\sum_{ij} e^{i(\pi,\pi)(\mathbf{R}_i-\mathbf{R}_j)}\left(\langle n_i n_j\rangle - \langle n_i\rangle\langle n_j\rangle\right) ,$$

because the DMRG routine returns an asymmetric ground state for large systems, when $V > V_C$. In this ground state the zig-zag charge ordering is also visible in the local densities. Then DMRG returns only one of the two zig-zag charge ordered configurations of the ground state and an order parameter, which includes local densities $\langle n_i\rangle$ would yield a wrong result.

A.8 Influence of open boundary conditions

In this thesis I have always used open boundary conditions in b-direction, due to better DMRG convergence. As a result the ladders are aborted and show boundary effects like oscillations in the local densities (Friedel oscillations). For one ladder and a large number of rungs these oscillations have only a small influence on the finite system.

For two coupled ladders the situation becomes more difficult. Due to worse convergence of more 2-dimensional systems we can only treat smaller systems. So the boundary regions cover a large part of the whole system and consequently they considerably influence the system. The oscillations of the local densities at the boundaries are illustrated in figure A.1 for a two ladder system of 8 rungs and at a V-value of 2.0. The system do not include the coupling to lattice distortions.

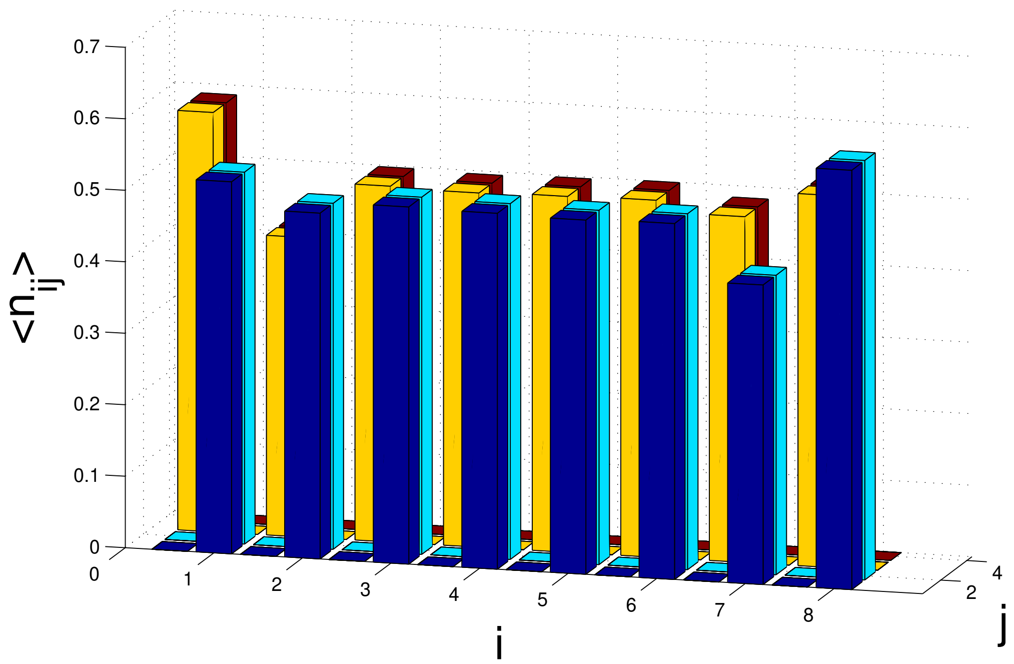

Figure A.1: Oscillations of the local density in a two ladder system of 8 rungs at a V-value of 2.0. In an infinite system the local density should be everywhere equal to 0.5. The figure clearly shows the deviation from this value in the boundary region.

To reduce these boundary effects we tried to modify the Coulomb repulsions at the rungs at boundary. For that purpose we considered a totally disordered system and a totally ordered system. Due to the periodic boundary conditions we had to distinct beween three different rungs of the system. The are illustrated in figure A.2. Now we modifyied the system so that the energie became equal for the total ordered and disordered systems. For that purpose we considered the energies per rung with the original nearest neighbor repulsion. That yields to the following energies per rung:

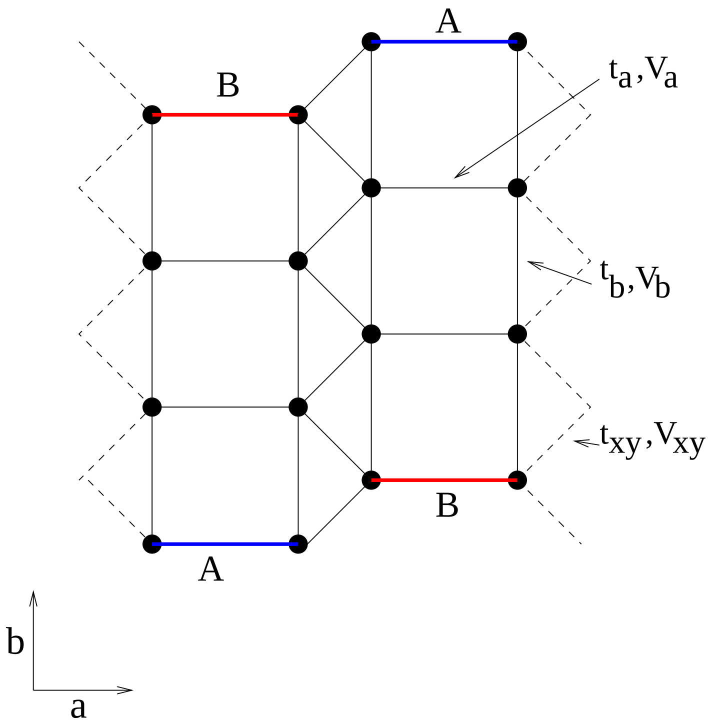

Figure A.2: A system with open boundary conditions, which includes three different types of rungs - the rungs in the bulk (black), the rungs at boundary A (blue) and the rungs at boundary B (red).

- in the bulk:
  - disordered system: $\frac{1}{4} * (V_a + 2V_b + 2V_{xy})$
  - ordered system: $\frac{V_{xy}}{2}$
- at boundary A:
  - disordered system: $\frac{1}{4} * (V_a + V_b + V_{xy})$
  - ordered system: $\frac{V_{xy}}{2}$
- at boundary B:
  - disordered system: $\frac{1}{4} * (V_a + V_b + 2V_{xy})$
  - ordered system: $\frac{V_{xy}}{2}$

To get equal energies for rungs at the boundary and in the bulk for the totally ordered as well as for the totally disordered system we had to modify the repulsion V_a at the boundary as follows:

- at boundary A: $\widetilde{V}_a = V_a + V_b + V_{xy}$
- at boundary B: $\widetilde{V}_a = V_a + V_b$

We checked this modification and yielded local densities which did not show any boundary effects. This constituted an improvement in comparison to the orignal system where we saw oscillations of the local density at the boundary. Unfortunately the boundary effects on the local spin S_z, which interfere the calculation of a spin gap, weren't not suppressed by this modification. Details on the boundary effects on the local spin S_z are mentioned in section A.10.

A.9 Bad convergence for coupled ladders

When we considered coupled ladders we were faced with a couple of convergence problems. They become visible if we consider the m^2_{CO} of a coupled ladder system with V-values in the range from 0 to 6 at different system sizes (Figure A.4). The regions, which show a strange behaviour are marked by arrows.

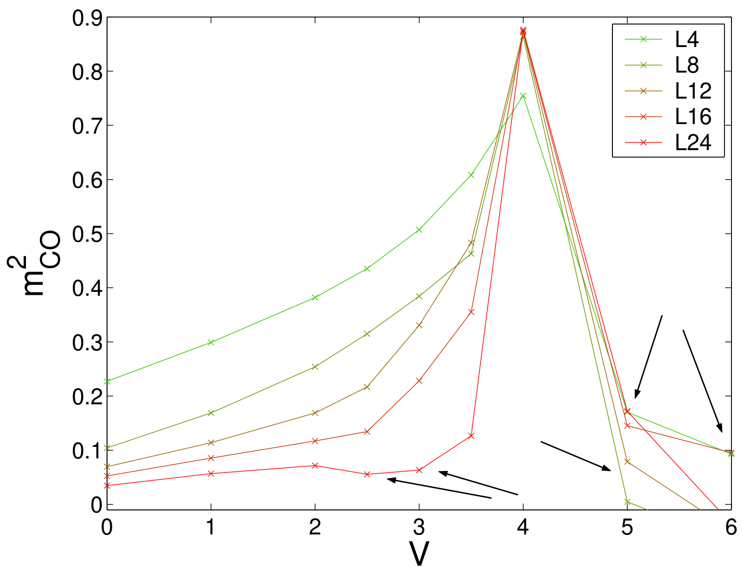

Figure A.3: Charge order parameter m^2_{CO} as a function of different V-values in a coupled ladder system without distortions. The regions in which the order parameter shows a strange behaviour are marked by arrows.

We tried to treat coupled ladder system up to 36 rungs per ladder but we detected that there was something going wrong. Particularly the charge order parameter m^2_{CO} indicates total disorder for V-values higher than 4 for all system sizes. This behaviour is not very discontenting, because it do not have a physical motivation. Our considerations conclude that their are two reasons for these behaviour.

Firstly the boundary conditions seems to influence the results dramatically. This assumption follows from Lanzcos calculation for a small system (2 coupled ladders with 4 rungs), which show the equal behaviour of the order parameter for open boundary conditions than the DMRG calculations. For periodic boundary conditions the order parameter do not decrease like it is illustrated in figure A.4.

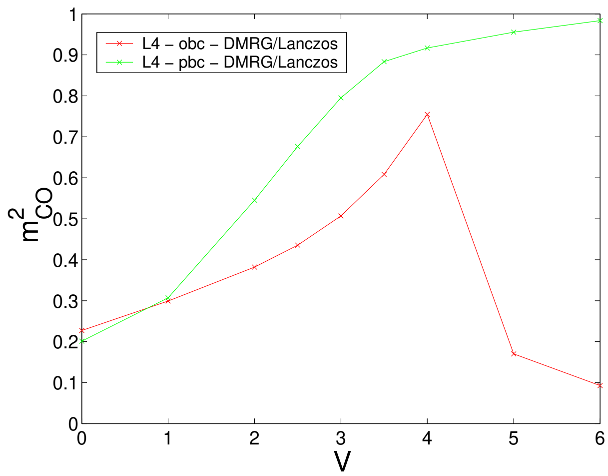

Figure A.4: Charge order parameter m^2_{CO} as a function of different V-values in a coupled ladder system without distortions and for rungs. DMRG calculations and Lanczos yield to the same result, when the same boundary conditions are used. (obc - open boundary conditions, pbc - periodic boundary conditions)

Secondly the results stay small for large system sizes. Consequently we assume that in this region the convergence become bad for large systems, because otherwise the order parameter would increase compared to smaller systems. This situation agrees with the generally observations that the convergence decrease with increasing V-value.

But also for smaller V-values we detected that the systems didn't converge to its ground states like it is also illustrated in figure A.4 and figure A.5. For the system consisting of 24 rungs the order parameter begin to decrease for V-values of about 2. So we considered the density-density correlations and found an unusual behavior like it is depicted in figure A.6. If we consider the first ladder (dark and light blue bars) we observe a local zig-zag charge order. The density-density correlations alternate and become about 0.25 after few rungs. In figure A.6 correlations on the first chain of the first ladder, which are larger than 0.25 are indicated by a " + ", the smaller ones are indicated by a " − ". At the points marked by arrows " + " and " − " do not alternate anymore.

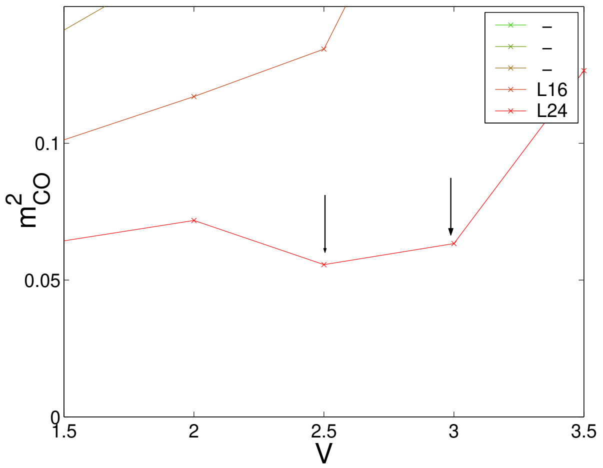

Figure A.5: Charge order parameter m_{CO}^2 as a function of different V-values in a coupled ladder system without distortions. The region in which the order parameter shows a strange behaviour are marked by arrows. This figure is a part of figure A.4, which is drawn to a larger scale.

We cannot explain this behavior and assume that it is caused by a bad convergence of the DMRG program. Due to the fact that more iteration through the lattice (These calculations took more than 1 week CPU) do not better the result we restrict ourselves to smaller systems up to 12 rungs (16 rungs for systems with distortions), where this strange behavior disappears. Moreover we do not regard V-values larger than 4 due the above mentioned reason. That do not constitute a strong restriction, because V-values larger than 4 are not realistic for NaV_2O_5.

A.10 Spin gap

Last but not least we tried to calculate spin gaps for coupled ladders in the same way than for single ladders. To due huge boundary effects we weren't able to calculate the spin gap in an easy way. In the region, which could

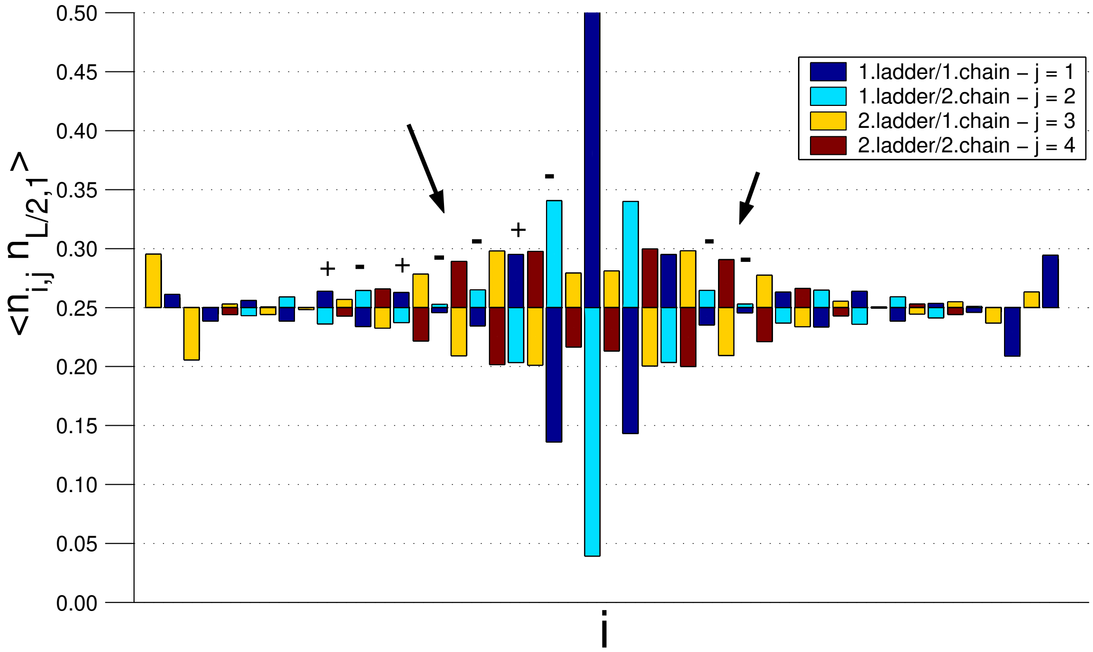

Figure A.6: The density-density correlations $\langle n_{ij} n_{\frac{L}{2}1} \rangle$ in a coupled ladder system with 24 rungs and a V-value 2.0.

be relevant for the spin gap in coupled ladder systems without distortions ($V > 3$, charge ordered states) the spin is located in the boundary area (probably due to bad convergence) like it is illustrated in figure A.7. So the energie gap beween the spin $S_z = 0$ and $S_z = 1$ ground state is strongly influenced by the boundary and consequently finite size scaling yields to wrong results.

To solve this problem we proceeded in an similar way than in section A.8, where we modified the nearest neighbor repulsion at the boundary. Here we changed the hopping terms at the boundary which mainly influence the spins. We checked several different hopping terms, but weren't very successful. For high V-values (about 3 an higher) the problem does not disappear.

For system with distortion we were able to give estimations for the spin gap for V-values smaller than 2, but the results are not mentionend in this work.

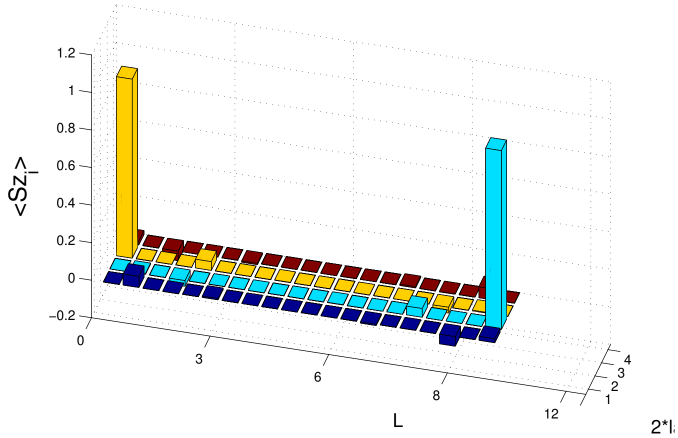

Figure A.7: Total spin S_z on the site in a system of 2 coupled ladder without distortions and 10 rungs at a V-value of 4.

Acknowledgments

I would like to thank all members of the many particle group at the ITP Graz, especially my supervisor Prof. Hans Gerd Evertz, and DI Markus Aichhorn for his help with the Lanczos program. In addition it is a pleasure to thank Prof. Reinhard Noack for using his DMRG program and for his support. Special thanks go to my sister Christiane Edegger for her help to eliminate misspellings in this thesis. And last but not least I would like to thank my parents, Karl and Elisabeth Edegger, for their encouragement all over the last few years.

Bibliography

[1] D. R. Hartree, Proc. Cambridge Philos. Soc. **24**, 89 (1928).

[2] V. Fock, Z. Phys. **61**, 126 (1930).

[3] P. Hohenberg and W. Kohn, Phys. Rev. **136**, B 864 (1964).

[4] W. Kohn and L. J. Sham, Phys. Rev **140**, A 1133 (1965).

[5] G. Bednorz and K. A. Müller, Z. Phys. B. **64**, 189 (1986).

[6] M. N. Baibich *et al.*, Phys. Rev. Lett. **61**, 2472 (1988).

[7] G. Binasch *et al.*, Phys. Rev. B **39**, 4828 (1989).

[8] C. H. Chen and S.-W. Cheong, Phys. Rev. Lett **76**, 4042 (1996).

[9] J. Spitaler, E. Ya. Sherman, C. Ambrosch-Draxl and H. G. Evertz (2004), cond-mat/0404076.

[10] W. von der Linden, *Many particle problems*, lecture notes, TU Graz, 2003.

[11] R. Blankenbecler, D. J. Scalapino, and R. L. Sugar, Phys. Rev D **24**, 2278 (1981).

[12] I. Peschel, X. Wang, M. Kaulke, and K. Hallberg, *Density-Matrix Renormalization* (1999), Springer-Verlag.

[13] A. Hübsch, *Charge excitations in low-dimensional transition metal compounds*, Ph.D. thesis, Dresden (2001).

[14] M. Aichhorn, *Charge ordering and Optical Conductivity of NaV2O5*, Master's thesis, TU Graz (2002).

[15] A. Carpy and J. Galy, Acta Crystallogr., Sect. B: Struct. Crystallogr. Cryst. Chem. **31**, 1481 (1975).

[16] J. Lüdecke *et al.*, Phys. Rev. Lett. **82**, 3663 (1999).

[17] H. Smolinsk *et al.*, Phys. Rev. Lett. **80**, 5164 (1998).

[18] H. G. von Schnering *et al.*, Z. Kristallogr. **213**, 246 (1998).

[19] A. Meetsma *et al.*, Acta Crystallogr., Sect. C: Cryst. Struct. Commun. **54**, 1558 (1998).

[20] E. J. W. Verwey, Nature (London) **144**, 327 (1939).

[21] T. Ohama *et al.*, Phys. Rev. B **59**, 3299 (1999).

[22] T. Yosihama *et al.*, J. Phys. Soc. Jpn. **67**, 744 (1998).

[23] Y. Fagot-Revurat, M. Mehring, and R. K. Kremer, Phys. Rev. Lett. **84**, 4136 (2000).

[24] M. Isobe and Y. Ueda, J. Phys. Soc. Jpn. **65**, 1178 (1996).

[25] D. Powell *et al.*, Phys. Rev. B **58**, R2937 (1998).

[26] P. Fertey *et al.*, Phys. Rev. B **57**, 13698 (1998).

[27] S. Ravy, J. Jegoudez, and A. Revcolevschi, Phys. Rev. B **59**, R681 (1999).

[28] H. Nakao *et al.*, J. Phys. Chem. B **60**, 1101 (1999).

[29] B. Gaulin *et al.*, Phys. Rev. Lett. **84**, 3446 (2000).

[30] T. Barnes, J. Riera, and D. A. Tennant, Phys. Rev. B **59**, 11384 (1999).

[31] A.Bernert *et al.*, Phys. Rev. B **66**, 165108 (2002).

[32] H. Nakao *et al.*, Phys. Rev. Lett. **85**, 4349 (2000).

[33] S. van Smaalen *et al.*, Phys. Rev. B **65**, 060101 (2002).

[34] H. Seo and H. Fukuyama, J. Phys. Soc. Jpn. **67**, 2602 (1998).

[35] P. Thalmeier and H. Fulde, Europhys. Lett. **44**, 242 (1998).

[36] M. V. Mostovoy and D. I. Khomskii, Solid State Commun. **113**, 159 (2000).

[37] M. Votja, A. Hübsch, and R. M. Noack, Phys. Rev. B **63**, 045105 (2001).

[38] M. Aichhorn *et al.*, Phys. Rev. B **65**, 201101R (2002).

[39] M. Aichhorn, M. Hohenadler, E. Ya. Sherman, J. Spitaler, C. Ambrosch-Draxl, and H. G. Evertz (2004), cond-mat/0312523.

[40] M. Cuoco, P. Horsch, and F. Mack, Phys. Rev. B **60**, R8438 (1999).

[41] D. Sa and C. Gros, Eur. Phys. J.B **18**, 421 (2000).

[42] M. N. Popova *et al.*, Phys. Rev. B **65**, 144303 (2002).

[43] M. Fischer *et al.*, Phys. Rev. B **60**, 7284 (1999).

[44] E. Y. Sherman *et al.*, Europhys. Lett. **48**, 648 (1999).

[45] G. H. Golub and C. van Loan, *Matrix Computations* (1989), The Johns Hopkins University Press.

[46] M. Daghofer, Master's thesis, TU Graz (2001).

[47] E. R. Davidson, Computers in Physics **7**, 5, 519 (1993).

[48] A. Hylleraas and B. Undheim, Z. Phys. **65**, 759 (1930).

[49] E. R. Davidson, J. Comput. Phys. **17**, 87 (1975).

[50] B. Liu, Numerical Algorithms in Chemistry (1978).

[51] S. R. White, Phys. Rev. Lett. **69**, 2963 (1992).

[52] K. G. Wilson, Rev. Mod. Phys. **47**, 773 (1973).

[53] W. von der Linden, *Computersimulationen*, lecture notes, TU Graz, 2003.

[54] S. Kirkpatrick, C. D. Gellat Jr., and M. P. Vecchi, Science **220**, 671 (1983).

[55] E. Marinari and G. Parisi, Europhys. Lett. **19**, 451 (1992).

[56] E. Marinari, *Optimized Monte Carlo Methods*, cond-mat/9612010, lecture notes, Budapest Summer School, 1996.